2008

# Low Noise, High Repetition Rate Semiconductor-based Mode-locked Lasers For Signal Processing And Coherent Communications

Franklyn Quinlan
*University of Central Florida*

# LOW NOISE, HIGH REPETITION RATE SEMICONDUCTOR-BASED MODE-LOCKED LASERS FOR SIGNAL PROCESSING AND COHERENT COMMUNICATIONS

by

FRANKLYN JOHN QUINLAN
B.A. The Colorado College, 1999
M.S. University of Central Florida, 2005

A dissertation submitted in partial fulfillment of the requirements
for the degree of Doctor of Philosophy
in CREOL, The College of Optics and Photonics
at the University of Central Florida
Orlando, Florida

Summer Term
2008

Major Professor: Peter J. Delfyett, Jr.

# ABSTRACT

This dissertation details work on high repetition rate semiconductor mode-locked lasers. The qualities of stable pulse trains and stable optical frequency content are the focus of the work performed. First, applications of such lasers are reviewed with particular attention to applications only realizable with laser performance such as presented in this dissertation. Sources of timing jitter are also reviewed, as are techniques by which the timing jitter of a 10 GHz optical pulse train may be measured. Experimental results begin with an exploration of the consequences on the timing and amplitude jitter of the phase noise of an RF source used for mode-locking. These results lead to an ultralow timing jitter source, with 30 fs of timing jitter (1 Hz to 5 GHz, extrapolated). The focus of the work then shifts to generating a stabilized optical frequency comb. The first technique to generating the frequency comb is through optical injection. It is shown that not only can injection locking stabilize a mode-locked laser to the injection seed, but linewidth narrowing, timing jitter reduction and suppression of superfluous optical supermodes of a harmonically mode-locked laser also result. A scheme by which optical injection locking can be maintained long term is also proposed. Results on using an intracavity etalon for supermode suppression and optical frequency stabilization then follow. An etalon-based actively mode-locked laser is shown to have a timing jitter of only 20 fs (1Hz-5 GHz, extrapolated), optical linewidths below 10 kHz and optical frequency instabilities less than 400 kHz. By adding dispersion compensating fiber, the optical spectrum was broadened to 2 THz and 800 fs duration pulses were obtained.

By using the etalon-based actively mode-locked laser as a basis, a completely self-contained frequency stabilized coupled optoelectronic oscillator was built and characterized. By simultaneously stabilizing the optical frequencies and the pulse repetition rate to the etalon, a 10 GHz comb source centered at 1550 nm was realized. This system maintains the high quality performance of the actively mode-locked laser while significantly reducing the size weight and power consumption of the system. This system also has the potential for outperforming the actively mode-locked laser by increasing the finesse and stability of the intracavity etalon.

The final chapter of this dissertation outlines the future work on the etalon-based coupled optoelectronic oscillator, including the incorporation of a higher finesse, more stable etalon and active phase noise suppression of the RF signal. Two appendices give details on phase noise measurements that incorporate carrier suppression and the noise model for the coupled optoelectronic oscillator.

For Katie

# ACKNOWLEDGMENTS

I would like to thank the entire Ultrafast Photonics group, members past and present, for their efforts that helped make this work possible. They are Prof. Peter Delfyett, Prof. Sangyun Gee, Dr. Michael Mielke, Dr. Tolga Yilmaz, Dr. Myoung Taek Choi, Dr. Kyungbum Kim, Dr. Wangkuen Lee, Dr. Luis Archundia, Dr. Bojan Resan, Dr. Nishant Bhatambrekar, Dr. Shinwook Lee, Sarper Ozharar, Ji-Myoung Kim, Dimitrios Mandridis, Ibrahim Ozdur, Mohammad Umar Piracha, Charles Williams, Iffat Nayyar, Sharad Bhooplapur, Abhijeet Ardey, Henock Legesse, Dat Nguyen, Nazanin Hoghooghi, Josue Davila-Rodriguez, and Sen-Yong Chen. I would particularly like to emphasize the importance of Prof. Peter Delfyett, Prof. Sangyoun Gee and Sarper Ozharar without whom none of what follows would have been possible.

# TABLE OF CONTENTS

# LIST OF FIGURES

# LIST OF TABLES

# CHAPTER 1
# INTRODUCTION

## *1.1 Signal processing and coherent communications in time and frequency domains*

Stable optical pulse trains with high repetition rates have a number of applications in optical communications and signal processing. Examples of how a stable pulse train may be exploited include optical time division multiplexed (OTDM) systems [1], digital-to-analog (DAC) [2] and analog-to-digital converters (ADC) [3] [4], and the generation of high speed arbitrary electrical waveforms [5]. An architecture using high repetition rate optical pulses for the generation of high speed electrical waveforms developed in [5] is shown in Figure 1.1. Here, each optical pulse is split, directed to separate modulators for phase modulation, recombined, and then photodetected. The pulses interfere as they are recombined, and power of the pulse at the photodetector will depend on the voltages sent to the set of modulators. By clocking the phase modulators at the pulse repetition rate, the power at the photodetector can be controlled on a pulse-by-pulse basis. Photodetection creates a series of electrical pulses of varying amplitude that when filtered electrically, comprise a high speed (up to half the pulse train repetition rate) RF waveform. For an arbitrary set of voltages on the modulators, a high speed arbitrary RF waveform is generated, useful for secure communication and radar applications [5].

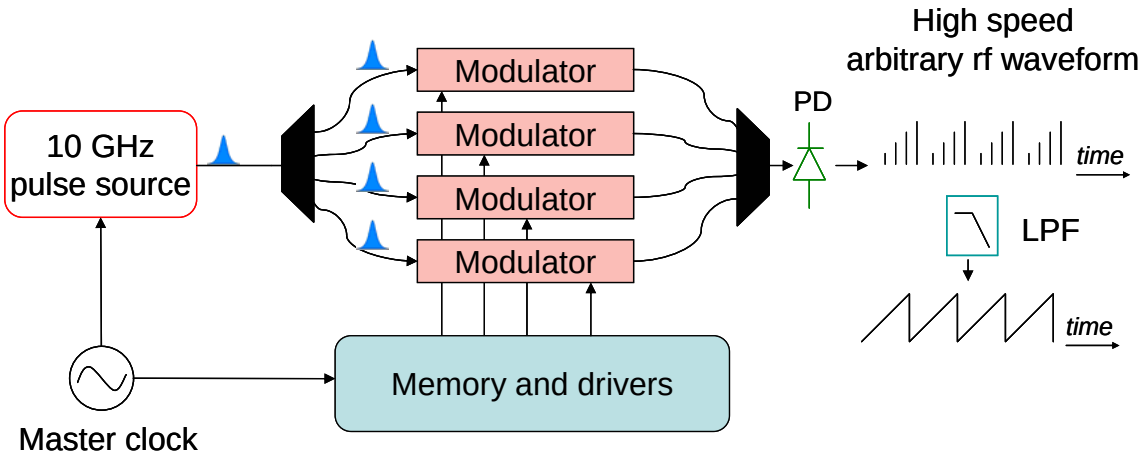


Figure 1.1: An example of a time domain application of a low timing jitter high repetition rate pulse source for the creation of high speed electrical waveforms. PD photodetector; LPF, lowpass filter.

Systems such as the RF arbitrary waveform generator have stringent requirements on the characteristics of the source pulse train in order to create high fidelity RF waveforms. As another example, a 10 gigasample/sec ADC requires a pulse train with an rms timing jitter under 30 fs and amplitude fluctuations under 0.049% to achieve 10 bits of resolution [6]. The ability of mode-locked lasers to produce high repetition rate stable pulse trains make them an obvious choice for high performance signal processing systems. Moreover, the particular advantages of semiconductor-based mode-locked lasers such as the high wall plug efficiency and compactness of these lasers make them worthy of investigation as pulse sources for state-of-the-art communication and signal processing applications. Creating stable pulse trains from semiconductor-based mode-locked lasers is a major focus of this work.

The fact that a mode-locked laser also produces a phase locked, regularly spaced frequency comb suggests a number of frequency domain applications for these lasers. For example, recent work has also shown the applicability of a stabilized multi-gigahertz-spaced comb to astronomical measurements [7]. With a multi-gigahertz spaced comb, the frequency spacing is sufficient for calibration of astrophysical spectrographs. This has lead to the prediction that a stabilized, multi-gigahertz frequency comb can enable radial velocity measurements with <1 cm/s precision, about two orders of magnitude more precise than current calibration techniques. A mode-locked laser's ability to produce a phase locked frequency comb also suggests that these lasers are also uniquely suited for frequency domain signal processing applications such as wavelength division multiplexing (WDM), optical code division multiple access (OCDMA), and optical arbitrary waveform generation (OAWG) [1]. An example of an OAWG architecture following [1] is shown in Figure 1.2. In Figure 1.2 a WDM filter separates the individual optical frequency components of the mode-locked laser. (Filtering technologies such as ring resonators have the ability to demultiplex optical frequency components at multi-gigahertz separation [8].) The phase and/or amplitude of the frequency components are independently modulated and then recombined to produce an arbitrary waveform. Since the frequency components of the laser must remain at the transmission peaks of the WDM filter, this system clearly demonstrates a constraint on the frequency comb for frequency domain applications, namely a high level of frequency stability. A stabilization technique requiring supercontinuum generation from the mode-locked laser pulse train can achieve an extraordinary level of stability of a frequency comb [9]. However, this stabilization technique has not yet been achieved with multi-gigahertz repetition rate

mode-locked lasers. This is because the generation of the supercontinuum requires very short pulses (usually ~ 100 fs or shorter) with high energy to produce the necessary high peak powers, a difficult task to generate from high repetition rate pulse trains, since available energy is shared with a larger number of pulses. A high repetition rate, compact, wall plug efficient mode-locked laser that is frequency stabilized would be a great boon to the realization of viable optical arbitrary waveform generation. The development of a semiconductor-based mode-locked laser with a high level of optical frequency stability is another major focus of this work.

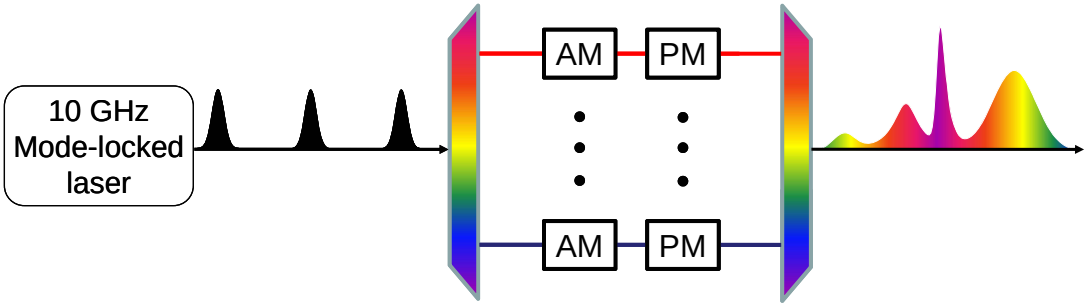


Figure 1.2: An example of a frequency domain application of frequency stabilized mode-locked lasers for optical arbitrary waveform generation. AM, amplitude modulator; PM, phase modulator

Additionally, narrow linewidth mode-locked lasers have the potential for coherent communication applications such as phase shift keying and quadrature amplitude modulation [10]. A collection of different modulation schemes and the laser linewidths they require is shown in Table 1 [10]. Whereas DFB lasers typically have linewidths ~1 MHz and above, mode-locked lasers can produce linewidths suitably narrow for the modulation schemes of Table 1 [11]. Again, coherent communications, just like signal

processing in time and frequency domains, leads to the conclusion that semiconductor-based mode-locked lasers are uniquely suited for high performance coherent communication and signal processing applications.

Table 1 Linewidth requirements for different modulation techniques, after [10]. $\Delta\nu$ is the linewidth, $R_b$ is the bit rate.

| **Modulation Format** | **Detection** | **$\Delta\nu/R_b$** | **$\Delta\nu$ for $R_b$ = 10 Gb/s** |
|---|---|---|---|
| 2-DPSK | Differentially Coherent | $3.0\cdot10^{-3}$ | 30 MHz |
| 4-DPSK | Differentially Coherent | $5.0\cdot10^{-4}$ | 5 MHz |
| 2-PSK | Coherent | $8.0\cdot10^{-4}$ | 8 MHz |
| 4-PSK | Coherent | $2.5\cdot10^{-5}$ | 250 kHz |
| 8-PSK | Coherent | $1.5\cdot10^{-6}$ | 15 kHz |
| 16-PSK | Coherent | $2.4\cdot10^{-7}$ | 2.4 kHz |
| 8-QAM | Coherent | $9.0\cdot10^{-6}$ | 90 kHz |
| 16-QAM | Coherent | $6.9\cdot10^{-7}$ | 6.9 kHz |

### *1.2 Laser linewidth and harmonic mode-locking*

The compactness of semiconductor lasers allows for fundamental mode-locking at multi-gigahertz repetition rates [12] [13], since the short cavity lengths attainable lead to cavity round trip times and optical longitudinal mode spacings in the multi-gigahertz range. However, such lasers do not have the necessary properties for the applications

discussed above. First, these lasers tend to have broad optical linewidths. For example, a semiconductor laser fundamentally mode-locked at 10 GHz has been measured to have an optical linewidth of 55 MHz [12]. This linewidth is far too broad for coherent communication applications of Table 1 such as quaternary phase-shift keying (4-PSK) and octonary quadrature-amplitude modulation (8-QAM). Moreover, the fact that the spontaneous emission contribution to the pulse train timing jitter is proportional to the square root of the linewidth [14] makes a narrow linewidth desirable for time domain applications of the mode-locked laser. The linewidth of a comb element of a mode-locked laser may be expressed as [15] [16]

$$\Delta\nu = \frac{v_g^2 \mu h \nu \ln\left(1/R^2\right)}{8\pi P L^2}\left(1+\alpha^2\right). \tag{1.1}$$

Definitions of the symbols are as follows: $\Delta v$, optical linewidth; $vg$, group velocity; $\mu$, inversion factor; $h$, Planck's constant; $v$, lasing optical frequency; $R$, laser facet reflectivity; $P$, optical power; $L$, cavity length; $\alpha$, linewidth enhancement factor. With a given semiconductor gain medium, the factors in this expression that can be most easily manipulated are the average optical power, the cavity length, and the cavity loss per roundtrip. Therefore, in order to achieve narrow linewidths for each frequency element of a mode-locked laser, the optical power may be increased by increasing the driving current of the semiconductor gain, the cavity loss may be kept to an absolute minimum and, for large reductions in the linewidth, the cavity length may be dramatically increased. Lasers with long cavity lengths are used in these investigations as a means to greatly reduce the optical frequency linewidth and the lower pulse-to-pulse timing jitter of the mode-locked

laser pulse train. The extended cavity laser has another advantage, namely an extended cavity allows intracavity elements that can used to stabilize the frequency comb.

In order to maintain a high repetition rate pulse train in a long cavity length laser, harmonic mode-locking must be employed [12]. In active harmonic mode-locking, the modulation rate is not equal to the cavity free spectral range as it is in fundamental mode-locking, but rather at an integer multiple $N$ of the free spectral range. Harmonic mode-locking and its implications can be interpreted in both the time and frequency domains. Beginning in the time domain, when a laser is mode-locked at the $N$th harmonic, there are $N$ pulses inside the laser cavity. These pulses, being separated by less than the cavity round trip time, are not derived from the regeneration of a single pulse. Pulses separated by the cavity round trip time can however be considered as the regeneration of a pulse, and the pulse train can be divided into $N$ distinct interleaved pulse trains. In the frequency domain, the interleaved pulse train picture leads to overlapped spectra, each spectral set consisting of modes separated by the inverse of the cavity round trip time. These spectra interfere (with different phases for different spectral sets) to produce a pulse train at $N$ times the cavity fundamental.

Interpretation of harmonic mode-locking may also begin in the frequency domain. The action of the mode-locker correlates the phase among modes separated by the mode-locking rate. Since the laser cavity modes are separated by the inverse of the round trip time, the frequency spectrum may be considered as interleaved sets of phase locked modes. This leads to a time domain picture of overlapping pulses with a repetition rate of $N$ times the fundamental. The different views of harmonic mode-locking are shown in Figure 1.3.

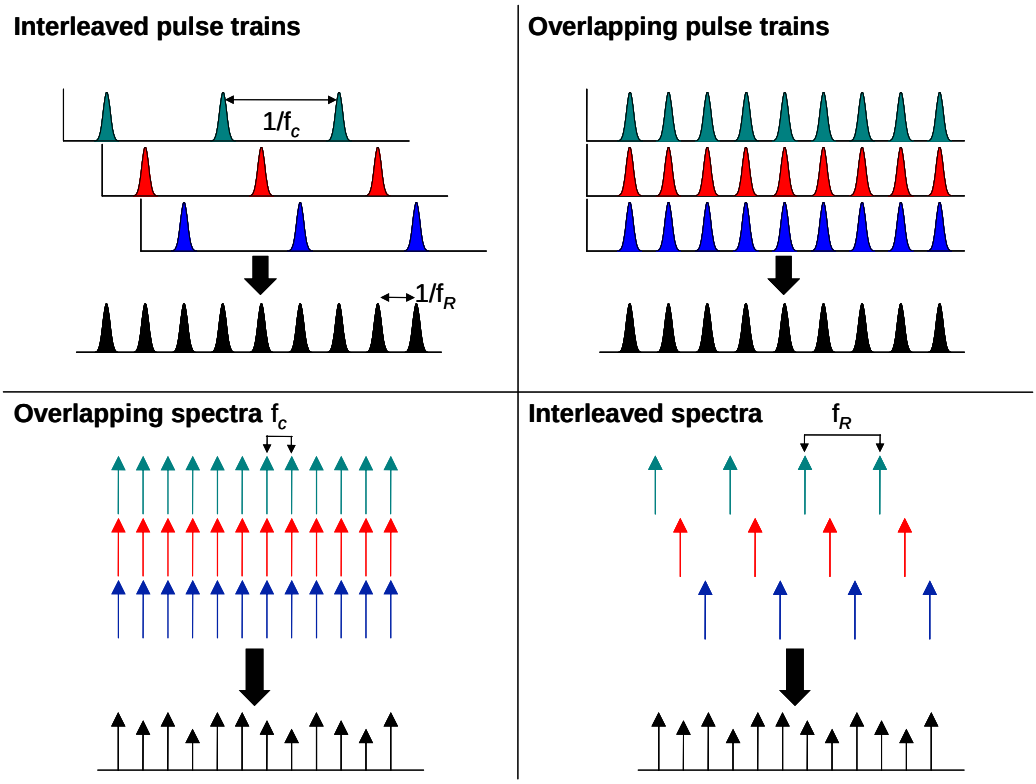


Figure 1.3: Four pictures of harmonic mode-locking. Harmonic mode-locking may be understood in terms of interleaved pulse trains and overlapping spectra, or as interleaved spectra and overlapping pulse trains.

The frequency domain picture of interleaved phase locked, or supermode, sets is useful for understanding the unique challenges of harmonic mode-locking. The simultaneous lasing of independent optical supermodes causes random fluctuations in the pulse train amplitude and timing as the relative phase and amplitude among supermodes fluctuates. This noise is the so called supermode noise in the timing jitter and pulse-to-pulse amplitude noise [12]. The supermode noise can all but nullify any noise reduction obtained by increasing the cavity length. Moreover, the simultaneous lasing of different optical supermodes precludes the use of a single phase locked frequency comb with

multi-gigahertz spacing. This makes the laser unsuitable for frequency domain applications such as OCDMA and WDM. Clearly, limiting the impact of the supermodes is important in both time and frequency domain applications.

In the chapters that follow, work on semiconductor-based, low noise and optical frequency stabilized harmonically mode-locked lasers is described in detail. Chapter 2 discusses the sources of timing jitter in actively mode-locked lasers and various means by which the timing jitter may be measured. In Chapter 3, experiments that explore the effect of the RF source used to mode-lock the laser are described. It is shown how the RF source phase noise limits both absolute and relative jitter and how a mode-locked laser can filter the RF source noise. These experiments lead to the realization of an ultralow timing and amplitude jitter source suitable for time domain applications. The focus then shifts to generating optical frequency stabilized lasers in Chapter 4 where injection locking for supermode noise suppression and optical frequency stabilization is discussed. Chapter 5 describes another method for frequency stabilization, namely using an intracavity etalon and the Pound-Drever-Hall laser frequency stabilization technique. The laser developed in Chapter 5 is used as the basis of the experiments of Chapter 6 where regenerative mode-locking is implemented. The regeneratively mode-locked laser of Chapter 6 simultaneously addresses supermode noise, optical linewidth, optical frequency stability and RF source noise to create a completely self contained low noise, frequency stabilized source. Chapter 7 discusses future work that will improve the performance of the regeneratively mode-locked laser of Chapter 6. The described improvements are active suppression of the pulse repetition rate timing jitter and the inclusion of a higher finesse etalon into the laser cavity. Appendix A discusses

interferometric noise measurements and Appendix B explains in detail the noise model of the regeneratively mode-locked laser.

# CHAPTER 2
# SOURCES OF TIMING JITTER AND NOISE MEASUREMENT

## *2.1 Introduction*

While the configuration of mode-locked lasers can vary widely, there are a number of core components and processes common to most of these lasers. Figure 2.1 is a generalized block diagram of a mode-locked laser. Necessary components for a mode-locked laser are gain, output coupling, and either an active mode-locker such as an electrically controlled loss modulator, a saturable absorber, or both. All laser cavities will also have some dispersion and some laser cavities may include polarization control and optical filters.

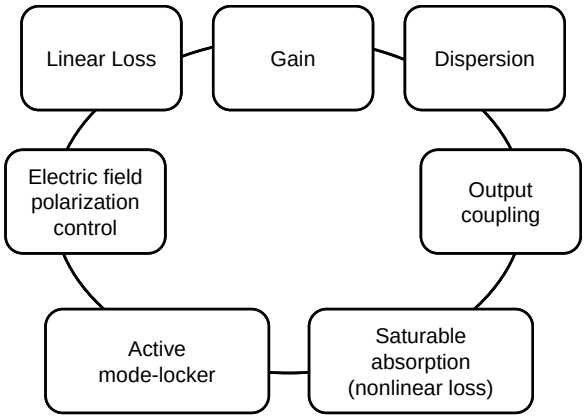


Figure 2.1: Block diagram schematic of a mode-locked laser

If the value of any of these parameters changes with time, for example, changes to the cavity birefringence or fluctuations in the gain, the pulse train will be disturbed, resulting in amplitude and timing jitter of the pulse train. (The shape of the pulse can also change, but this is a higher order effect that is not considered here. Also not considered is noise in the carrier-envelope offset phase [17].) Aside from changing laser parameters, more

fundamental sources of noise must also be considered. The most fundamental source of noise on the pulse train is quantum mechanical in nature, namely spontaneous emission and vacuum fluctuations. It is the mathematical representation and measurement of the noise on the pulse train, expressed in terms of timing jitter and amplitude fluctuations, that is the focus of this chapter.

### *2.1 Sources of timing jitter in actively harmonically mode-locked lasers*

A mode-locked laser pulse train has instabilities in the time separation between pulses. This timing jitter is a result of many factors, both technical and fundamental. Technical noise sources include temperature and vibration induced jitter, and can be addressed by ensuring good environmental isolation. Two more fundamental contributors to an actively mode-locked laser's timing jitter are spontaneous emission and mode-locker phase noise. As shown in [14], the power spectral density of the timing jitter due to spontaneous emission and mode-locker phase noise may be written as

$$S^J(\omega) = \frac{1}{\omega_0^2}\frac{\Gamma^2}{\omega^2+\Gamma^2}S_{rf}^{\phi}(\omega) + \frac{4\sqrt{2}}{\omega_0^2}\frac{\Delta\omega_{ST}}{N\Gamma}\frac{\Gamma}{\omega^2+\Gamma^2}\left[1+\frac{(N\Delta\omega)^2}{\omega^2+(2\Gamma)^2}\right]. \tag{2.1}$$

The definitions of the symbols in Equation 2.1 are listed in Table 2. The root mean square (RMS) timing jitter is obtained by integrating the jitter spectrum [18][18]:

$$\sigma_J = \int S^J(\omega)\frac{d\omega}{2\pi}. \tag{2.2}$$

Table 2: Definition of symbols for Equation 2.1

| | |
|---|---|
| $S^J(\omega)$ | Power spectral density of the timing jitter |
| $\omega_0$ | Pulse repetition angular frequency |
| $\Delta\omega$ | Mode-locker frequency detuning from laser free spectral range |
| $\Gamma$ | Mode-locked laser characteristic filter angular frequency |
| $S_{rf}^{\phi}(\omega)$ | Power spectral density of the mode-locker phase noise |
| $\Delta\omega_{ST}$ | Schawlow-Townes linewidth |
| $N$ | Integer proportional to the number of modes in the mode-locked spectrum |

A few conclusions can be drawn by inspecting Equation 2.1. In the first term, note the presence of the mode-locker phase noise, $S_{rf}^{\phi}(\omega)$. The mode-locker phase noise tends to dominate the noise spectrum for low offset frequencies. Also note $S_{rf}^{\phi}(\omega)$ is filtered when imposed onto the timing jitter. The characteristic frequency $\Gamma$ of the filtering depends on the quality factor of the laser cavity. The ability of a mode-locked laser to filter the phase noise of a RF signal has many consequences important to this work and is explored extensively in the following chapters. The second term of Equation 2.1 is the spontaneous emission contribution to the timing jitter. To reduce the contribution of the spontaneous emission, clearly the detuning must be kept to a minimum. This can be done by careful control of the mode-locker frequency, although it should be noted that the laser is more sensitive to detuning the broader the optical bandwidth. (Also, when optical stability is not required, in a laser cavity with dispersion, the optical spectrum can shift to a position that has the minimum detuning in a self-stabilizing way [19].) Equation 2.1 also points to

the importance of the Schawlow-Townes linewidth [20] in determining the timing jitter, namely the narrower the Schawlow-Townes linewidth is, the lower the timing jitter will be. As described in Chapter 1, the linewidth may be reduced by keeping the optical power high, the loss low and the cavity length long. In order to maintain a high repetition rate with a long cavity, harmonic mode-locking must be employed. Equation 2.1, developed for fundamental mode-locking, can be adapted for harmonic mode-locking (under certain assumptions mentioned below) as follows:

$$S^{J}(\omega)=\frac{1}{\omega_0^2}\sum_{m=-\infty}^{\infty}\frac{\Gamma^2}{(\omega-m\omega_f)^2+\Gamma^2}S_{rf}^{\phi}(\omega)+\sum_{m=-\infty}^{\infty}\frac{4\sqrt{2}}{\omega_0^2}\frac{\Delta\omega_{ST}}{M\Gamma}\frac{\Gamma}{(\omega-m\omega_f)^2+\Gamma^2}\left[1+\frac{(N\Delta\omega)^2}{(\omega-m\omega_f)^2+(2\Gamma)^2}\right] \tag{2.3}$$

where $\omega_f$ is the cavity fundamental frequency, or the inverse of the cavity round trip time. This noise spectrum consists of repeated noise peaks separated by the cavity fundamental frequency. The repeated noise peaks are referred to as the "supermode noise spurs" in the literature [12], [21], [22]. A plot of Equation 2.3 is shown in Figure 2.2. The noise added due to the supermode noise spurs can completely negate noise reduction due to a longer laser cavity. Benefits of a long laser cavity can be regained if the noise spurs can be suppressed or mitigated. (The assumption that all the supermode noise spurs have the same spectrum holds only when the pulse-to-pulse noise is uncorrelated [22]. Nested cavities [23] or the inclusion of an intracavity etalon [12] can correlate the pulse-to-pulse noise and the supermode noise spurs will no longer be equally distributed in power.) Addressing the supermode noise spurs is another major focus of this work.

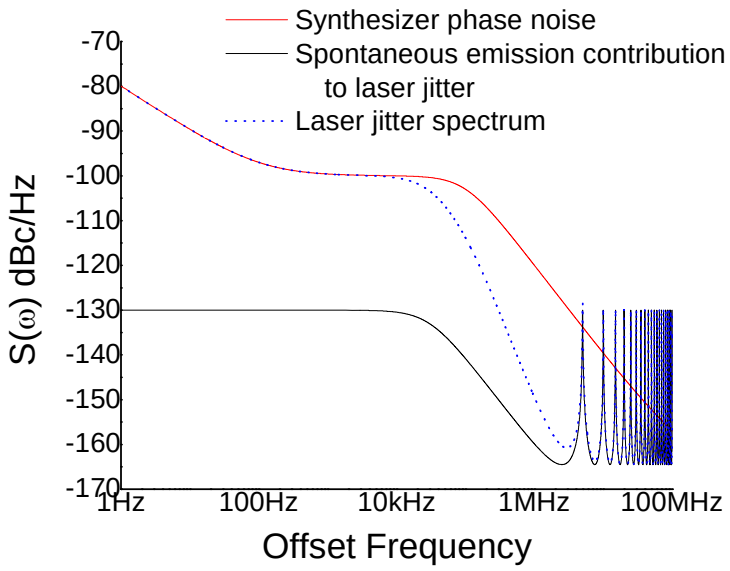


Figure 2.2: Phase noise of an RF synthesizer, a harmonically mode-locked laser's jitter spectrum and spontaneous emission contribution to the jitter. At low offset frequencies the jitter is dominated by the synthesizer noise. At high offset frequencies the supermode noise spurs dominate. Also note the filtering of the synthesizer noise by the mode-locked laser.

### *2.2 Measuring timing and amplitude jitter*

Measuring both the pulse-to-pulse timing jitter and the pulse-to-pulse energy fluctuations can be performed on the photodetected pulse intensity spectrum by examining the phase and amplitude noise sidebands of the photodetected carrier at the pulse repetition rate frequency [18]. (Timing jitter can also be measured by purely optical means [24].) The timing jitter can be determined from the phase noise sidebands by

$$\sigma_J = \frac{1}{2\pi f_{ML}} \sqrt{2\int L(f)df} \tag{2.4}$$

where $\sigma_J$ is the root-mean-squared jitter, $f_{ML}$ is the pulse repetition rate, and $L(f)$ is the power of the phase noise sideband in a one Hertz bandwidth relative to the carrier power. $S^{\phi}(\omega)$ of Equation 2.1 is related to $L(f)$ by $S^{\phi}(\omega) = 2L(2\pi f)$. To obtain the total RMS jitter, the upper limit of integration in Equation 2.4 should be the Nyquist frequency (one-half the pulse repetition rate). For multigigahertz pulse rates, measuring the phase noise sidebands to the Nyquist frequency is difficult, and reports of phase noise measured out to Nyquist are rare [12], [25]. Instead, assumptions about the noise spectrum and extrapolations are made [4], [26]. Similar to the timing jitter, the pulse energy fluctuations are related to the amplitude noise sidebands via

$$\frac{\Delta E}{E} = \sqrt{2\int M(f)df} \tag{2.5}$$

where $\Delta E/E$ is the fractional fluctuation of the pulse energy and $M(f)$ is the power in an amplitude noise sideband in a one Hertz bandwidth relative to the carrier power. Again, the noise should be measured to the Nyquist frequency. Measuring the amplitude noise can be performed with an AM detector consisting of a splitter, phase shifter and double balanced mixer [27], or a diode detector [28].

Measuring the amplitude noise of an RF source is relatively straightforward, but measuring the phase noise of a low noise RF signal requires some care. Since only phase differences are meaningful, a separate source against which the phase fluctuations are measured must be decided upon. Any reference source will have its own phase instabilities which in general may be partially correlated with the phase instabilities of the

device under test. In order to best illustrate some of the advantages and limitations of different reference sources, some basic definitions and noise measurement setups are reviewed [29], [30]. Also, the power of phase noise sidebands to be characterized can lie more than 16 orders of magnitude below the power of the RF carrier. Needless to say any measurement system must show large dynamic range and high sensitivity. A noise measurement system with a low noise floor is critical, and analysis and reduction of the noise floor is also considered.

### 2.2.1 Absolute noise

The photodetected signal from a mode-locked laser can be represented (after the filtering of harmonics) as a sinusoidal voltage signal with amplitude and phase noise,

$$S(t) = [1 + \alpha_S(t)]V_0 \cos[\omega_0 t + \phi_S(t)] \tag{2.6}$$

where $\alpha_S(t)$ is the amplitude noise, $V_0$ is the nominal amplitude of the signal, $\omega_0$ is the nominal frequency and $\phi_S(t)$ is the random varying phase. (Recall that it is the power in the phase noise of the photodetected signal that contains the pulse-to-pulse timing jitter information, and the amplitude noise contains the pulse-to-pulse energy jitter information.) For all cases of interest, $\alpha_S(t)$ and $\phi_S(t)$ are <<1, and the photodetected signal $S(t)$ may be expanded as

$$S(t) = V_0[\cos(\omega_0 t) + \alpha_S(t)\cos(\omega_0 t) - \phi_S(t)\sin(\omega_0 t)]. \tag{2.7}$$

This signal can be mixed with a reference that also has small amplitude and phase noise

$$R(t) = V_0[\cos(\omega_0 t + \delta) + \alpha_R(t)\cos(\omega_0 t + \delta) - \phi_R \sin(\omega_0 t + \delta)] \tag{2.8}$$

where $\delta$ accounts for a relative phase shift between $S(t)$ and $R(t)$. The product of $S(t)$ and

$R(t)$ can be performed with a double balanced mixer, and the resulting baseband signals can be isolated with a low pass filter following the mixer. When $\delta = 90°$, the resulting baseband signal is proportional to the phase difference of $S(t)$ and $R(t)$:

$$V_M = \kappa[\phi_S(t) - \phi_R(t)] \tag{2.9}$$

where $\kappa$ is related to the conversion efficiency of the mixer. Phase fluctuations $\phi_S(t)$ and $\phi_R(t)$ relative to the ideal $V_0 \cos(\omega_0 t)$ are termed the absolute phase noise of their respective signals. The power spectra of the absolute phase fluctuations $\phi_S(t)$ and $\phi_R(t)$ are defined as $S_S^{\phi}(\omega)$ and $S_R^{\phi}(\omega)$, respectively.

If the noise in the signal and reference are completely uncorrelated, the power spectrum of the phase difference is simply the addition of the individual power spectra:

$$S_{S,R}^{\phi}(\omega) = S_S^{\phi}(\omega) + S_R^{\phi}(\omega). \tag{2.10}$$

If $S_S^{\phi}(\omega)$ is known to be much greater than $S_R^{\phi}(\omega)$, the resulting power spectrum is approximately $S_S^{\phi}(\omega)$. A schematic for measuring the absolute noise of source is shown in Figure 2.3.

A better way to measure the noise of near equivalent sources is the three source method. The three source method involves measurements of all three combinations of sources. For three uncorrelated sources with power spectra $S^{\phi}(\omega), S^{\gamma}(\omega)$, and $S^{\sigma}(\omega)$, the phase noise $S^{\phi}(\omega)$ is determined by

$$S^{\phi}(\omega) = \frac{S^{\phi,\gamma}(\omega) + S^{\phi,\sigma}(\omega) - S^{\sigma,\gamma}(\omega)}{2}. \tag{2.11}$$

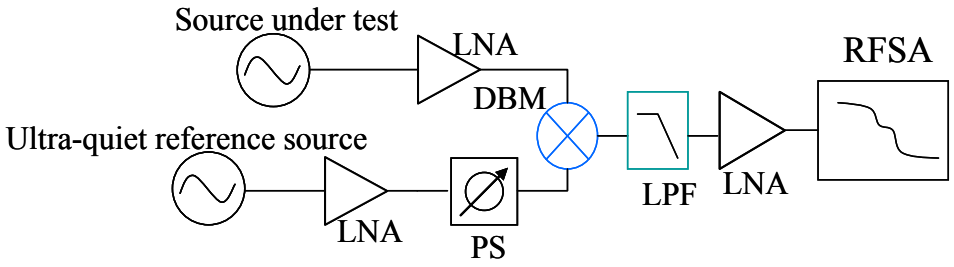


Figure 2.3: Setup for measuring the absolute phase noise of a source. The same setup is used for the three source method. PS, phase shifter; DBM, double balanced mixer; LPF, low pass filter; LNA, low noise amplifier, RFSA, radio frequency spectrum analyzer.

### 2.2.2 Relative Noise

A phase noise measurement designed to measure the phase noise of two port devices is shown in Figure 2.4. In this case, the phase noise of the two signal inputs of the mixer are derived from the same source and cannot be considered uncorrelated. A simple way to account for phase noise transfer through the two port device is to treat it as a linear system when acting on the phase noise (see Appendix B for details). The phase noise of the signal from the two port device thus may then be written as

$$\phi_S(t) = h(t) * \phi_R(t) + \phi_{DUT}(t) \tag{2.12}$$

where $h(t)$ is the response function of the two port device to the input phase noise and $\phi_{DUT}(t)$ is uncorrelated noise added by the two port device. The transfer function associated with $h(t)$ is $|H(\omega)|e^{i\theta}$. The power spectrum of the signal from the two port device is

$$S_{out}^{\phi}(\omega) = |H(\omega)|^2 S_R^{\phi}(\omega) + S_{DUT}^{\phi}(\omega). \tag{2.13}$$

The power spectrum of the phase noise difference $\phi_S(t) - \phi_R(t)$ at the output of the mixer is

$$S_{rel}(\omega) = S_R^{\phi}(\omega) \cdot \left[1 + |H(\omega)|^2 - 2|H(\omega)|\cos(\theta(\omega))\right] + S^{\phi}{}_{DUT}(\omega). \tag{2.14}$$

Herein after, the term relative noise is reserved for such a measurement. In cases where $|H(\omega)|e^{i\theta} \approx 1$ only the added noise of the two port device, also called the residual noise, is measured [31].

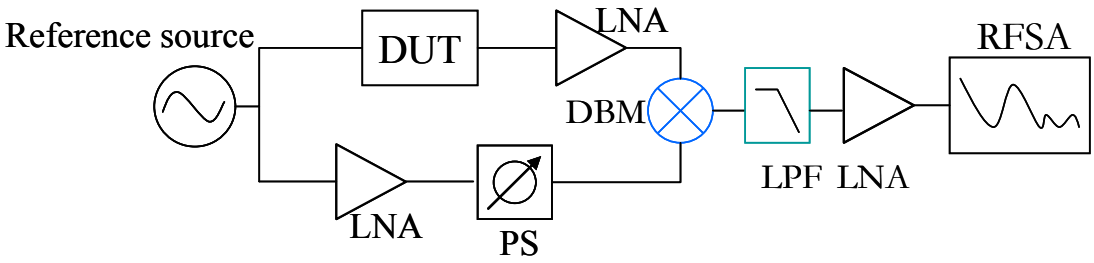


Figure 2.4: Two port device "residual" phase noise measurement setup. DUT, device under test; PS, phase shifter; DBM, double balanced mixer; LPF, low pass filter; LNA, low noise amplifier, RFSA, radio frequency spectrum analyzer.

### 2.2.3 Delay Line Frequency Discriminator

When a separate lower noise reference is not available, knowledge of the absolute noise $S^{\phi}$ can still be obtained via the frequency discriminator (FD) noise measurement method. This is a single source method, where the signal from the device under test is split and a relative delay is imposed before being applied to the mixer. A schematic is shown in Figure 2.5.

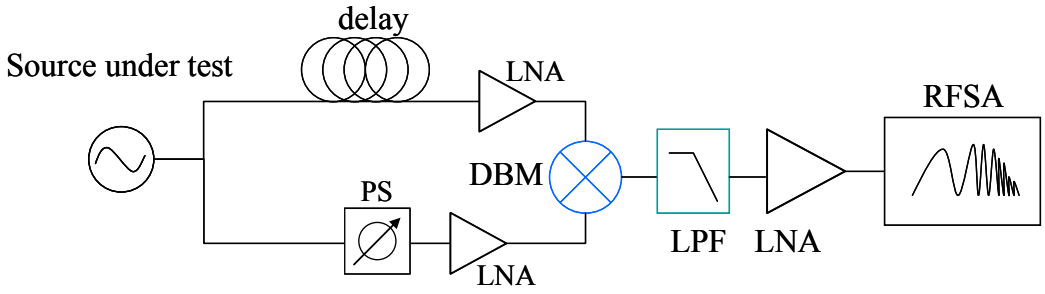


Figure 2.5: Measurement schematic for a delay line frequency discriminator. PS: phase shifter; DBM: double balanced mixer; LPF: low pass filter; LNA: low noise amplifier; RFSA: radio frequency spectrum analyzer.

The voltage signal after the mixer of Figure 2.5 can be shown to be

$$S_{FD}^{\phi}(\omega) = 2 \cdot S_{DUT}^{\phi}(\omega) \cdot (1 - \cos(\omega\tau)) \tag{2.15}$$

where $\tau$ is the relative delay between the two signals from the device under test. The modulation produced by the relative delay creates an offset frequency-dependent measurement sensitivity that deserves some attention and is shown through an analysis of the FD transfer function, shown in Figure 2.6. The transfer function goes to zero for frequencies that are integer multiples of $1/\tau$ and an FD cannot accurately relate noise values at frequencies near the interference nulls.. Also, since frequency values are usually measured on a logarithmic scale, at large frequency offsets the individual nulls are not resolved. For these reasons, the frequency discriminator is usually only used for frequency offsets less than $1/\tau$.

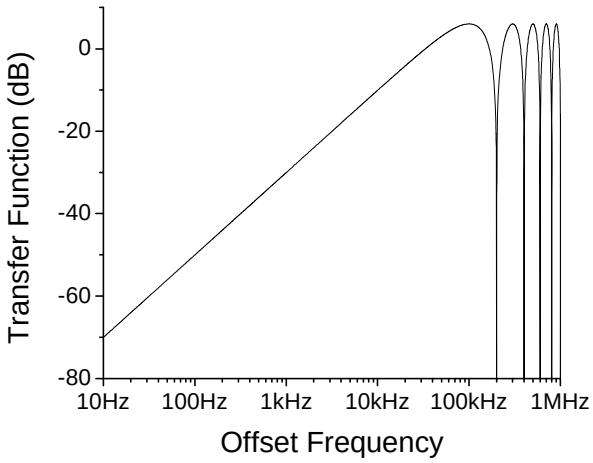


Figure 2.6: Plot of the delay line frequency discriminator transfer function of $2(1-\cos(\omega\tau))$. The relative delay used in 5 μs.

The relative delay $\tau$ not only affects the maximum frequency offset of the measurement, but the sensitivity at small offsets as well. To see why this is so, the detector noise must be considered. For a detector phase noise $S_D^{\phi}(\omega)$, the measurement sensitivity is given by

$$\frac{S_D^{\phi}(\omega)}{2(1-\cos(\omega\tau))} \tag{2.16}$$

(this can be seen by adding the detector noise to Equation 2.15 and solving for $S_{DUT}^{\phi}$). Equation 2.16 is plotted in Figure 2.7 for two different delays. Clearly the sensitivity at low offsets improves as $\tau$ is increased. Since the maximum frequency offset decreases with increased delay $\tau$, a compromise must be reached between desired sensitivity and maximum frequency offset of the measurement.

Measuring the noise floor of the FD consists of measuring $S_D^{\phi}$ by removing the relative delay $\tau$, then calculating Equation 2.16 with the measured $S_D^{\phi}$ and the appropriate $\tau$.

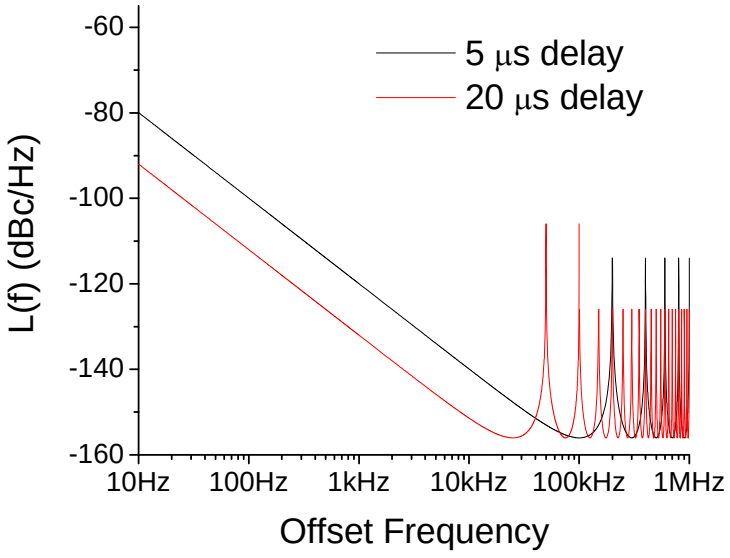


Figure 2.7: Delay line frequency discriminator noise floor for 5 μs and 20 μs delays. A value of -150 dBc/Hz for $S_D^{\phi}(\omega)$ is used.

### 2.2.4 Noise floor

In the analysis of the phase noise measurements considered thus far, with the exception of the brief mention for determining the sensitivity of the FD, noise originating in the phase noise detection system itself has been ignored. The most fundamental noise sources are shot noise associated with photodetection and thermal noise. For a CW laser signal illuminating a photodetector, the shot noise power is given as [20]

$$\sigma_{shot} = 2q\bar{i}RB \tag{2.17}$$

where $q$ is the charge of an electron, $R$ is the system impedance, $B$ is the measurement bandwidth and $\bar{i}$ is the average photocurrent. The average photocurrent is simply the product of the average optical power $P_{opt}$ and the detector responsivity $\Re$:

$$\bar{i} = \Re P_{opt}. \tag{2.18}$$

Strictly speaking, Equation 2.17 does not apply for time varying signals [32], however empirical results have shown its applicability to a mode-locked pulse train phase noise. The phase noise associated with shot noise (in a 1 Hz bandwidth) is therefore given by

$$L_{shot}(f) = \frac{q\bar{i}R}{P_{rf}} \tag{2.19}$$

where $P_{rf}$ is the power in the RF carrier. Since $\bar{i}$ is proportional to the optical power and $P_{rf}$ is proportional to the square of the optical power, $L_{shot}(f) \propto 1/P_{opt}$. This is contrasted with the thermal noise contribution to the phase noise, given as

$$L_{therm}(f) = \frac{kT}{2P_{rf}} \tag{2.20}$$

where $k$ is Boltzmann's constant, and $T$ is the system temperature. (The factor of two in the denominator accounts for the equal separation of the thermal noise into phase and amplitude noise.) The phase noise due to thermal noise goes as $L_{therm}(f) \propto 1/P_{opt}^2$. Because of the different dependence on the optical power of the thermal and shot noise, thermal noise will limit the noise floor for low optical powers while shot noise is the limiting fundamental noise for high optical powers. The crossover occurs at an optical power of

$$P_{opt} = \frac{kT}{2qR\Re}. \tag{2.21}$$

For typical parameter values of an operating temperature of 273 K, photodetector responsivity of 0.8 A/W and a 50 ohm system, the crossover optical power is -5.3 dBm.

Of course, shot and thermal noise are not the only noise sources of a measurement system. There will be flicker and AM to PM conversion in the photodetector and mixer, but the noise originating in the amplifiers used to detect the phase noise often set the noise floor. The amplifiers will exhibit flicker noise and white noise. (The white noise level is characterized by the noise figure). The noise from the amplifiers increases the optical power needed to be shot noise limited. At low offset frequencies, flicker noise dominates; at large offset frequencies, the white noise sets the noise floor of the system. A typical noise floor is shown in Figure 2.8. Flicker noise is characterized by a 1/f (10 dB per decade) roll-off, and originates in low frequency parametric variations that are nonlinearly upconverted to modulate the amplified RF carrier [33]. Amplifiers with a low noise figure are best when the white noise level is of concern; however such amplifiers are not necessarily optimized for low flicker, or vice versa. A pictorial representation of the noise measurement showing the transference of flicker noise from amplifiers prior to the mixer is shown in Figure 2.9. The two signals are represented as a sum of a carrier and noise sidebands. The flicker noise associated with amplifying an RF carrier is shown along with the input noise sidebands we wish to measure. Since all noise sidebands are weak compared to the carriers, sideband-sideband multiplications are insignificant compared to carrier-sideband multiplications (the carrier-carrier term is at DC). The mixer output is therefore the noise of the device under test plus the flicker of both amplifiers.

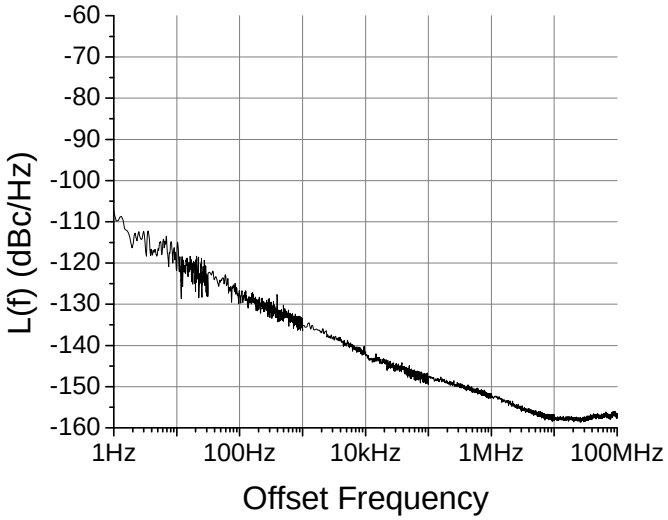


Figure 2.8: Typical phase noise measurement noise floor.

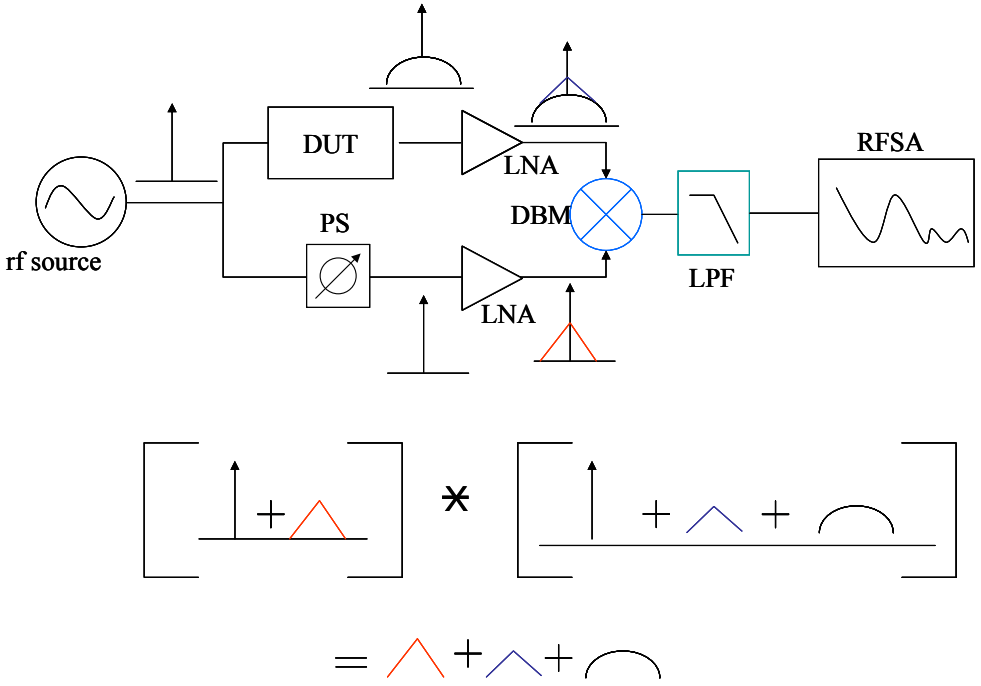


Figure 2.9: Pictorial representation of a phase noise measurement via saturated mixer as phase detector with amplifier flicker. "*" denotes convolution.

The noise floor may be measured by removing the DUT of Figure 2.9 (while maintaining a relative 90° phase shift), being careful to match the signal powers to those used in the actual noise measurement. Also, the relative delay between the signals into the mixer must be minimized to avoid frequency discriminator effects. Calibrating the instrument involves measuring the phase to voltage conversion efficiency $\kappa$ which may not be constant for all offset frequencies of interest. A noise measurement system that reduces the contribution of the amplifier flicker noise is explained in Appendix A.

### *2.3 Noise sources and measurement summary*

In summary, the major contributions to an actively mode-locked laser's timing jitter have been discussed. These include technical or environmental noise sources, and the more fundamental noise sources of RF source phase noise and amplified spontaneous emission. The phase noise of the RF source used as the mode-locker contributes heavily to the timing jitter, however, if the laser's quality factor is high enough, the RF source phase noise will be filtered as it is transferred onto the timing jitter. For a harmonically mode-locked laser, supermode noise spurs can contribute significantly to the timing jitter, and their effect needs to be mitigated to achieve a low timing jitter source. Also, measurement techniques to measure the absolute and relative phase noise of an RF source have been reviewed. The tradeoffs among different measurement methods have been outlined and the major contributions to the noise floor have been addressed.

# CHAPTER 3
# AN ULTRALOW TIMING JITTER MODE-LOCKED LASER

## *3.1 Introduction*

In Chapter 2, the concepts of absolute noise and relative noise as well as various schemes to measure them were discussed. In this chapter, absolute and relative phase noise measurement results are presented concentrating on the effects of the RF source [30]. First, an Agilent synthesizer was used as the RF source to mode-lock both an erbium-based mode-locked laser and a semiconductor-based mode-locked laser. Sections 3.2 and 3.3 describe the devices used and absolute and relative noise measurements performed. In Sections 3.4 and 3.5, further investigations were made by driving the lasers "in series" and "in parallel" that revealed more information on the absolute and residual phase noise of a mode-locked laser. Building upon these initial results, the semiconductor gain-based laser was rebuilt and the synthesizer was replaced with a lower noise oscillator forming an ultralow jitter source. Apart from providing low jitter, this laser gives the clearest measurement of the RF source phase noise transfer function. It also provides the opportunity to examine the effect of the laser optical power on the measured timing jitter. The description of and experiments on the ultralow timing jitter source are in Section 3.6. The results presented in this chapter are summarized in Section 3.7.

## *3.2 Synthesizer and mode-locked lasers*

The devices used for the original test of the filtering effect are an RF synthesizer and two high quality factor lasers, one semiconductor based and one erbium fiber based. The RF synthesizer is an Agilent 8254A, 250 kHz--40 GHz frequency synthesizer with the

low noise option [28], and is used to provide the timing signal for both the erbium and the semiconductor based lasers. A diagram of the semiconductor based laser is shown in Figure 3.1. A 100 meter fiber delay is incorporated into the cavity to increase the laser's quality factor. Active mode-locking at a frequency near 10 GHz is achieved via a Mach-Zender type electro-optic modulator in the cavity ring. The cavity length is about 108 m, yielding a free spectral range of about 1.85 MHz. Since some of the noise measurement schemes used involve mode-locking two lasers at the same frequency, small tunings of the free spectral range of the laser were necessary. To adjust the free spectral range, both dispersion and changing the physical cavity length were exploited. The cavity dispersion was utilized by tuning the intracavity optical bandpass filter to set the optical spectrum to where the target mode-locking frequency was a multiple of the longitudinal mode spacing. Fine tuning was achieved with a short free space section with one fiber launcher on a translation stage. The erbium based laser used is similar to the semiconductor laser in many respects, both cavities containing the same basic components, including an optical bandpass filter, electro-optic modulator, and an optical isolator. The erbium based laser's free spectral range is 1.68 MHz, close to that of the semiconductor based laser, indicating a cavity length of about 119 m.

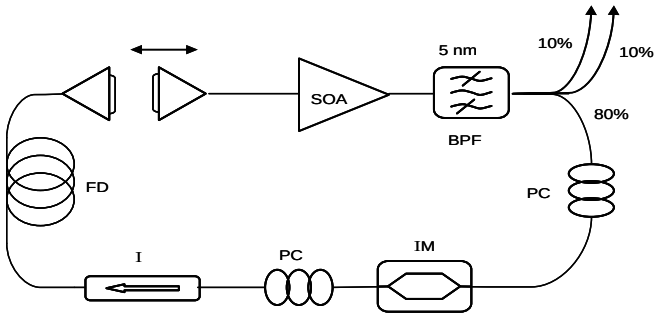


Figure 3.1: Semiconductor based fiberized ring laser schematic. BPF: bandpass filter; PC: polarization controller; IM: intensity modulator; I: isolator; FD 100 meter fiber delay; SOA: semiconductor optical amplifier

### *3.3 Frequency discriminator and relative noise measurements*

In order to determine if there is any significant filtering of the RF source noise by either laser, frequency discriminator (FD) measurements on all three devices were performed. The results are shown in Figure 3.2. Although the interference pattern of the FD measurement precludes precise knowledge of the absolute noise, it does not prevent the examination of the relative phase noise fall-off of the three devices. Beginning at frequencies below 100 kHz, there is a significant departure of the absolute phase noise of the semiconductor laser compared to that of the RF source indicating a filtering of the RF source noise when it is transferred onto the timing jitter for this laser. The absolute phase noise of the erbium laser is lower still, signaling a much lower cut-off frequency (and higher quality factor) than the semiconductor laser.

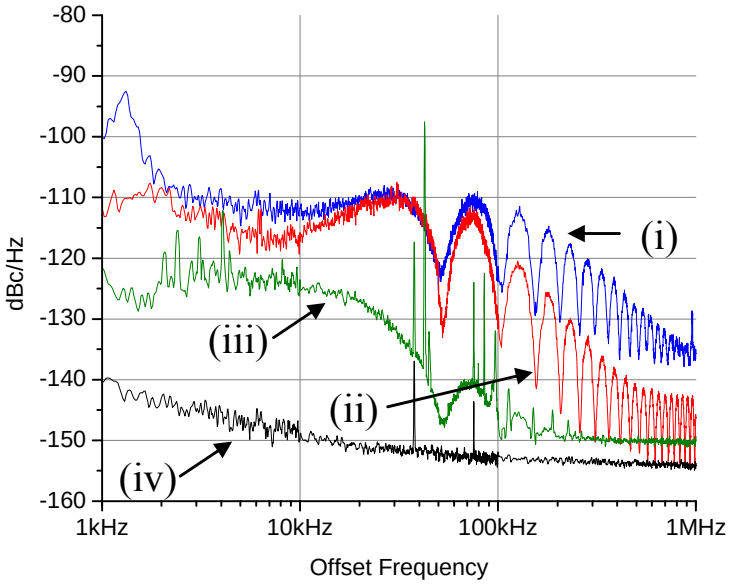


Figure 3.2: Frequency discriminator measurements of the RF source (i), the semiconductor laser (ii), and the fiber laser (iii). Curve (iv) is the noise floor.

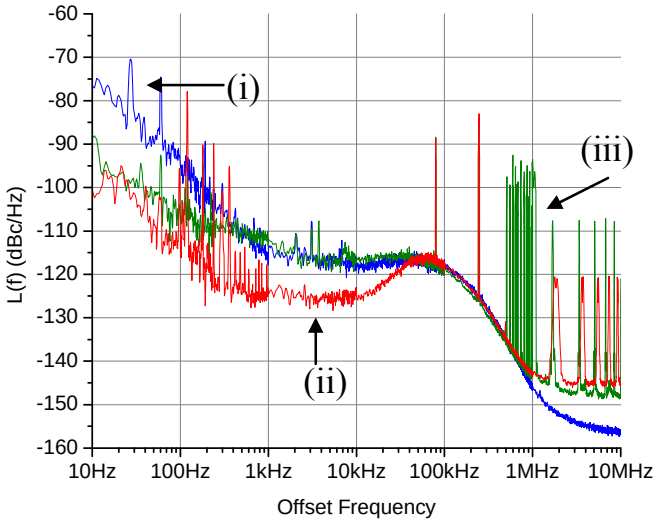


Figure 3.3: Residual noise measurements using the setup in Figure 2.4 of the semiconductor laser (ii), and the fiber laser (iii). The absolute noise of the rf source is shown in curve (i).

Figure 3.3 shows how this filtering manifests itself in the relative noise and demonstrates the necessity of distinguishing between relative noise and residual noise in high quality factor lasers. Here the semiconductor laser phase noise and the erbium laser phase noise, both measured relative to the RF source, are shown (the measurement setup is shown in Figure 2.4). Also, the absolute phase noise of the RF source (determined by using the three source method) is plotted for comparison. The filtering corner frequencies, estimated from FD measurements, are ~50 kHz and 5 kHz for the semiconductor laser and erbium laser, respectively. Regions of the relative noise spectrum for both lasers where filtering is significant are clearly dominated by the RF source absolute phase noise. For example, when the signal from the RF source is compared to the semiconductor laser, the absolute noise of the RF source begins to contribute to the relative noise at an offset of 10 kHz, and continues to do so out to 1 MHz. This is the noise bump in Figure 3.3, curve (ii). The effect of the RF source absolute noise on the erbium laser-RF source relative noise, as indicated by the equivalence of curves (i) and (iii), stretches from 1 kHz to 1 MHz. The noise spurs, multiples of 1.85 MHz on curve (ii) and multiples of 1.68 MHz on curve (iii), are the supermode noise spurs of the semiconductor laser and the erbium laser, respectively. Examining the absolute noise plots of Figure 3.2 and the relative noise plots of Figure 3.3 demonstrates the need to consider the laser's low noise application when evaluating phase noise. With the given RF source, the semiconductor laser would be preferred to the erbium laser when there is correlation between the phase noise of the RF source and the laser. On the other hand, if the reference by which the laser's phase noise is measured is uncorrelated, the lower absolute noise (excluding

supermode noise spurs) of the erbium laser dictates that it is preferable to the semiconductor laser.

Aside from these absolute and relative phase noise measurements, further investigations were made in which the filtering effect of a high quality factor laser was exploited. Two different setups were used, shown in Figure 3.4. The setup in Figure 3.4(a), where the signal generated from one laser is used to mode-lock another, is referred to as the "lasers in series" configuration and is capable of revealing otherwise obscured residual noise. Likewise, when the relative noise of two lasers driven by the same source is measured, the setup is referred to as the "lasers in parallel" configuration. This setup, shown in Figure 3.4(b), reveals information about the absolute noise of the semiconductor laser.

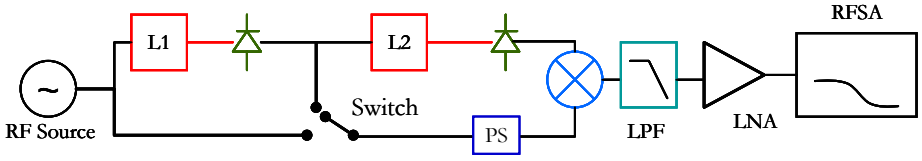


(a)

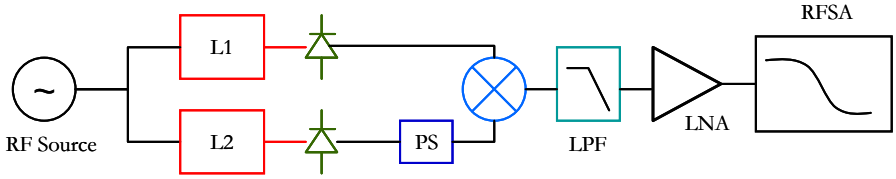


(b)

Figure 3.4: "In series" (a) and "in parallel" (b) measurement schematics. The noise of L2 in (a) can be measured relative to either the RF source or L1 depending on the position of the switch.

### *3.4 Lasers in Series Configuration*

When the absolute phase noise of an RF source has rolled-off to a level sufficiently low at the cut-off frequency of a mode-locked laser, no significant filtering of the RF source noise by the laser will take place. In this case, the relative noise will be dominated by the residual noise of the mode-locked laser. In lieu of such an RF source, the filtering effect of another laser with a higher quality factor can be used to generate a low absolute noise signal for mode-locking, thereby revealing the residual noise. The setup used to do this is shown in Figure 3.4(a). As shown, the RF source is used to mode-lock the erbium laser. The output of the erbium laser is photodetected, amplified, then used to mode-lock the semiconductor laser. The noise of the semiconductor laser can then be measured relative to either the erbium laser or the RF source. It should be noted that although the absolute phase noise of the signal from the erbium laser is quite low for frequencies below 1 MHz, strong supermode noise spurs at multiples of 1.68 MHz will feed into the semiconductor laser. Discussions of the noise measured for the "lasers in series" configuration are therefore separated into effects seen above 1 MHz and effects seen below 1 MHz. The semiconductor laser's noise relative to the erbium laser for frequencies below 1 MHz is shown in Figure 3.5(a). Note that the noise bump of Figure 3.3 is no longer present. Given the cut-off frequency of the semiconductor laser and the low absolute noise of the erbium laser's signal in this part of the noise spectrum, the relative noise of Figure 3.5(a) can only be the residual noise of the semiconductor laser. The semiconductor laser's phase noise relative to the RF source below 1 MHz is shown in Figure 3.5(b), where it is seen that the most of the noise spectrum is dominated by the RF source absolute noise.

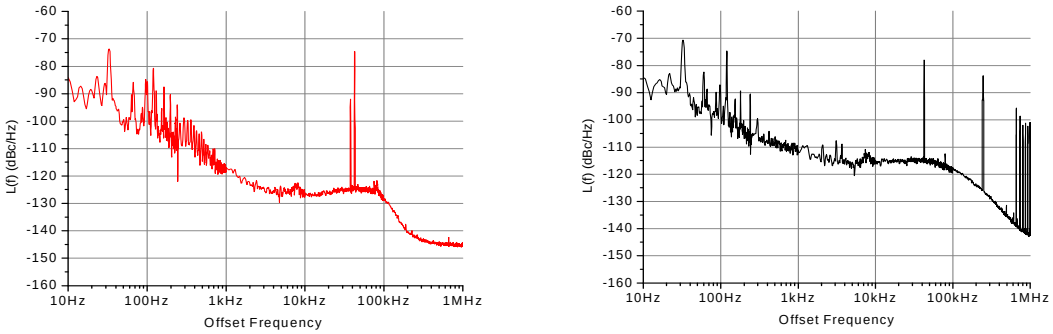


(a) (b)

Figure 3.5: "In series" phase noise measurements below 1 MHz. (a) Semiconductor laser noise relative to the erbium laser. (b) Semiconductor laser noise relative to the RF source.

As mentioned above, noise spectra of the semiconductor laser above 1 MHz will be influenced by the presence of the supermode noise spurs from the erbium laser. Figure 3.6(a) shows the semiconductor's phase noise relative to the erbium laser from 1 to 10 MHz. Two sets of supermode noise spurs are seen, the stronger set coming from the erbium laser, and the weaker set at multiples of 1.85 MHz are the supermode noise spurs of the semiconductor laser. The fact that the supermode spurs from the erbium laser appear in this noise measurement indicates that they may be filtered by the semiconductor laser. Whether or not this is so can be determined by examining the semiconductor phase noise relative to the RF source, shown in Figures 3.6(b) and 3.6(c). Here it is seen that the strength of the erbium laser's supermode spurs in the output of the semiconductor laser depends on the frequency separation from the supermode spurs

originating in the semiconductor laser. This interesting result indicates that the filtering effect is periodic with the periodicity equal to the free spectral range of the laser.

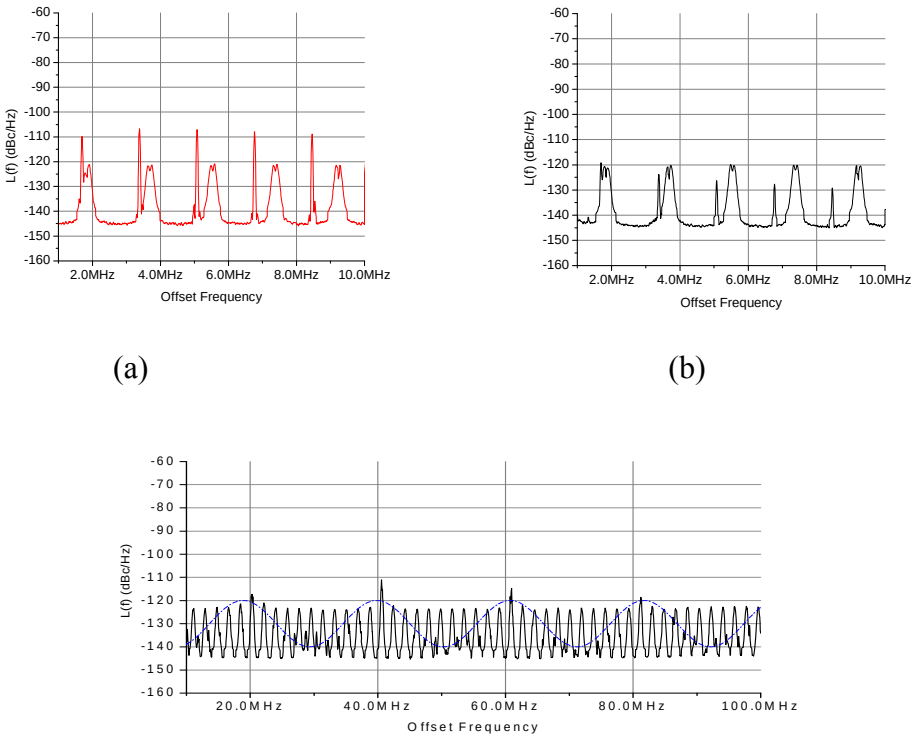


Figure 3.6: “In series” phase noise measurements above 1 MHz. (a) Semiconductor laser noise relative to the erbium laser, 1 MHz to 10 MHz. (b) Semiconductor laser noise relative to the RF source, 1 MHz to 10 MHz, where a filtering effect is apparent. (c) Semiconductor laser noise relative to the RF source, 10 MHz to 100 MHz, showing the periodicity of the filtering. The blue dotted line of (c) shows the varying strength of the erbium laser’s supermode spurs.

### *3.5 Lasers in Parallel Configuration*

New information can also be gleaned from high quality factor lasers when they are arranged "in parallel" as in Figure 3.4(b). If the two lasers are equivalent, this setup will reveal the residual noise of either laser (after a 3 dB correction). For lasers with very different absolute phase noise levels, the "lasers in parallel" configuration instead yields information about the absolute noise of the laser with the higher absolute phase noise. Results from Figure 3.2 show that the semiconductor based laser has a much higher absolute phase noise for offset frequencies 10 kHz to 1 MHz. The result of the "in parallel" measurement is shown in Figure 3.7(a). The absolute noise of the semiconductor laser dominates the noise measurement in the 10 kHz to 1 MHz range. To verify this, the measured data was multiplied by the FD transfer function of Equation 2.15 and compared to the FD measurement of the laser. The excellent agreement of the two plots is shown in Figure 3.7(b). The deviation of the two plots at large offset is due to the different configuration of amplifiers, both optical and electrical, used for the two measurements causing different noise floor levels. Note that unlike the FD measurement, the "in parallel" configuration reveals the absolute noise free of the interference pattern that precludes an accurate representation of the absolute noise.

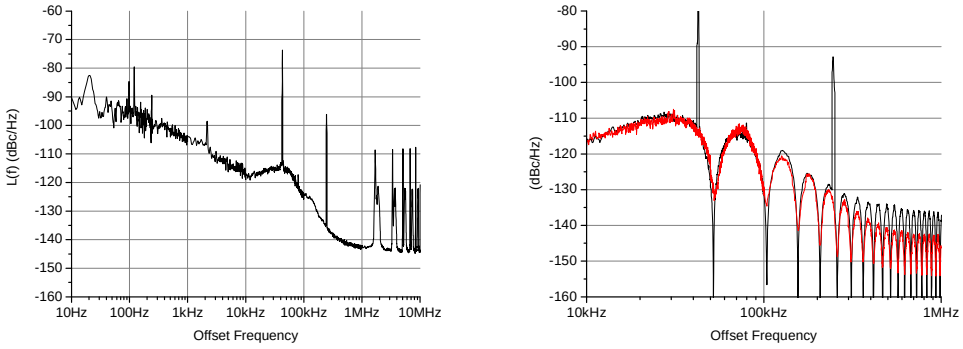


(a) (b)

Figure 3.7: (a) Lasers "in parallel" measurement and (b) the comparison of the "in parallel" measurement multiplied by the FD transfer function to the FD measurement of the SL. The red curve in (b) is the FD measurement, and the black curve is the lasers "in parallel" measurement multiplied by the FD transfer function.

In summary, investigations into the phase noise of high quality factor lasers showed how timing fluctuations relative to the signal used to mode-lock the laser can increase with the quality factor, although the absolute noise of the laser is decreased. Both the reduction of the absolute noise and the increase in the relative noise are due to the filtering of the noise spectrum of the RF driving source when that noise is transferred onto the timing jitter. Also, experiments were performed using two high quality factor lasers that took advantage of the filtering effect to reveal aspects of the residual and absolute phase noise of the laser with the lower quality factor. Furthermore, these experiments demonstrated that the filtering effect of harmonically mode-locked lasers is periodic, with a period corresponding to the free spectral range of the laser.

### *3.6 Ultralow jitter mode-locked laser*

With the availability of an ultralow noise RF source, running two lasers in series is no longer necessary to remove the noise bump in the relative phase noise. Additionally, the entire absolute noise spectrum of the synthesizer driven mode-locked laser can be measured without running two lasers in parallel. The semiconductor laser was rebuilt for use with the ultralow phase noise RF source. A schematic of the laser is shown in Figure 3.8. The laser, very similar to the one described in Section 3.2, is actively harmonically mode-locked at 10.24 GHz via loss modulation of a Mach-Zehnder type intensity modulator. The fiberized ring cavity uses a commercially available semiconductor optical amplifier (SOA) as the gain medium. A 100 meter fiber delay is included in the cavity to increase the laser cavity's quality factor. This sets the cavity length at about 110 m and the corresponding cavity fundamental frequency to 1.82 MHz. The straightforward cavity design helps maintain low loss, also important for maintaining a large quality factor. Note that unlike the laser of Figure 3.1, there is no bandpass filter in the laser cavity. Since there is large dispersion and no bandpass filter, the laser mode-locks at the wavelength where the modulation matches a multiple of the longitudinal mode separation. The laser employs no active feedback stabilization, but is encased in an insulated enclosure to isolate the laser from environmental perturbations.

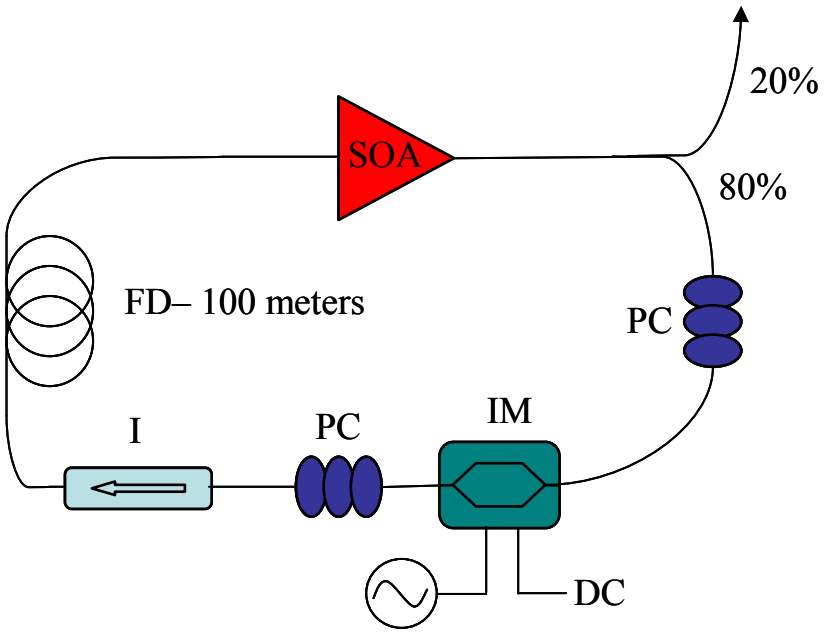


Figure 3.8: Laser Schematic. SOA: semiconductor optical amplifier; PC: polarization controller; IM: intensity modulator; I: isolator; FD: fiber delay

The similarities between this laser and the semiconductor laser of Section 3.2 suggest that this laser will also filter the RF source phase noise. Indeed, when the laser was driven by the Agilent synthesizer, it was discovered that not only are the absolute and relative phase noise affected, but the amplitude noise as well. The absolute phase noise of the mode-locked laser and the absolute phase noise of the synthesizer are shown in Figure 3.9. (The absolute phase noise of the laser was measured by comparing the synthesizer driven laser output to a sapphire loaded cavity oscillator (SLCO) and the absolute phase noise of the synthesizer was measured via the three source method.) As seen in the Figure, there is a clear departure of the laser noise from the synthesizer noise at offsets of 100 kHz and above. The functional form of this filtering given in Equation 2.1 is

$$S^{J}(\omega)=\frac{\Gamma^{2}}{(\omega)^{2}+\Gamma^{2}}S^{\phi}_{rf}(\omega). \tag{3.1}$$

The result of applying Equation 3.1 with Γ=170 kHz to the synthesizer noise is also shown in Figure 3.9. Note the excellent fit to the mode-locked laser absolute phase noise.

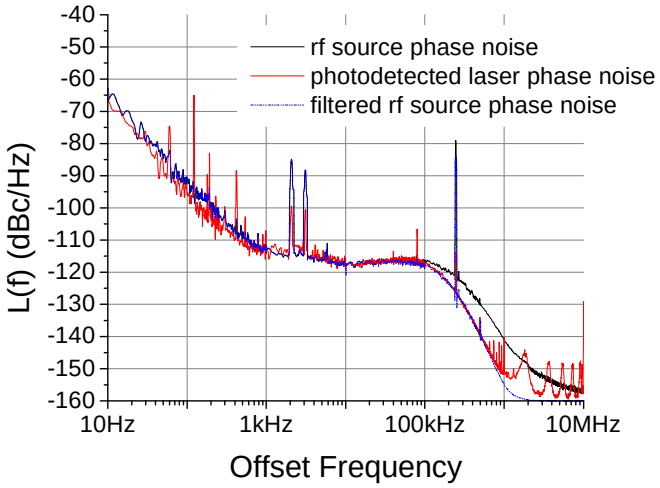


Figure 3.9: Absolute phase noise of the rf synthesizer and the mode-locked laser when driven by the RF synthesizer. Also shown is the RF synthesizer noise after the filter function of Equation 3.1 is applied.

While the absolute phase noise measurement reveals the amplitude response (magnitude squared) of the phase noise transfer function, no information about the phase of the transfer function is present. Recalling Equation 2.14,

$$S_{rel}(\omega)=S^{\phi}_{R}(\omega)\cdot\left[1+\left|H(\omega)\right|^{2}-2\left|H(\omega)\right|\cos(\theta(\omega))\right] \tag{2.14}$$

the transfer function phase response can be determined from a relative noise measurement. The relative noise and the application of Equation 2.14 to the synthesizer noise are shown in Figure 3.10. The filtering corner frequency Γ used is the same as in

Figure 3.9, namely 170 kHz. The phase response $\theta(\omega)$ used is $\Gamma/\omega$. Note the excellent fit to the noise bump of the relative noise measurement.

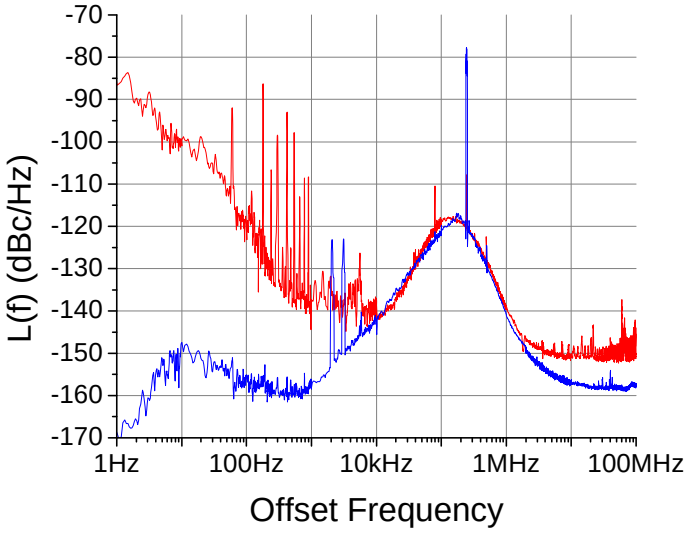


Figure 3.10: Mode-locked laser relative noise (in red) and Equation 2.14 applied to the synthesizer phase noise (blue).

Offset frequencies where there is a noise bump in the relative noise are frequencies for which the laser does not track the timing fluctuations of the modulation window of the loss modulator caused by timing fluctuations of the RF source. When the timing of the modulation window in the Mach-Zehnder modulator jitters at a rate that the laser pulses do not follow, the peak of the modulation window will vary its position relative to the mode-locked pulses. This leads to amplitude fluctuations as the pulses are transmitted through different parts of the loss modulation curve, creating phase to amplitude conversion of the synthesizer phase noise. The amplitude noise of the laser when the

synthesizer is used to mode-lock the laser is shown in Figure 3.11. Note that no such bump is observed in the amplitude noise of the synthesizer itself.

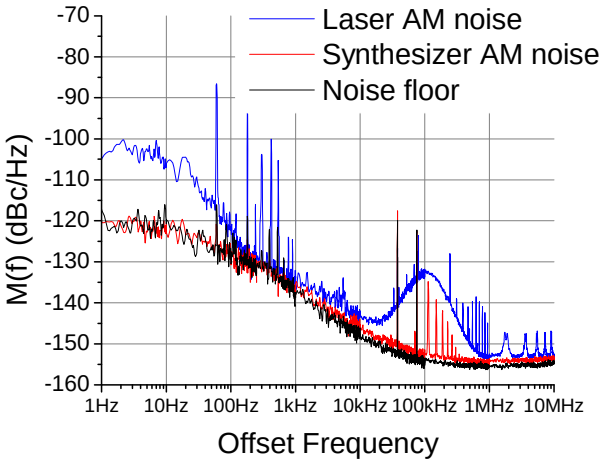


Figure 3.11: Amplitude noise spectrum of the mode-locked laser, synthesizer and noise floor. The bump in the laser amplitude noise originates in phase to amplitude conversion of the synthesizer phase noise.

To eliminate the noise bump in the relative noise measurement and create an ultralow jitter mode-locked laser, the Agilent synthesizer was replaced with the sapphire loaded cavity oscillator (phase noise = -156 dBc/Hz at 10 kHz offset) from Poseidon Scientific Instruments. Approximately 15 dBm of RF power from the SLCO was applied to the intensity modulator corresponding to a ~95% modulation index. The optimally tuned characteristics of the laser are shown in Figure 3.12. The SOA was biased at 500 mA resulting in an average output power of 17 mW. Since this output power is too large for our photodetector, the power on the photodetector was limited to 7 mW, generating -3.66 dBm of RF power at 10.24 GHz. The noise bump-free relative phase noise shown in

Figure 3.12(a) exhibits an approximately -10 dB/decade noise roll-off from 1 Hz to 40 kHz. After a slight rise to a level of -150 dBc/Hz at 100 kHz offset, the noise drops to nearly -160 dBc/Hz between the supermode spurs. The peaks of over 50 supermode spurs remain below -150 dBc/Hz, out to the 100 MHz measurement limit. Other spurs are of a technical nature, some being identified as harmonics of 60 Hz line noise, some originating from the fluorescent room lights, and some originating from computer monitors nearby. The associated timing jitter $\sigma_J$ can be obtained from the phase noise $L(f)$ by Equation 2.4. A timing jitter of 4.65 fs was obtained via integration of the phase noise spectrum from 1Hz to 100 MHz, the limit of the measurement capability. By averaging the power in a supermode spur and extrapolating to Nyquist, the integrated timing jitter to the Nyquist frequency of 5.12 GHz was estimated to be under 30 fs.

The pulse-to-pulse energy fluctuations were determined by measuring the amplitude noise sidebands on the 10.24 GHz photodetected laser output. Unlike the phase noise measurement, an electrical amplifier was used to measure the amplitude noise. The results are shown in Figure 3.12(b). Supermode spurs at a level similar to those seen in the phase noise measurement are present in the amplitude noise; however most of the noise spectrum is dominated by the amplifier noise and the noise floor of the AM detector. The large spur at 20 MHz offset originates in the electrical amplifier. The pulse-to-pulse energy fluctuation, determined by integrating the amplitude noise sidebands, is 0.0365% (1 Hz - 100 MHz).

Also of note is the optical spectrum of Figure 3.12(c) which displays 10.24 GHz spaced modes. The modes were not stable, however, and the visibility of these modes on the optical spectrum analyzer would wash out after a few seconds. The broad optical pulses

as measured directly from the laser output of Figure 3.9(d) contained a large negative linear chirp due mostly to the intracavity fiber dispersion. Using a dual grating compressor, the pulses were compressed to an autocorrelation FWHM of 5 ps.

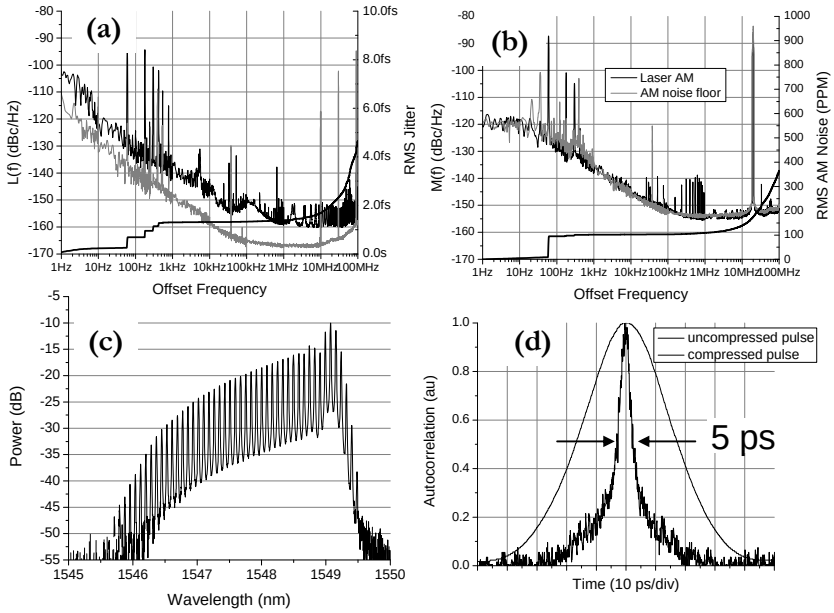


Figure 3.12: Laser characteristics when optimally tuned. (a) Relative phase noise, noise floor and integrated timing jitter, (b) amplitude noise, noise floor and integrated amplitude fluctuation, (c) optical spectrum, log scale, (d) pulse autocorrelation before and after external compression.

Important to achieving the low noise of the mode-locked laser is the optical power level both inside and coupled out of the laser cavity. A high intracavity power – by way of reduced linewidth – has been shown to reduce timing jitter of actively mode-locked lasers theoretically [14]. Specifically, it has been shown that the spontaneous emission contribution to the mean square timing jitter is proportional to the linewidth. The inversely proportional relationship between the optical power and the linewidth for single

mode lasers is well known [15], and the relationship has been shown to hold for each mode of mode-locked semiconductor lasers as well [34]. This relationship between the intracavity power and jitter will manifest itself in the phase noise measurement as the phase noise power of a supermode spur varying linearly with the inverse of the output power. Figure 3.13 shows the phase noise plots for SOA bias current levels of 200 mA and 300 mA. Clearly the supermode spur level decreases as the SOA bias, and therefore the optical power, is increased. The inset in Figure 3.10 shows the linearity of the phase noise power of a supermode spur to the inverse of the output power as the SOA bias is varied from 150 mA to 500 mA. Furthermore, at 500 mA bias, the output power is high enough to eliminate any need for external amplification prior to measuring the phase noise. This eliminates any noise associated with amplification [35] and lowers the noise floor of the phase noise measurement. This has lead the shot noise level, calculated to be ~160 dBc/Hz, to limit the noise performance between the supermode spurs.

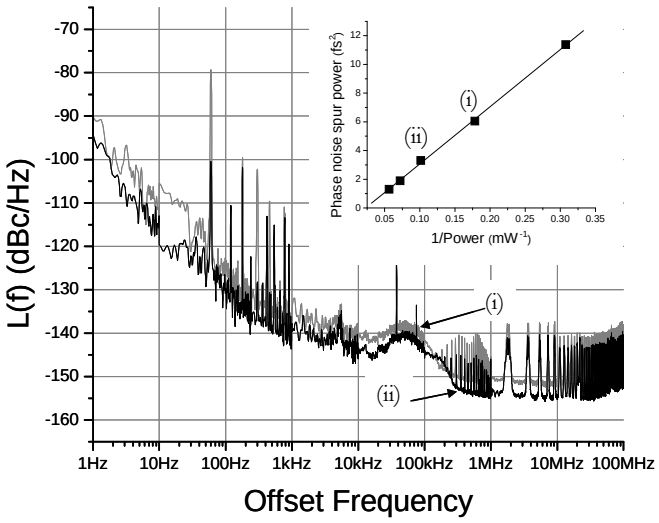


Figure 3.13: Phase noise for different SOA drive currents. (i) 200 mA, (ii) 300 mA. The phase noise power of the first supermode spur of these two curves along with those for gain biases of 150 mA, 400 mA and 500 mA versus inverse optical power and the best line fit are plotted in the inset.

In summary, a timing jitter of less than 5 fs (1 Hz - 100 MHz) was achieved with a semiconductor based actively mode-locked laser. The straightforward laser design requires no active feedback and uses only commercially available components. By extrapolating the noise out the Nyquist frequency the rms jitter is estimated to be under 30 fs. The amplitude noise, limited by the noise floor of the AM detector and the noise of an RF amplifier, is less than 0.0365%. The low noise is attributed to the high optical power level both inside and coupled out of the cavity, as well as the low noise of the SLCO. The low noise of the SLCO removes any phase noise filtering effect detrimental to not only the relative jitter, but to the pulse-to-pulse amplitude fluctuations as well.

### *3.7 Discussion and conclusion*

Low jitter mode-locked lasers that do not require optical frequency stabilization have found applications in high speed signal processing. Indeed, a laser very similar to the one described in Section 3.6 has been used for the generation of arbitrary RF waveforms [5]. Whether the description of the jitter should be in absolute or relative terms depends on the application. If the reference source is uncorrelated with the mode-locked laser, increasing the laser cavity length decreases both the influence of the RF source and the spontaneous emission contribution to the jitter. The situation is slightly different when the RF source used to mode-lock the laser is the master clock and the jitter relative to this RF source is important. Since the RF source contribution to the relative noise *increases* with a narrowing of the optical linewidth while the spontaneous emission contribution *decreases* with a narrowing of the linewidth, careful consideration must be taken when choosing an RF source and mode-locked laser.

The filtering of the RF source noise when it is transferred onto the timing jitter of an actively mode-locked laser can be understood in terms of the quality factor of the laser as follows. In the optical frequency domain, active mode-locking can be understood as the creation of sidebands about an optical longitudinal mode at a frequency offset equal to the mode-locking rate. When the frequency difference between the longitudinal mode and the created sideband equals a multiple of the longitudinal mode spacing, the sideband injection locks the two longitudinal modes. The locking bandwidth, that is, the range of RF frequencies for stable mode-locking, depends on the linewidth of the longitudinal modes, and therefore depends on the quality factor of the laser. In other words, as the quality factor increases, the range of RF frequencies that can influence mode-locking

decreases. This decrease in the range of RF frequencies manifests itself as a filtering of RF source noise when transferring that noise onto the timing jitter. Since sidebands created at any multiple of the longitudinal mode spacing can injection lock, RF noise centered at any multiple of the laser's free spectral range will influence the timing jitter. The filtering of RF source noise is therefore periodic with a periodicity equal to the laser's free spectral range and a cut-off frequency inversely proportional to the laser cavity quality factor.

It should also be noted that other effects can contribute to the low pulse-to-pulse timing jitter of a harmonically mode-locked laser such as presented in Section 3.6. It has been found that correlation among optical supermodes can reduce the contribution of supermode noise to the timing jitter [36].

# CHAPTER 4
# OPTICAL INJECTION LOCKING FOR SUPERMODE SUPPRESSION AND OPTICAL FREQUENCY STABILIZATION

## *4.1 Introduction*

For the laser in the last chapter, no effort was made to force the laser to select a single optical supermode and no effort was made to stabilize the optical frequencies. In order to select and stabilize a single optical supermode, external optical injection experiments were performed [37]. The principal behind injection locking for supermode suppression and optical frequency stabilization is to inject a low power optical signal from a stable CW source whose frequency matches a longitudinal mode of the mode-locked laser. This allows the injected longitudinal mode and consequently the optical supermode of which the longitudinal mode is a part to begin to dominate the laser gain. Other supermodes are then suppressed via gain saturation. Thus in the injection locked state, the laser produces a comb of frequencies anchored to the wavelength of the injected signal. Also, since only a single optical supermode dominates, noise associated with competition among optical supermodes can be suppressed. Two desirable outcomes may therefore be achieved simultaneously: supermode noise suppression and optical frequency stabilization.

In addition to the well studied optical injection locking of CW lasers [38], mode-locked lasers have been successfully locked to external sources both pulsed and CW. These studies have, among other things, shown how CW injection of a mode-locked laser can establish coherence between the CW injection laser and the mode-locked laser comb elements as well as narrowing the optical linewidth of the slave laser [39], [40]. However, the effects of CW optical injection on the supermode noise spurs effecting pulse-to-pulse

timing and energy fluctuations have not been previously considered. Moreover, long-term stabilization of injection locking must be achieved for the laser to be a viable comb source. Simulations and preliminary experiments on a scheme in which feedback is applied to the mode-locked laser cavity length are also presented in this chapter.

### *4.2 Optical injection locking experiments*

The experimental setup is shown in Figure 4.1. The mode-locked laser consists of a semiconductor optical amplifier (SOA) in a fiberized ring cavity. A 10.24 GHz RF signal is applied to a Mach-Zehnder type intensity modulator. A bandpass filter is included to force the lasing frequency to that of the injection seed. Polarization controllers are inserted prior to the modulator and the SOA, and an optical isolator ensures unidirectional operation. The cavity fundamental frequency is 11.8 MHz, corresponding to a cavity length of 17 m. The laser is mode-locked at ~870th harmonic; the optical spectrum therefore consists of 870 interleaved sets of 10.24 GHz-spaced comb lines when the laser is free running (no optical injection).

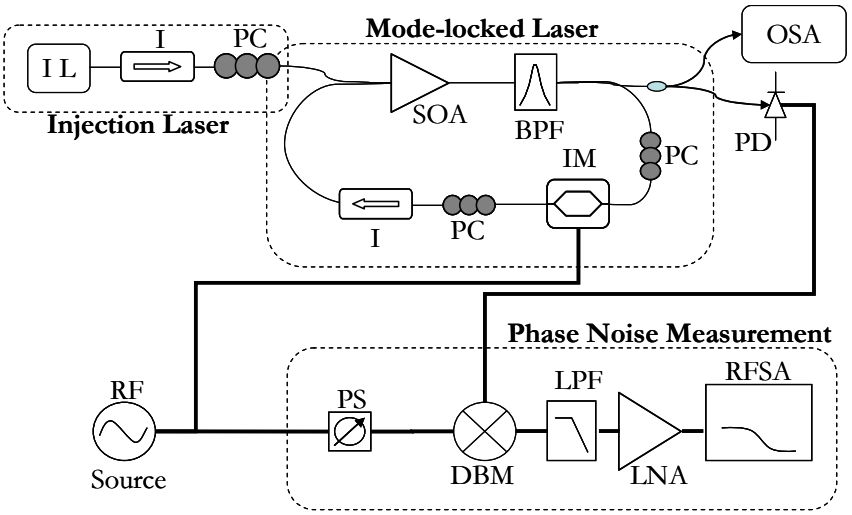


Figure 4.1: Experimental setup for optical injection and phase noise measurement. IL: injection laser; SOA: semiconductor optical amplifier; BPF: bandpass filter; PC: polarization controller; I: isolator; IM: intensity modulator; DBM: double balanced mixer; LPF: low pass filter; LNA low noise amplifier; PS: phase shifter; OSA optical spectrum analyzer; RFSA: RF spectrum analyzer

The injection seed laser is a commercially available, frequency stable, narrow linewidth laser. Given the mode-locked laser's mode separation of 11.8 MHz, the linewidth and stability requirements of the injection seed laser are quite stringent to ensure only single supermode set is injected and that lock can be maintained. Previous reports have shown how noise from an injection seed laser can be imparted onto a slave laser [41]. In anticipation of seeing a similar effect with our harmonically mode-locked laser, the intensity noise of our injection seed source was measured. The injection seed laser has a large intensity noise peak at 205 kHz, shown in Figure 4.2. As shown below, a similar noise peak emerges at 205 kHz offset from the 10.24 GHz photodetected carrier of the mode-locked laser when the laser is injection locked.

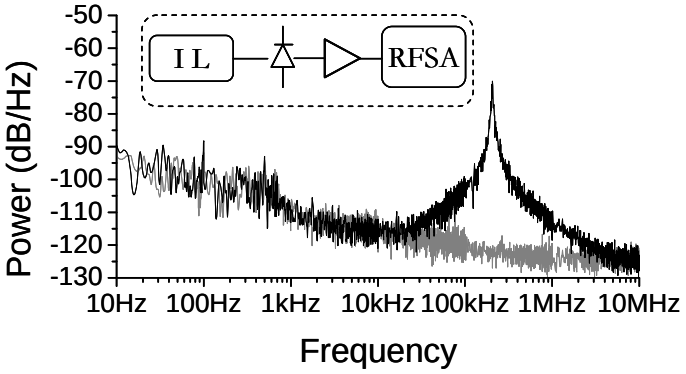


Figure 4.2: Injection laser intensity noise measurement setup (inset) and result.

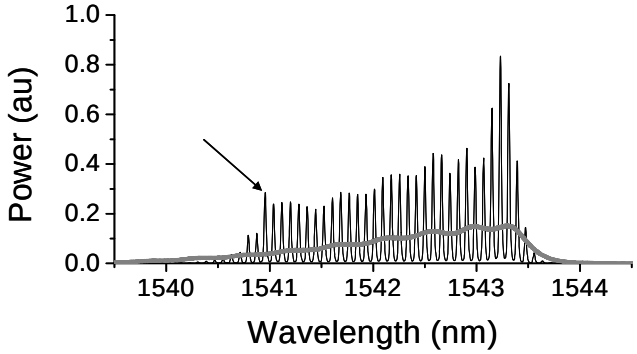


Figure 4.3: Optical spectrum of the mode-locked laser in free running (grey) and injection locked (black) states. The arrow indicates the injection wavelength.

Figure 4.3 shows the optical spectrum with and without external CW optical injection. The optical power injected into the mode-locked laser was ~19 μW and the average power of the mode-locked laser pulse train was 5 mW. Without injection, the spectrum is smooth, indicating the presence of many optical supermodes lasing simultaneously. Once the laser is injection locked, a single optical supermode begins to dominate the laser gain

and a high contrast 10.24 GHz-spaced phase locked comb emerges in the optical spectrum. The arrow in Figure 4.3 indicates the mode into which the master laser is injected.

Measurements of the pulse-to-pulse noise reduction are shown in Figures 4.4 and 4.5. Both the phase noise and the amplitude noise plots show a large reduction of the supermode noise – more than 20 dB – to levels below -140 dBc/Hz. Note the presence of a noise peak at 205 kHz in both the injection locked phase and amplitude noise that originates in the CW injection laser. The pulse-to-pulse timing jitter, obtained by integrating the phase noise from 10 Hz to 100 MHz, shows a drop from 127 fs in the unlocked state to 25 fs in the injection locked state despite the presence of the 205 kHz noise peak in the injection locked state.

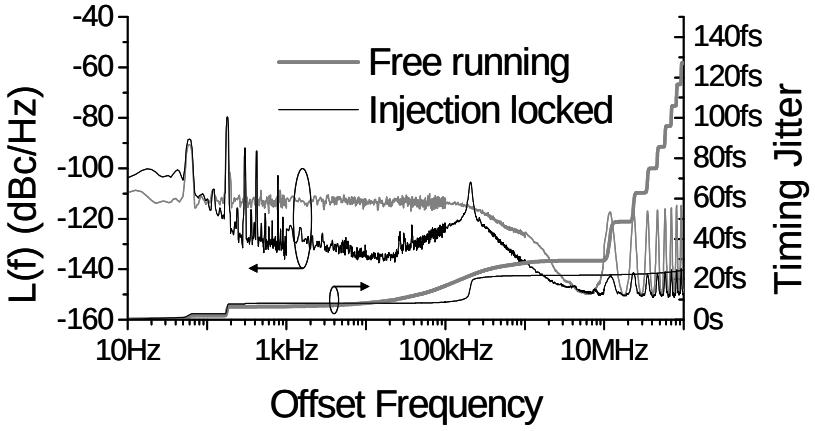


Figure 4.4: Phase noise and timing jitter of the mode-locked laser in free running and injection locked states.

Monitoring the polarization state of the injection laser and the mode-locked laser in both injection locked and free running states provided an indication to the source of the increase of the amplitude noise below 1 kHz offset. Although both the injection seed and the free running mode-locked laser's polarization states were constant, the polarization state of the injection locked mode-locked laser would drift. This drift is believed to arise when the mode-locked laser resonance becoming slightly detuned from the injection seed frequency because of thermal fluctuations in the mode-locked laser cavity as well as frequency fluctuations of the CW injection laser. Since the SOA's gain is polarization sensitive, changes to the polarization state caused small changes in the output power and consequently increased the low offset amplitude noise of the injection locked mode-locked laser. Despite the increase below 1 kHz, the amplitude noise decreased overall in the injection locked state, from 0.85% to 0.12%.

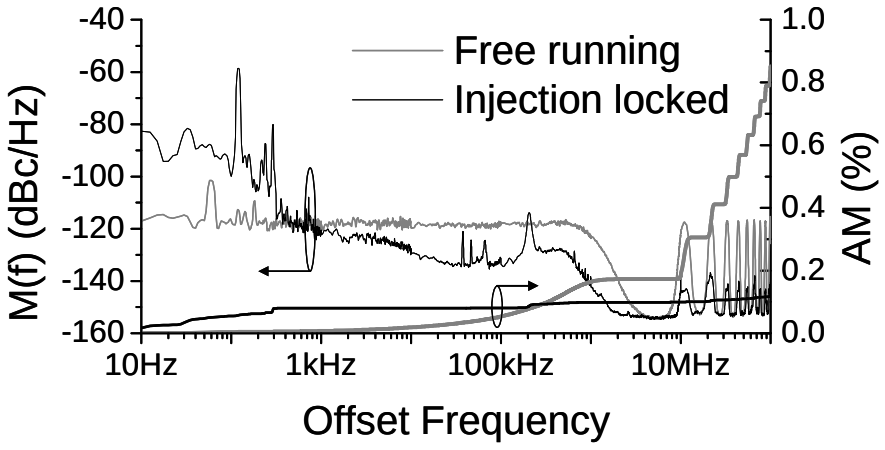


Figure 4.5: Amplitude noise of the mode-locked laser in free running and injection locked states.

The appearance of a bump in the relative phase noise with injection locking may indicate linewidth narrowing caused by injection locking. Unfortunately, the master oscillator's noise peak at 205 kHz makes it impossible to confirm the existence the same kind of phase noise bump seen in Chapter 3. Separate linewidth measurements were performed using heterodyne beating (for the case of no optical injection) and self-delayed heterodyne measurements (for the injection locked case). The results of these measurements are shown in Figure 4.6. When there is no optical injection, the mode-locked laser was beat with the same laser that was used for optical injection. Figure 4.6(b) shows the RF spectrum of the beat measurement when there is no injection locking. The spectrum contains the 10.24 GHz carrier and the supermode noise spurs as well as the master oscillator-mode-locked laser beat frequencies. The width of the longitudinal modes of the mode-locked laser without optical injection as determined by the beat signals is ~1.6 MHz. This broad linewidth contrasts greatly with the linewidth when the mode-locked laser is injection locked, shown in Figure 4.6(a). In the self-delayed heterodyne measurement used here, the optical signal under test is split into two arms, one arm is then frequency shifted and a large relative delay is imposed before the two arms are recombined using a directional coupler. To accurately measure the linewidth of an optical signal with this technique, the relative delay between the two arms must be greater than the coherence length of the signal. The relative delay between the two arms of the self-delayed heterodyne measurement setup used here was 18.53 km. Unfortunately, this was not enough to accurately measure the linewidth of the injection locked mode-locked laser. An upper limit estimate may be obtained, however, by assuming the relative delay is equal to the coherence length of the mode-locked laser.

This leads to an upper limit on the linewidth of ~10 kHz. For comparison, the same setup was used to measure the linewidth of the injection laser, also shown in Fig. 4.6(a). Note that the free running linewidth of ~1.6 MHz is more than two orders of magnitude broader than the injection locked laser. The narrowing of the optical linewidth of the mode-locked laser to the level of the injection seed is a major benefit of the injection locking technique.

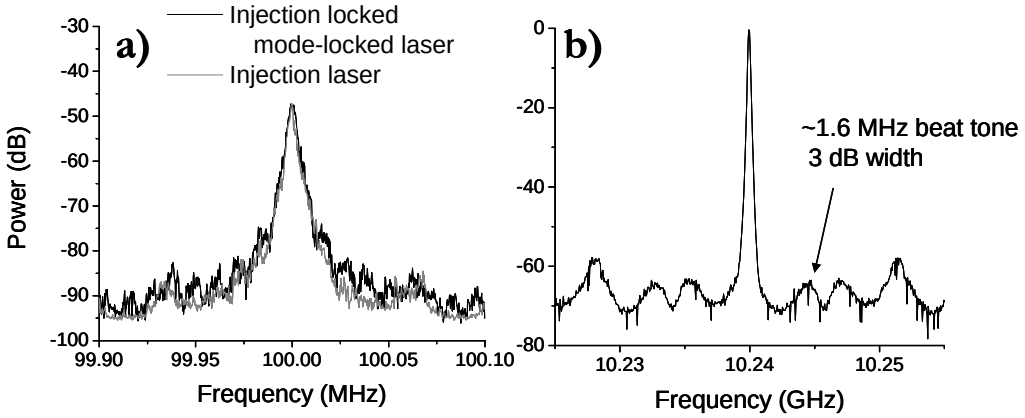


Figure 4.6: Linewidth measurements. a) Injection locked mode-locked laser and injection laser; b) free running mode-locked laser heterodyne beat linewidth measurement with four mode-locked laser-CW laser beat tones.

Additional measurements were made to ascertain the frequency stability of the injection locked mode-locked laser. The setup is shown in Figure 4.7. Prior to injection into the mode-locked laser, part of the injection signal is tapped off and frequency shifted 100 MHz. This frequency shifted signal is then beat with the output of the mode-locked laser. Figure 4.8 shows the strong stable beat signals at 20.38 GHz and 20.58 GHz that

demonstrate the high coherence between the injection laser and the mode-locked laser during the locking of the mode-locked laser's optical modes to the injection signal.

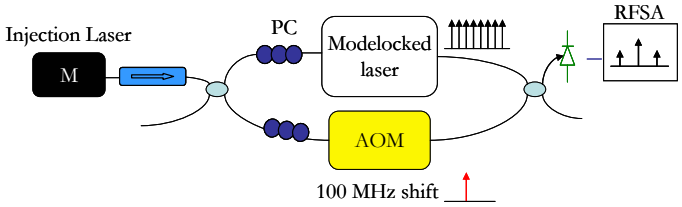


Figure 4.7: Setup for frequency stability of the injection locked laser measurement. AOM, acousto-optic modulator; PC, polarization controller.

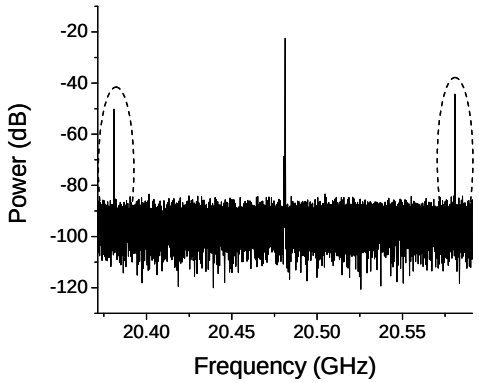


Figure 4.8: Frequency stability measurement. The beat tones are circled, the center tone is the second harmonic of the pulse repetition rate.

### *4.3 Long term locking scheme*

These initial experiments show the promise of injection locking for noise reduction, linewidth narrowing and frequency stabilization. However, maintaining lock to the injection seed for long durations still needs to be addressed for this technique to be a viable method for supermode suppression and frequency stabilization. A possible

stabilization scheme is shown in Figure 4.9. The essential idea is that of the Pound-Drever-Hall stabilization technique [42], except that instead of stabilizing a laser to a resonator, the resonator (the mode-locked laser) is stabilized to the injection seed. Prior to injection, the injection seed is phase modulated at a rate that is different from the mode separation of the mode-locked laser. In other words, if the injection seed frequency is within the injection locking bandwidth of a longitudinal mode of the mode-locked laser, the phase modulation sidebands do not lie within the locking bandwidth of other longitudinal modes. Within the injection locking bandwidth, the injection seed will experience a phase shift $\theta$ with detuning from resonance given by [38]:

$$\sin(\theta) = \frac{\omega_0 - \omega}{\Gamma} \tag{4.1}$$

where $\omega_0$ is the resonant frequency, ω is the frequency of the injected signal, and Γ is the locking bandwidth. Since the phase modulation sidebands do not injection lock other longitudinal modes, they will not experience the same phase shift. The phase shift of the injection seed relative to the phase modulation sidebands can be measured by mixing the photodetected signal with the phase modulation source. The voltage signal from the mixer will then be an error signal by which the mode-locked laser can be stabilized to the injection seed. In the proposed setup, the error signal is applied to a piezo driven fiber stretcher located in the cavity. Figure 4.10 shows the expected error signal from the output of the mixer, and Figure 4.11 shows an experimentally measured error signal for the case of the mode-locked laser run CW. Note the excellent agreement between the two plots.

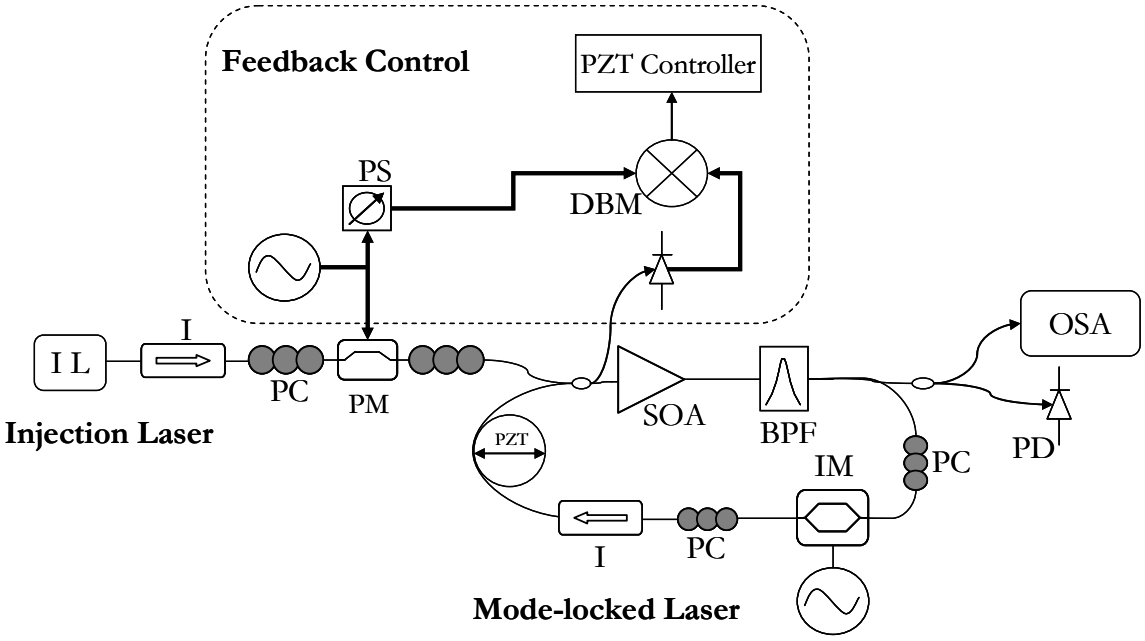


Figure 4.9: Proposed injection locking with a feedback loop to stabilize the mode-locked laser to the injection source. PS, phase shifter; PM; phase modulator; PC, polarization controller; IM, intensity modulator; PD photodetector, BPF; bandpass filter; PZT, piezoelectric transducer, I, isolator; OSA, optical spectrum analyzer; IL, injection laser; DBM, double balanced mixer; SOA, semiconductor amplifier.

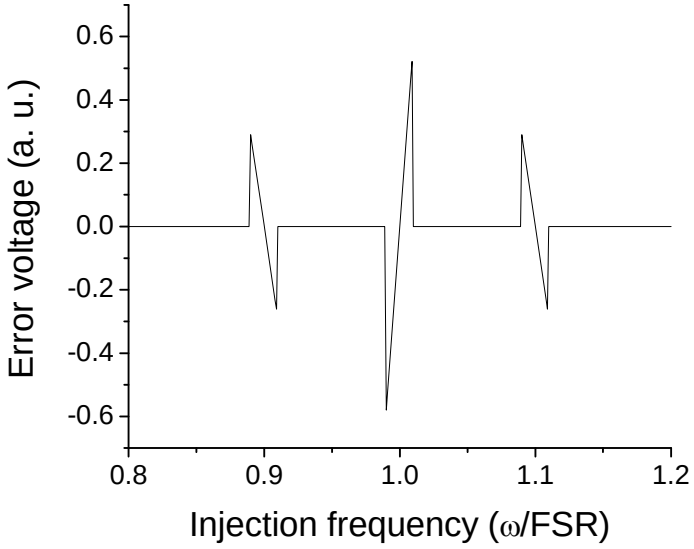


Figure 4.10: Simulation of the error signal derived from the setup in Figure 4.9. The phase shift of the injection laser follows Equation 4.1 with Γ equal to 0.01·FSR and the phase modulation rate equal to 0.1·FSR. Note the linear response of the signal near resonance.

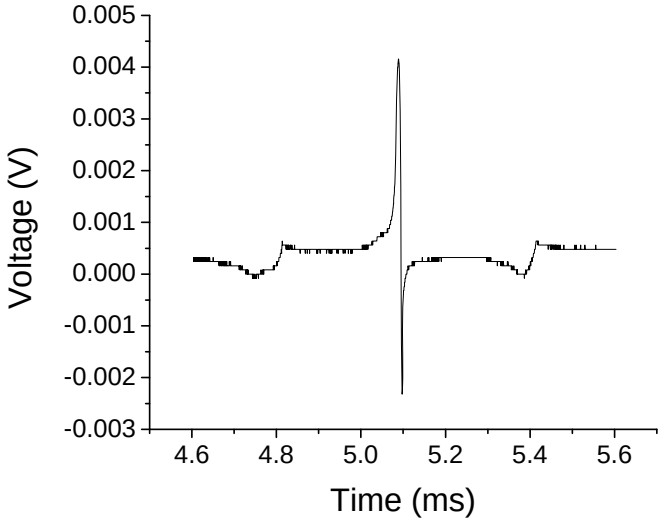


Figure 4.11: Measured error signal while the slave laser is run CW.

In summary, supermode noise spurs were reduced more than 20 dB in the photodetected amplitude and phase noise of a harmonically mode-locked laser via CW injection and the pulse-to-pulse timing jitter and amplitude noise were reduced from 127 fs to 25 fs, and 0.85% to 0.12% (10 Hz- 100 MHz), respectively. The noise reduction is accompanied by the emergence of a high contrast 10 GHz optical frequency comb locked to the injection seed and the reduction of the linewidth of the optical modes to the level of the injection seed. With the proposed technique for long term stabilization, injection locking can be a viable method for frequency stabilization and supermode noise suppression in harmonically mode-locked lasers.

# CHAPTER 5
# INTRACAVITY ETALON FOR SUPERMODE SUPPRESSION AND OPTICAL FREQUENCY STABILIZATION

## *5.1 Introduction*

Another method for supermode selection and frequency stabilization that has shown to be quite successful is placing a Fabry-Perot etalon (FPE) inside the laser cavity [25], [43], [44]. In the frequency domain, the etalon may be described as a periodic bandpass filter. When the mode-locking rate equals the etalon free spectral range, the filtering action of the etalon removes all but a single optical supermode. Not only does this produce an optical frequency comb with frequency separation equal to the mode-locking rate, it also eliminates the timing jitter and pulse-to-pulse energy fluctuation noise associated with the competition among supermodes. Without stabilization of the laser cavity however, any optical cavity length change brought on by environmental influences will cause fluctuations in the optical frequencies. These frequency fluctuations can destabilize the mode-locking as the optical frequencies become detuned from the transmission windows of the FPE. The mandatory stabilization of the optical frequencies can be performed with a Pound-Drever-Hall (PDH) stabilization loop that uses the same intracavity etalon that suppresses the supermode noise [25], [42]. The essence of the PDH stabilization method is pictured in Figure 5.1. A laser line to be stabilized is phase modulated and reflected off a Fabry-Perot etalon. By setting the laser frequency near a transmission peak while the sidebands reside in the reflection band of the etalon, the laser line experiences a phase shift the sidebands do not as the laser frequency fluctuates. By mixing the photodetected reflected signal with the source used to modulate the laser, an error signal can be derived.

This error signal is conditioned and applied to an actuator in the laser cavity. By incorporating PDH stabilization with the intracavity FPE, supermode suppression and optical frequency stabilization are achieved simultaneously with a single etalon.

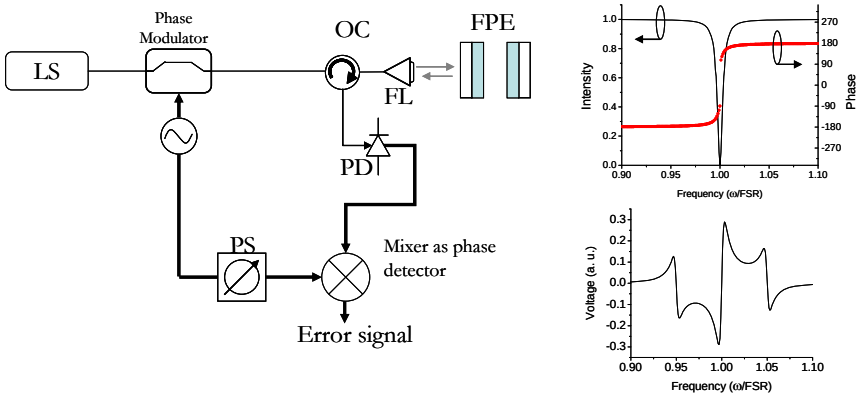


Figure 5.1: Pound-Drever-Hall laser frequency stabilization. The schematic on the left shows the basic setup. The upper right graph shows the phase and amplitude response of one of the resonances of the etalon in reflection. The lower right shows the derived error signal. LS, laser source; OC, optical circulator; FPE, Fabry-Perot etalon; PS, phase shifter; FL, fiber launcher; PD, photodetector.

In the following section an intracavity etalon-based actively mode-locked laser with ultralow timing and amplitude jitter is described. This laser represents a marked improvement in noise performance over previous similar lasers [25]. Section 5.3 describes a modification to the laser resulting in an increase in optical bandwidth by more than a factor of two. In Section 5.4 some comments are made regarding the use of an ultralow noise RF source for mode-locking and Section 5.5 summarizes the work presented in this chapter.

### *5.2 Intracavity etalon-based actively mode-locked laser experiments*

An actively mode-locked laser incorporating an etalon and PDH stabilization was built and characterized. The laser system schematic is shown in Figure 5.2. The fiberized laser cavity uses a commercially available semiconductor optical amplifier as the gain medium. The cavity fundamental frequency is 44 MHz, corresponding to a roundtrip cavity length of about 4.5 m. A free space section with a polarization beam splitter and air gap Fabry-Perot etalon (finesse ~100) with three low thermal expansion coefficient spacers serve to suppress unwanted optical supermodes and generate the PDH error signal. Without the inclusion of the etalon, ~233 optical supermodes can lase simultaneously. The mode-locking frequency is set equal to the free spectral range of the FPE, 10.24 GHz, which is ~233$^{rd}$ harmonic of the cavity fundamental frequency. The average output power is around 5 mW. To generate the PDH error signal, 10% of the output is tapped off and phase modulated. After phase modulation the output is injected into the free space section of the laser cavity with polarization orthogonal to the intracavity light. The phase modulation rate is set to 500 MHz, comfortably in the reflection band of the etalon.

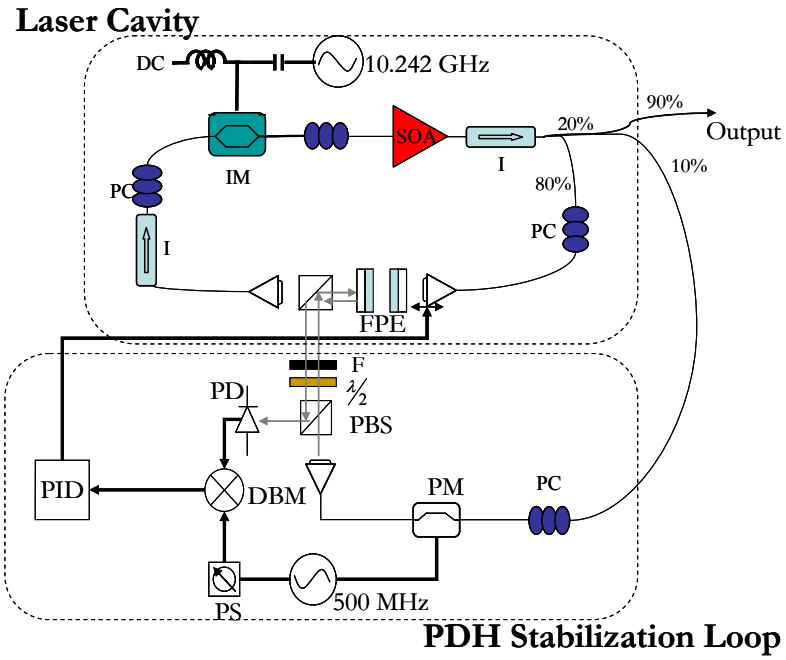


Figure 5.2: Laser cavity and optical frequency stabilization schematic. I, isolator; IM, intensity modulator; FPE, Fabry-Perot etalon; PC, polarization controller; PM, phase modulator; F, Faraday rotator; $\lambda/2$, half-wave plate; DBM, double balanced mixer; PS, phase shifter; PD photodetector; PID, PID controller. Grey arrows indicate feedback loop beam path in free space.

The optical spectrum is shown in Figure 5.3. In Figure 5.3(a) the full spectrum with an OSA resolution limited frequency comb is shown. A high resolution optical spectrum of a single comb line (resolution = 1 MHz) showing the high optical signal-to-noise ratio (OSNR) is shown in Figure 5.3(b). The nearest neighbor longitudinal mode is suppressed to a level 50 dB below the dominant mode.

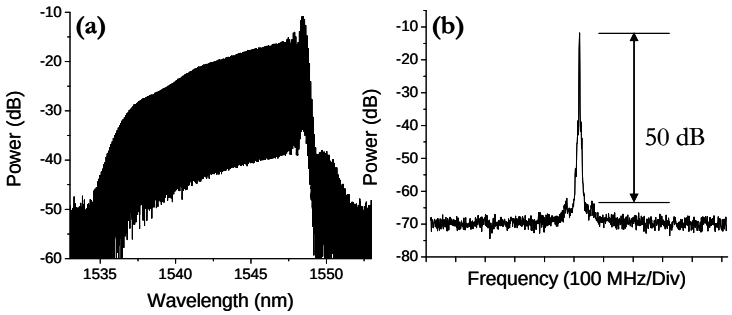


Figure 5.3: Optical spectrum. a) Full spectrum showing resolution limited comb visibility. b) High resolution spectrum showing 50 dB OSNR of a single mode.

A frequency stability measurement of the PDH stabilized laser source was performed by monitoring the stability of a photodetected beat signal between a stable, narrow linewidth CW laser and one of the modes of the PDH stabilized source. The fluctuation of the beat frequency contains contributions from both the PDH stabilized laser and the CW laser, therefore the fluctuation of the beat frequency yields an upper limit on the instability of the PDH stabilized source. Also, the narrow linewidth of the CW source (~1 kHz) allows estimation of the linewidth of the optical frequencies of the mode-locked laser. The results of these measurements are shown in Figure 5.4. In Figure 5.4(a) the width of the beat frequency, and therefore the linewidth of a mode of the mode-locked laser, is limited to the resolution bandwidth of the spectrum analyzer of 10 kHz. Figure 5.4(b) demonstrates the optical frequency stability of the mode-locked laser. A maximum hold for 30 seconds of the RF spectrum shows a maximum deviation of only 360 kHz.

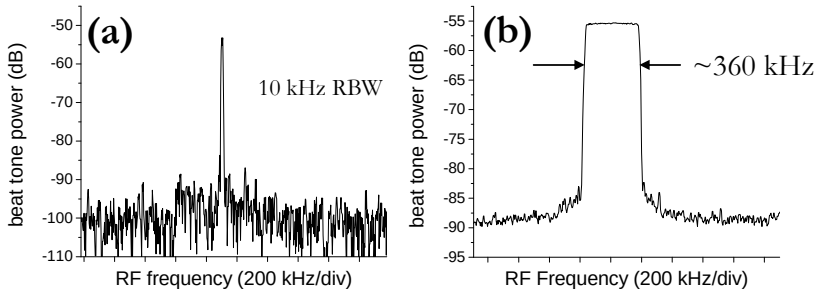


Figure 5.4: PDH stabilized laser source linewidth and frequency stability measurements. In (a), the linewidth was limited by the spectrum analyzer resolution bandwidth of 10 kHz. In (b), the spectrum analyzer was set to maximum hold for 30 seconds.

The time domain characteristics of the stabilized source were also measured. In Figure 5.5 are the measurements of the pulse-to-pulse timing jitter, pulse-to-pulse energy fluctuations, autocorrelation trace and sampling scope trace. The RF carrier phase noise was measured relative the RF source used to mode-lock the laser. Figure 5.5(a) shows an integrated timing jitter (1 Hz-100 MHz) of 5 fs. The first supermode noise spur peaks at -145 dBc/Hz and the second supermode noise spur is in the measurement noise floor. This indicates that the supermode noise spurs are well suppressed by the inclusion of the intracavity FPE. The supermode noise spur level roll-off and a shot noise level in a quadrature component calculated to be -157 dBc/Hz lead to an estimated timing jitter integrated from 1 Hz to the Nyquist frequency of 5.12 GHz of only 20 fs. The integrated pulse-to-pulse energy fluctuation (1 Hz -100 MHz) in Figure 5.5(b) is 0.04% and is mostly measurement noise floor limited. Also of note are the externally compressed pulses (compressed with a dual grating pulse compressor) with an autocorrelation FWHM of 1.5 ps shown in Figure 5.5(c). The large wings in the autocorrelation trace

indicate large higher order chirp. The pulse train sampling scope trace is shown in Figure 5.5(d).

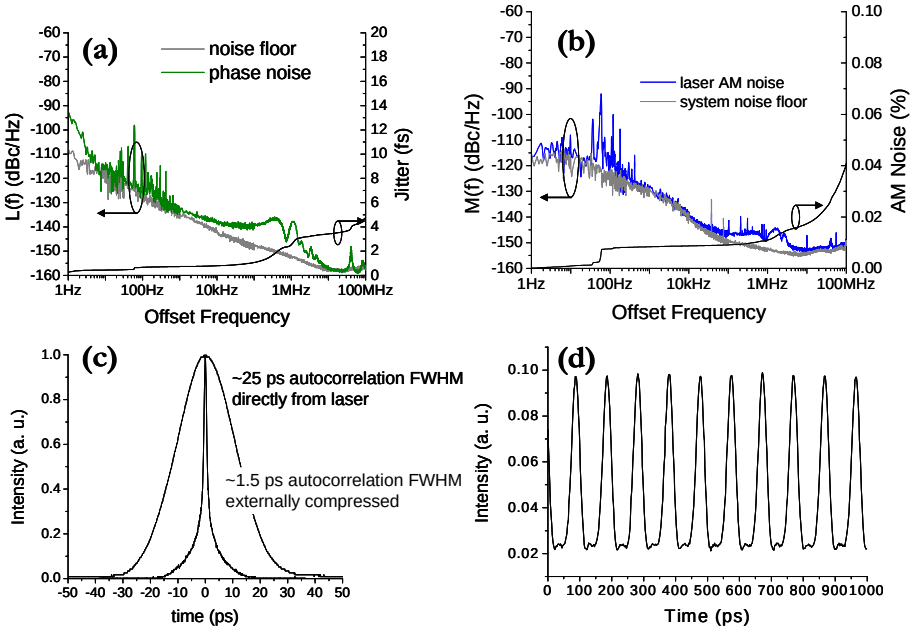


Figure 5.5: Time domain characteristics. a) Phase noise and timing jitter; b) AM noise and percent pulse-to-pulse energy fluctuation; c) autocorrelation trace; d) sampling scope trace.

### *5.3 Intracavity etalon-based actively mode-locked laser with DCF*

Subsequent to these experiments, a 43 cm length piece of dispersion compensating fiber (DCF) was incorporated into the laser cavity just before the intensity modulator in attempt to reduce the overall cavity dispersion. The laser optical spectrum when DCF is incorporated is shown in Figure 5.6. In Figure 5.6(a), a -10 dB bandwidth of 16 nm with OSA resolution-limited comb visibility is shown. The 16 nm bandwidth contains 195 phase correlated optical modes spaced by 10.24 GHz, significantly broader than the

optical spectrum when no DCF is used. A high resolution optical spectrum showing the high OSNR is shown in Figure 5.6(b). The exhibited OSNR is greater than 40 dB and is limited by the noise floor of the high resolution spectrum analyzer. Note that optical modes spaced by the cavity fundamental frequency of 34 MHz are not visible, having been suppressed below the noise floor of the high resolution spectrum analyzer.

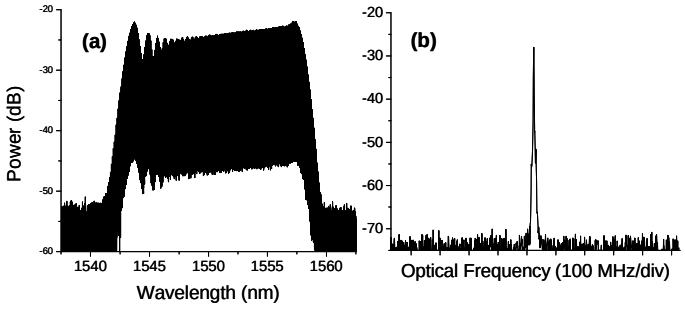


Figure 5.6: PDH stabilized laser with DCF optical spectrum. a) Full spectrum showing a -10 dB width of 16 nm; b) high resolution optical spectra showing > 40 dB OSNR of a single mode.

The optical frequency stability of the mode-locked laser with DCF was also measured in the same manner described in Section 5.2. These results are shown in Figure 5.7. As in Figure 5.5, the width of the beat tone is limited by the resolution of the measurement of 10 kHz. As shown in Figure 5.7(b), a maximum hold on the RF spectrum analyzer shows a maximum deviation in 30 seconds of only 780 kHz. Again, due to fluctuations of the CW laser used in this measurement, the maximum deviation of Figure 5.7(b) should be taken as an upper limit.

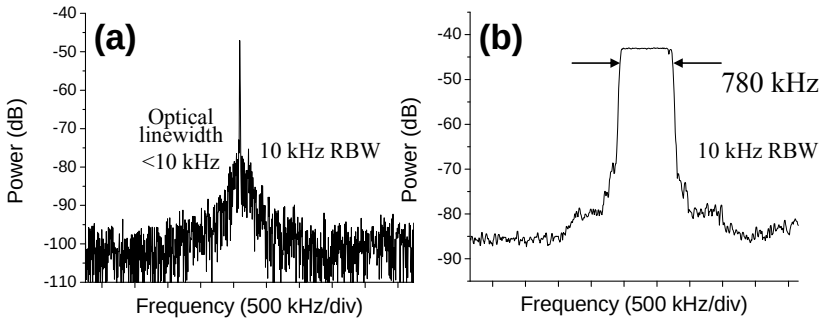


Figure 5.7: PDH stabilized laser with DCF linewidth and frequency stability measurements. In (a), linewidth was limited by the spectrum analyzer resolution bandwidth of 10 kHz. In (b), the spectrum analyzer was set to maximum hold for 30 seconds.

The time domain characteristics of the source with DCF incorporated were also measured. Figure 5.8 shows the measurements of the pulse-to-pulse timing jitter, pulse-to-pulse energy fluctuations, autocorrelation trace and sampling scope trace. Figure 5.8(a) shows an integrated timing jitter (1 Hz-100 MHz) of 11.4 fs. The supermode noise is slightly higher than without the DCF. The first supermode noise spur peaks at -143 dBc/Hz and the second supermode noise spur peaks at -150 dBc/Hz. The supermode noise spur level roll-off and a shot noise level in a quadrature component calculated to be -155 dBc/Hz lead to an estimated timing jitter integrated from 1 Hz to the Nyquist frequency of 5.12 GHz of 31 fs. The integrated pulse-to-pulse energy fluctuation (1 Hz - 100 MHz) in Figure 5.8(b) is 0.046% and again is mostly measurement noise floor limited. The externally compressed pulses have an autocorrelation FWHM of 880 fs and are shown in Figure 5.8(c). Note that the large wings seen in Figure 5.5(c) are no longer apparent. The pulse train sampling scope trace shown in Figure 5.8(d).

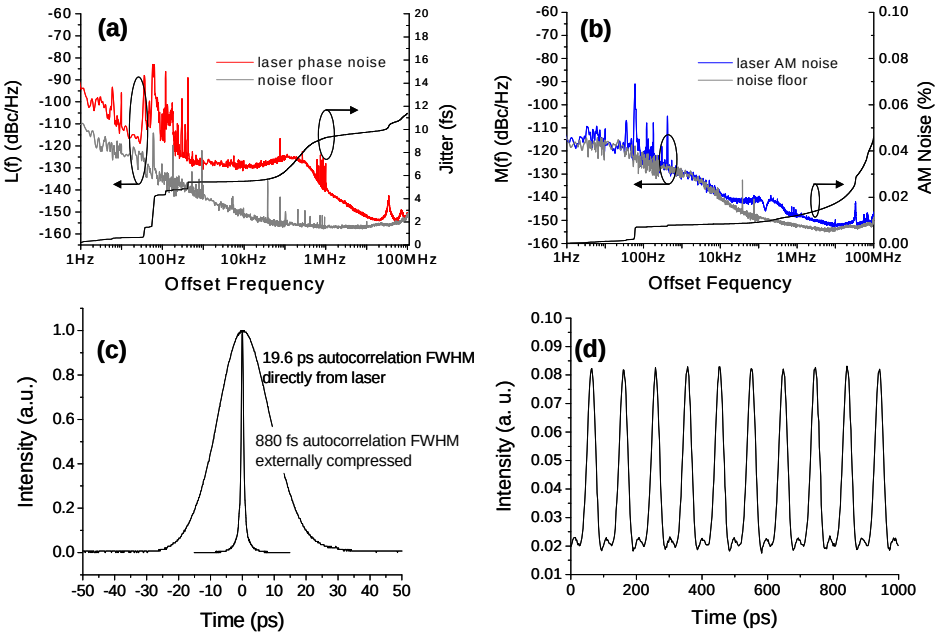


Figure 5.8: Time domain characteristics with DCF. a) Phase noise and timing jitter; b) AM noise and percent pulse-to-pulse energy fluctuation; c) autocorrelation trace; d) sampling scope trace.

### *5.4 Comments on using low noise RF sources with etalon-based actively mode-locked lasers*

It must be kept in mind that the timing jitter noise spectra of Section 5.2 and 5.3 are residual noise spectra. The absolute timing jitter noise spectra will be dominated by the Agilent source used to mode-lock the laser. Also, part of the amplitude noise of Figure 5.5(b) and Figure 5.8(b) may be due to Agilent source phase noise coupling to amplitude noise of the pulse train as described in Chapter 3. In order to lower the absolute timing jitter of the etalon-based mode-locked laser, an ultralow noise RF source, such as the SLCO, must be used. The difficulty then becomes matching the free spectral range of the

etalon to the frequency of the ultralow phase noise RF source, since neither are easily tuned. It is possible to measure the free spectral range of an etalon very precisely [45], but to then correct the free spectral range requires its disassembly and polishing of the spacer(s) with high precision. The iterative process of measuring the free spectral range of an etalon, disassembly, repolishing, assembly and re-measure has been limited to etalons with flat mirrors. Unfortunately, diffraction losses of flat mirror etalons limit the finesse to 100-200. This means that a laser with a curved mirror etalon with a finesse ~1000 that would otherwise improve laser performance (since the laser cavity length could be decreased while still supporting only one optical supermode) would be extremely difficult to use with an ultralow noise RF source. This creates a serious limitation to improvements to the intracavity etalon-based actively mode-locked laser. The following chapter outlines a different technique that allows for the generation of an optical frequency comb from a semiconductor-based laser that does not have this limitation.

### *5.5 Summary*

In summary, by incorporating a Fabry-Perot etalon into a harmonically mode-locked laser, a frequency stable, narrow linewidth comb source can be produced. A timing jitter of only 20 fs (1 Hz-5.12 GHz) and a maximum frequency deviation of an optical mode of 360 kHz were obtained. By adding a short piece of dispersion compensating fiber into the cavity, the optical spectrum was broadened to ~2 THz. This corresponds to nearly 200 GHz-spaced phase locked frequencies. Moreover, the compressed pulse width was reduced to below one picosecond. The high quality output characteristics were maintained for hours at a time, limited only by the dynamic range of the piezoelectric

driven translation stage. The short pulse, low timing jitter, high OSNR, broad optical spectrum stabilized to well below 1 MHz output of this laser make it well suited to serve as a OCDMA, WDM, OTDM, source. These qualities also make this source ideal for signal processing applications such as waveform generation and analog-to-digital conversion.

# CHAPTER 6
# THE ETALON-BASED COUPLED OPTOELECTRONIC OSCILLATOR

## *6.1 Introduction*

In Chapter 3, the action of a mode-locked laser on the phase noise of an RF source was described. It was found that a mode-locked laser is capable of filtering the source phase noise when transferring it onto the timing jitter. The analysis was conducted by considering the laser and photodetector as a single RF component described by a phase noise transfer function. In this analysis, the laser acts as an electrical filter with a high quality factor, or Q value, defined as [46]

$$Q = \frac{f_0}{2\Gamma} \tag{6.1}$$

where $f_0$ is the resonant frequency of the filter (in this case the mode-locking rate) and $\Gamma$ is the filter's half-width at half maximum (HWHM) bandwidth. Such a conception of a mode-locked laser as a high Q microwave component has lead to a unique microwave oscillator known as the coupled optoelectronic oscillator (COEO) [47][44]. Unlike traditional RF oscillators, low jitter optical pulses are produced in addition to a low noise electrical signal. The conventional COEO is not however a stabilized frequency comb source. On the other hand a COEO designed around a mode-locked laser with an intracavity etalon should be able to produce a stabilized multi-gigahertz spaced comb. Additionally, such an oscillator should not suffer from difficulties related to matching the etalon free spectral range to the frequency of an RF source since in a COEO design there is no separate RF source. Not only can the RF source for mode-locking be eliminated, but

it is also possible to remove the source necessary for the generation of the Pound-Drever-Hall laser frequency stabilization. This results in a semiconductor-based, completely self contained low jitter multi-gigahertz spaced stabilized frequency comb source. In this chapter, the analysis and experimental realization of such a source are presented. In the following section, the differences between the conventional COEO and the etalon-based COEO are discussed. Section 6.3 reports experimental results on an optical frequency self-stabilized COEO. Improvements on this source are described in Section 6.4 where the pulse repetition rate is also stabilized. The feedback design for stabilization is justified by the measurements of the fixed point frequencies in Section 6.5.

### *6.2 The conventional COEO and. the intracavity etalon-based COEO*

A diagram of a conventional COEO is shown in Figure 6.1, and a detailed description of such an oscillator can be found in [47]. The major segments of the COEO are the optical loop designed for mode-locking through loss modulation, and an optoelectronic feedback loop. The optical loop is simply a laser cavity like that of Chapter 3, but the RF source has been replaced by the optoelectronic feedback loop. The generation of a low noise RF signal and optical pulses build from noise, roughly described as follows. When the laser output is photodetected, the beat signals from different longitudinal modes are detected. One of these beat signals is selected with an RF filter, amplified, and with a properly adjusted phase, used to drive the loss modulator in the optical cavity. The modulation reinforces the strength of that particular photodetected beat signal which is amplified, drives the modulator and so on. Provided there is enough gain for the RF signal, oscillation will occur for the photodetected beat tone selected by the RF filter.

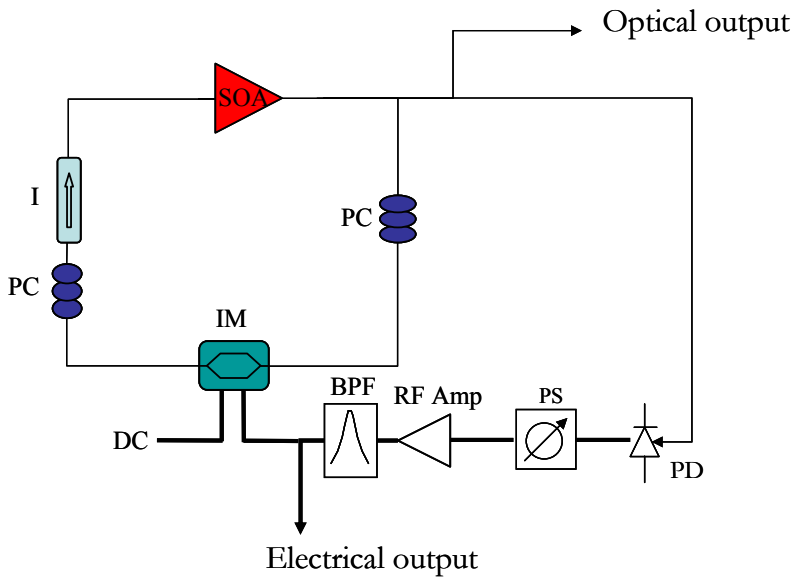


Figure 6.1: The convention al coupled optical electronic oscillator. The oscillator produces a low noise RF signal and a train of low noise optical pulses.

Just as a conventional COEO can be created by adding an optoelectronic loop to the laser of Chapter 3, an optical frequency stabilized COEO can be created by adding an optoelectronic loop to the frequency stabilized laser of Chapter 5. As in Figure 6.1, the optoelectronic loop is formed by photodetecting part of the laser output with a high speed detector, amplifying, and driving the modulator in the laser cavity. A phase shifter is also included to ensure the modulator is at peak transmission when a pulse travels through and can be used for fine control of the pulse repetition rate. Note that unlike conventional the COEO, an RF mode selection filter is no longer necessary in the optoelectronic loop, for this function is now performed by the etalon. Figure 6.2 illustrates a frequency domain picture of the difference between an intracavity etalon-based COEO and a conventional COEO with an RF filter. Without the inclusion of an etalon, the laser supports modes separated by the laser cavity fundamental frequency, $f_0$ (around 35.5 MHz for the

oscillator described below). In the conventional COEO of Figure 6.1, an RF filter in the optoelectronic loop determines the pulse repetition rate by selecting a harmonic of $f_0$ to drive the modulator. In this case the optical spectrum behaves like that of an actively harmonically mode-locked laser where interleaved mode sets, or supermodes, operate simultaneously. Just like the time domain lasers of Chapter 3, simultaneous lasing of different optical supermodes precludes the use of a single phase locked frequency comb with multi-gigahertz spacing. Placing an etalon in the laser cavity eliminates all but one optical supermode. The selection of a single optical supermode also eliminates spurious beat frequencies in the optoelectronic loop, rendering any RF filtering unnecessary. Another unique feature of the etalon-based COEO is that it is a completely self-contained optical frequency stabilized source. Instead of using a separate oscillator to provide the reference for the Pound-Drever-Hall error signal, the 10.24 GHz COEO signal is frequency divided down to 640 MHz for this purpose. In this way, the optical frequencies and their stability and the RF frequency of the oscillator are all solely defined by the intracavity etalon.

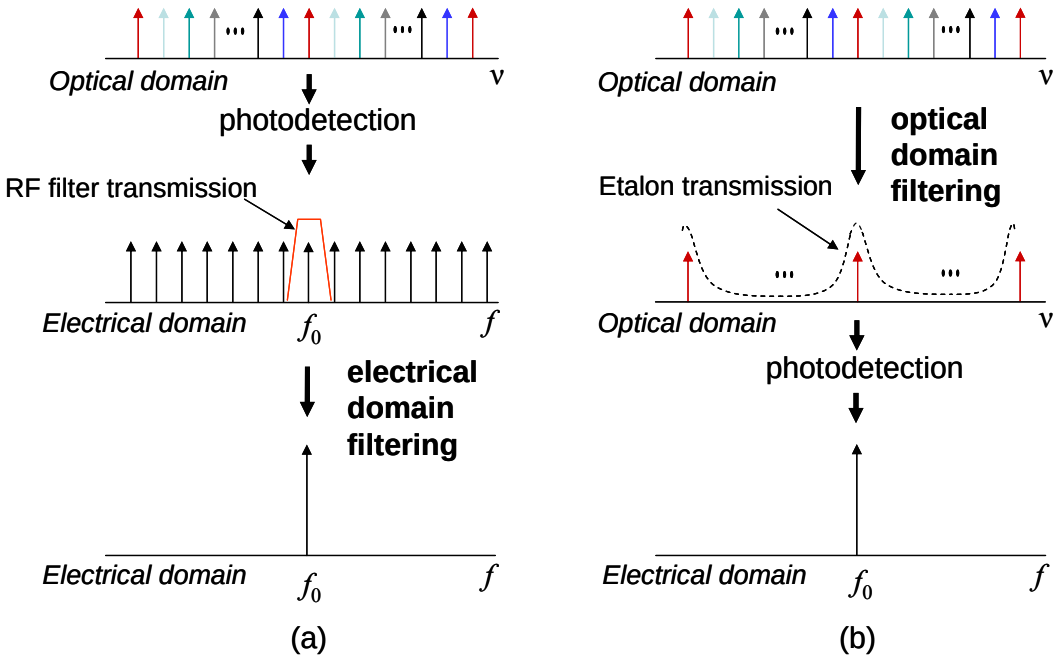


Figure 6.2: Comparison of the frequency domain pictures of (a) a conventional COEO and (b) an intracavity etalon-based COEO.

### *6.3 Optical frequency self stabilized COEO*

The intracavity etalon-based COEO with optical frequency stabilization is shown in Figure 6.3. Note that as described above, neither an RF filter in the optoelectronic loop nor a separate oscillator for the PDH loop are included. The optical spectrum of the COEO is shown in Figure 6.4. The full spectrum with a -10 dB width of 13 nm is shown in Figure 6.4(a) while the high OSNR is of a single mode is shown in Figure 6.4(b). When comparing Figure 6.4 to Figure 5.6, it can be seen that the quality of the optical spectrum has been maintained when the actively mode-locked laser was converted to a COEO. Furthermore, optical frequency stability was measured using the same technique as described in Chapter 5 for the actively mode-locked laser. The result is shown in

Figure 6.5. The linewidth and optical frequency stability are also maintained, demonstrating the ability of the COEO to self-stabilize the 10.24 GHz-spaced optical frequency comb.

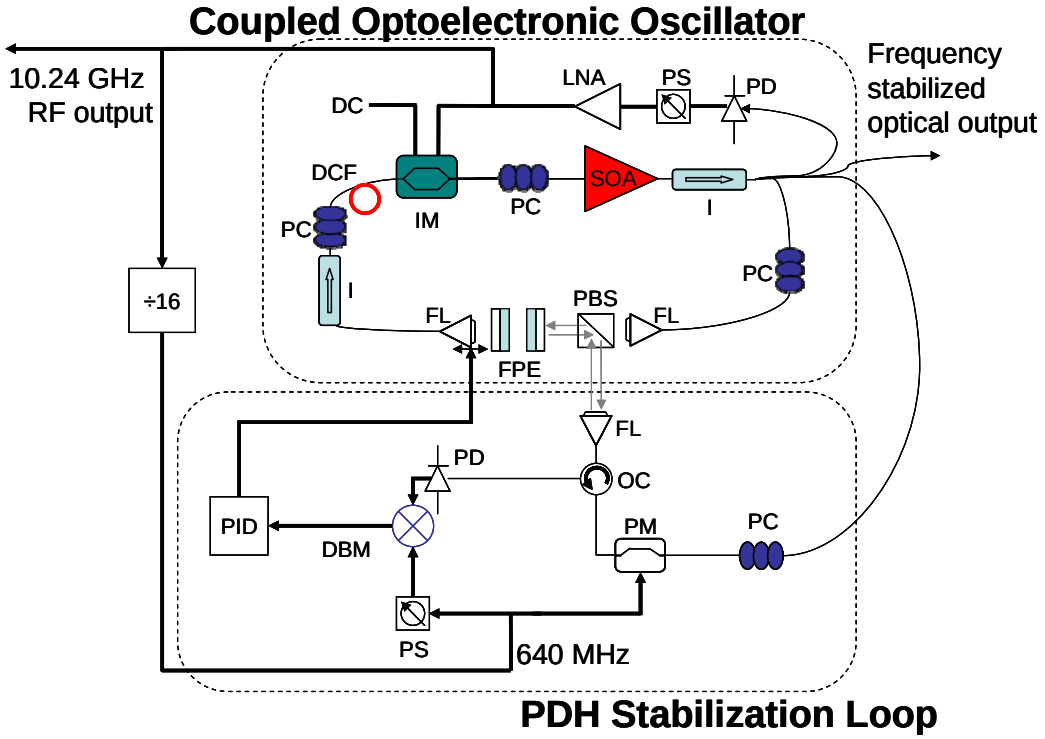


Figure 6.3: Optical frequency stabilized coupled optoelectronic oscillator schematic. The PDH loop is driven by the frequency divided COEO signal. LNA, low noise amplifier.

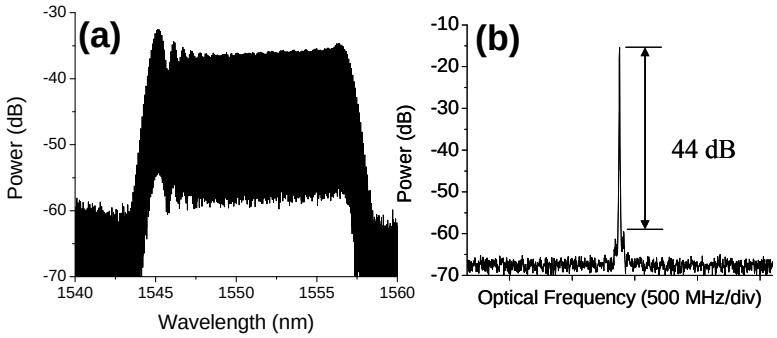


Figure 6.4: Optical frequency stabilized COEO optical spectrum. (a) Full spectrum with a 13 nm -10 dB width, (b) high resolution optical spectrum of a single mode demonstrating 44 dB sidemode suppression.

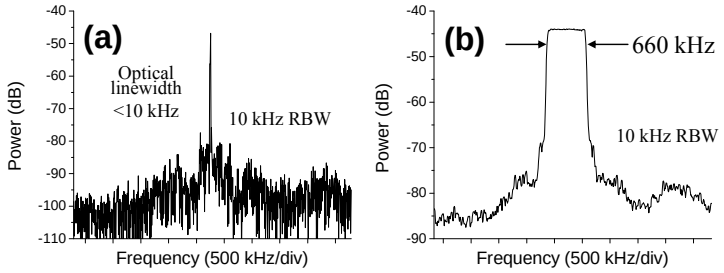


Figure 6.5: Optical frequency stabilized COEO. (a) Linewidth and (b) frequency stability measurements in the RF domain.

The removal of the RF filter can be advantageous, for the RF filter can be very susceptible to environmental fluctuations. The change in the delay due to environmental changes for a 10.24 GHz signal through a bandpass filter was measured using the setup shown in Figure 6.6(a). The tested filter had a -10 dB bandwidth of 27 MHz centered at 10.24 GHz. A low noise 10.24 GHz signal was split with half the power going through the filter to the RF port of a double balance mixer and half the power going through a

phase shifter to the LO port of the mixer. The two signals on the mixer were set to phase quadrature by the phase shifter to create a phase to voltage converter. By monitoring the DC voltage level after the mixer, the relative phase shift between the two inputs to the mixer was measured. The results are shown in Figure 6.6(b). Also shown is the result of the same measurement when the filter is replaced by a short length of cable. When the RF filter is placed in the electrical feedback loop of a COEO, these changes in the accumulated phase translate into frequency fluctuations of the COEO signal. The direct effect of the RF bandpass filter stability on the COEO frequency stability is shown in Figure 6.7. When the bandpass filter is placed in the electrical feedback loop (directly after the low noise amplifier), the maximum frequency deviation of the COEO signal is more than an order of magnitude greater than when there is no filter in the feedback loop. The maximum frequency deviation of the COEO signal when the RF filter is removed corresponds to 0.06 ppm.

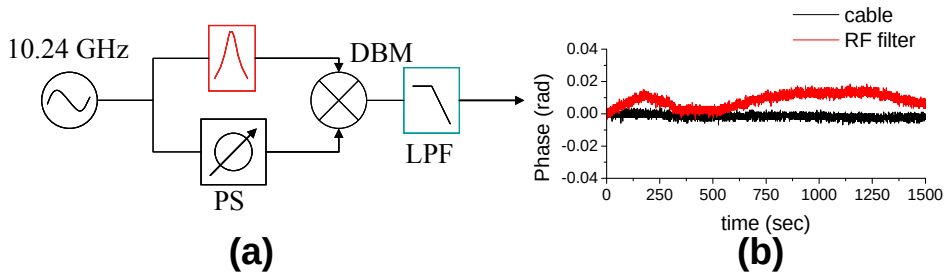


Figure 6.6: Phase to voltage converter. (a) Setup and (b) result showing the susceptibility of the RF filter to environmental influences.

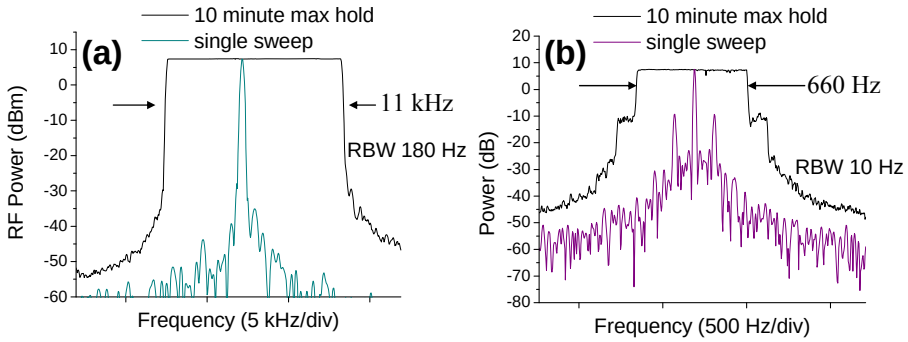


Figure 6.7: Stability of the 10.24 GHz output of the COEO (a) when an RF filter for mode selection is included in the electrical feedback loop and (b) when the RF filter is removed. Note the different scales on the horizontal axes.

Additional RF spectra were measured to determine the purity of the COEO signal and the suppression of the supermode noise spurs. The level of suppression of the supermode noise spurs of the RF output of the COEO is shown in Figure 6.8(a). The spurs are barely visible above the noise floor, corresponding to noise level better than -130 dBc/Hz. This level of supermode suppression is the same as the directly measured photodetected spectrum of the actively mode-locked laser from Chapter 5. A 5 kHz span measurement of this signal, shown in Figure 6.8(b), shows the well defined COEO frequency for this oscillator.

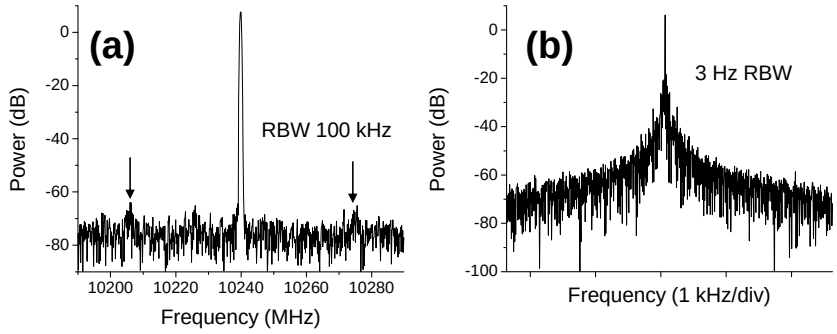


Figure 6.8: RF spectra of the COEO output. (a) 100 MHz span measurement; the arrows indicate the location of the supermode noise spurs. (b) 5 kHz span measurement showing a well defined COEO frequency.

Finally, the pulse autocorrelation was measured for the COEO. Again, the output pulse has a large linear chirp and can be compressed to under 1 ps as shown in Figure 6.9.

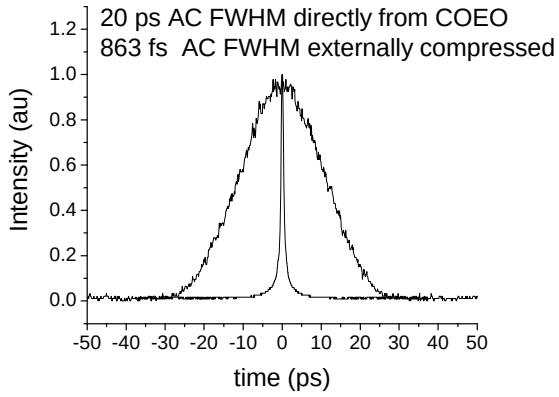


Figure 6.9: Pulse autocorrelation for the optical frequency stabilized COEO.

### *6.4 Optical frequency and repetition rate stabilization in a COEO*

The COEO design of the previous section, while generating a stabilized comb, can be improved upon and still remain self contained if the optical bandwidth is sufficiently broad. A shortcoming of the COEO of the previous section is that by changing the laser cavity length to stabilize the optical frequencies, the repetition rate may change. That is to say, one error signal cannot simultaneously stabilize the average optical frequency and the mode separation. However, by taking the difference between two error signals derived from opposite ends of the optical spectrum, a signal that is proportional to only the repetition rate can be obtained. To see how this is so, recall that the PDH error signal voltage $V$ is proportional to the deviation of the laser mode from the transmission peak of the etalon:

$$V \propto \delta\nu_n = \delta\nu_c + n\delta f_{rep} \tag{6.2}$$

where $\delta\nu_n$ is change in the optical frequency of the $n$th mode, $\delta\nu_c$ is the change in the average frequency, or laser carrier frequency and $\delta f_{rep}$ is the change in the pulse repetition rate. If another error signal is generated from the $m$th mode, the difference between the error signals is

$$V_1 - V_2 \propto \delta\nu_n - \delta\nu_m = (n-m)\delta f_{rep} \tag{6.3}$$

Thus the difference in error signals is independent of changes to the optical carrier frequency and can be used to independently control the pulse repetition rate. The scheme used here is similar to [48] where an external etalon was used to stabilize the comb of a passively mode-locked Ti:sapphire laser.

A schematic for an optical frequency stabilized COEO incorporating two PDH error signals for repetition rate stabilization is shown in Figure 6.10. This setup differs from that of Figure 6.3 in that after the phase modulated signal is reflected from the etalon, it is split and sent to two separate 0.8 nm width tunable bandpass filters centered at opposite ends of the optical spectrum. Separate PDH error signals are generated from the filtered comb sections and their difference is applied to a voltage controlled phase shifter in the optoelectronic loop to stabilize the repetition rate. One of the individual error signals is then used to control the cavity length to stabilize the optical frequencies.

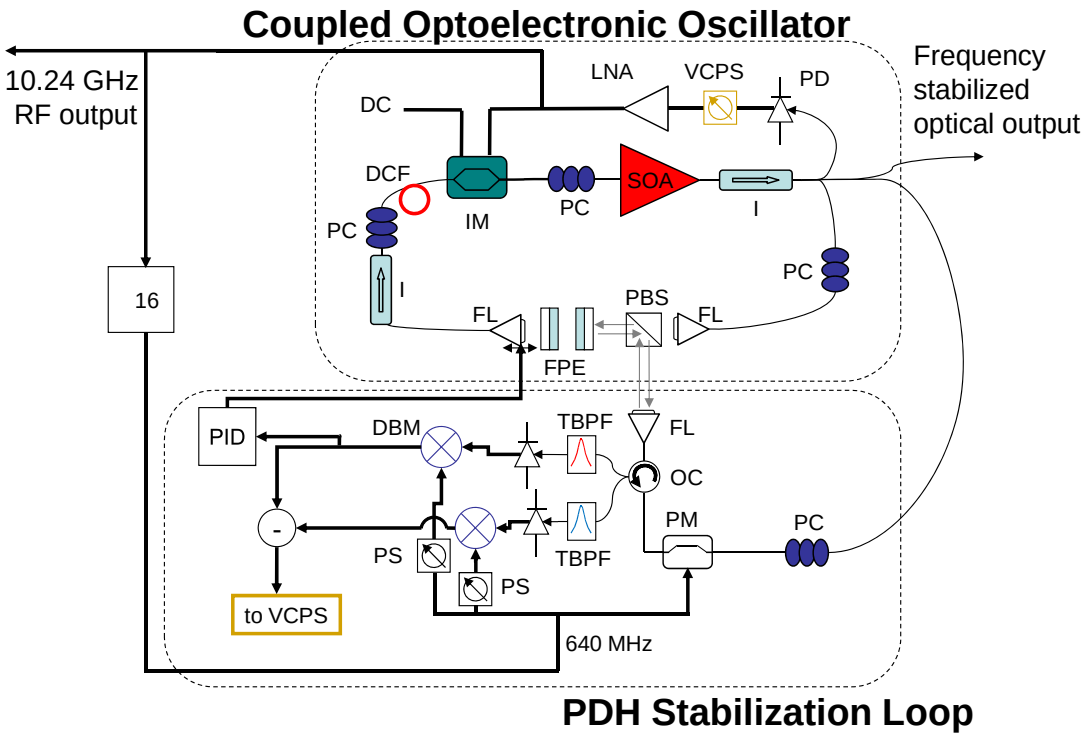


Figure 6.10: Coupled optoelectronic oscillator with optical frequency and pulse repetition rate stabilization. VCPS, voltage controlled phase shifter; TBPF, tunable bandpass filter.

In order to improve on the COEO with only one PDH error signal, the dual PDH approach must be able to detect pulse repetition rate changes smaller than 660 Hz. With the given etalon and optical spectral bandwidth, it is not immediately obvious that this is the case. To test the viability of the dual PDH approach, the COEO of Figure 6.10 was converted into an actively mode-locked laser by replacing the optoelectronic loop with an RF synthesizer. Active mode-locking allowed for precise control of the pulse repetition rate while the difference between error signals was monitored. (Care was taken to balance the strength of the error signals to keep changes in the average frequency from contributing to their difference.) The results of this measurement are shown in Figure 6.11. Figure 6.11(a) shows the step-wise sweep of the pulse repetition rate, and Figure 6.11(b) shows the resulting change in the difference between error signals generated from spectral components 15.4 nm apart. Note that the 56 Hz steps in the repetition rate are resolved in the error signal measurement, indicating the possibility of improvement over the single PDH design. Instabilities in the etalon, however, may limit the stability of the repetition rate to level worse than implied by the results of Figure 6.11. Stability limits are discussed in greater detail in the following section.

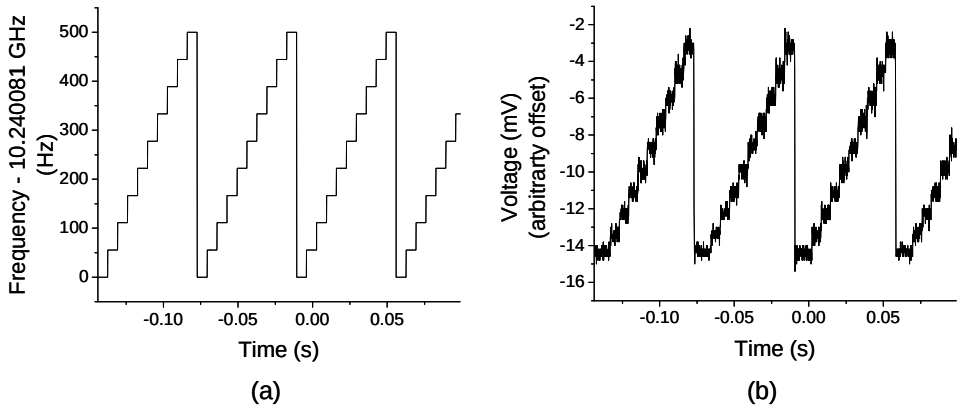


Figure 6.11: Repetition rate sensitivity measurement. (a) Illustration of the step-wise frequency sweep of the repetition rate. (b) Measured difference in the error signals generated from spectral components 15.4 nm apart where the 56 Hz steps in the repetition rate are observed.

The optical spectrum of the COEO with both optical frequency and pulse repetition rate stabilization is shown in Figure 6.12. Careful optimization of the RF power sent to the Mach-Zehnder modulator expanded the -10 dB bandwidth slightly to 15.5 nm, corresponding to 190 comb lines or nearly 1.96 THz. Also shown in Figure 6.12 is the filtered comb sections used in the stabilization feedback loops.

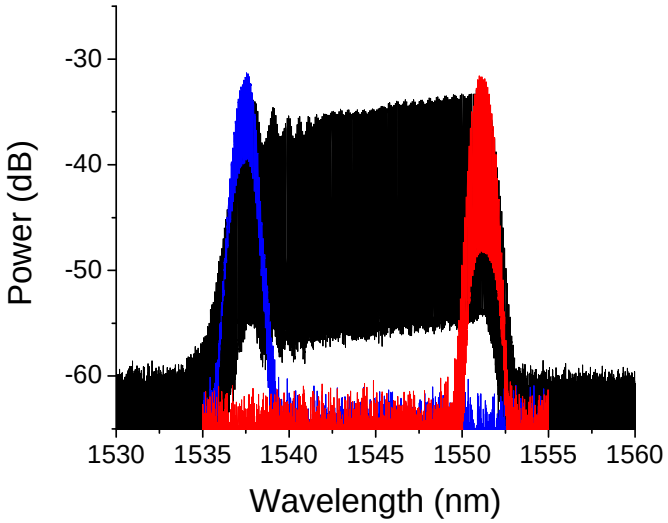


Figure 6.12: Optical spectrum of the optical frequency and repetition rate stabilized COEO with 190 comb lines in a -10 dB width. The filtered sections of the spectrum used in the stabilization loops are also shown.

Figure 6.13 shows the stability of the repetition rate when the repetition rate stabilization is applied. The maximum drift over 10 minutes of 350 Hz is nearly a factor of two better than when only a single PDH loop is used to stabilize the COEO.

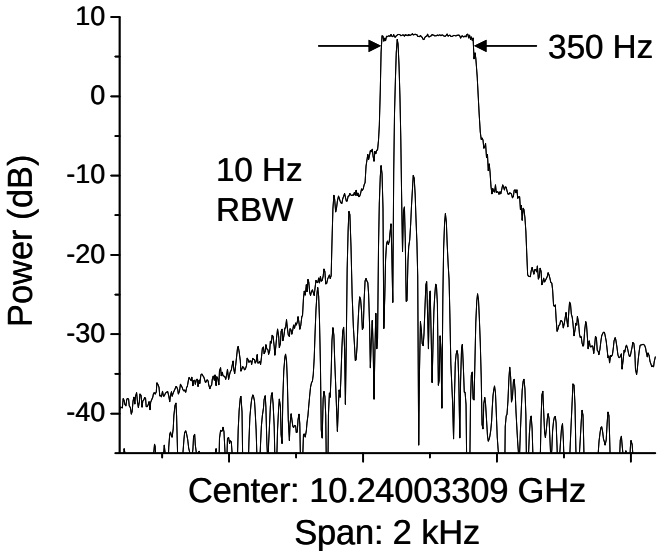


Figure 6.13: Repetition rate stability measurement of the COEO with optical frequency and pulse repetition rate stabilization. The maximum deviation of the repetition rate in 10 minutes is 350 Hz. Side spurs are 60 Hz line noise and harmonics.

The optical and repetition rate stabilized coupled optoelectronic oscillator presented in this section represents a unique oscillator, capable of generating low jitter optical pulses, a low noise RF signal at 10 GHz and narrow linewidth optical modes in a completely self-contained manner. This suite of characteristics is not available in any other source, leading to the belief that this laser can have a broad impact on a number of high performance signal processing and coherent communication applications.

## *6.6 Comb dynamics of an etalon based COEO*

### 6.6.1 Introduction and description of the fixed point formalism

Any comb line may be represented as a function of two parameters: the repetition rate $f_{rep}$ and either a carrier envelope offset frequency $f_{ceo}$ (near DC) or an optical carrier frequency $\nu_c$ (near the center of the optical spectrum). For passively mode-locked lasers with supercontinuum generation, where an electrical reference signal is used to stabilize the frequency comb, it is more appropriate to write the comb line frequencies in terms of $f_{ceo}$ rather than $\nu_c$. When the comb is stabilized to an optical reference, $\nu_c$ is the parameter of choice. Since the reference for the COEO described above is the intracavity etalon, the comb lines are represented as $\nu_n = \nu_c + nf_{rep}$ . When the COEO is perturbed, the frequency of the $n$th comb line is changed due to changes in both $\nu_c$ and $f_{rep}$. Two questions then arise: to what extent are $\nu_c$ and $f_{rep}$ changed for a given perturbation and what system parameters are best utilized to stabilize $\nu_c$ and $f_{rep}$? The oscillator of Figure 6.10 uses the phase in the optoelectronic loop and the cavity length to control the optical frequencies and the repetition rate, respectively. The arrangement of these feedback loops seems reasonable, since the optical frequencies of the actively mode-locked laser were also stabilized with feedback to the cavity length and since the optoelectronic loop replaces the RF source that controlled the repetition rate. For an actively mode-locked laser, it is clear that changing the cavity length only changes the optical carrier frequency, and tuning the RF source frequency only changes the pulse repetition rate. The optical frequency stabilized COEO is of course not an actively mode-locked laser, so one should not assume the orthogonality of the feedback loops still holds. That is to say that in general, changes to any parameter (such as the cavity length) will affect both $\nu_c$ and $f_{rep}$.

This is also true for passively mode-locked lasers, and a "fixed point formalism" has been developed to describe how changing a given parameter will affect $v_c$ and $f_{rep}$ [49], [50]. The fixed point description is as follows. When a laser parameter is changed, the frequency of the nth comb line changes as

$$\delta\nu_n = \delta\nu_c + n\delta f_{rep} \tag{6.4}$$

For the comb line indexed by $n_{fix} = -\frac{\delta\nu_c}{\delta f_{rep}}$, the change in the carrier frequency is compensated for the change in $f_{rep}$ leaving the mode frequency unchanged. This frequency (which need not lie within the optical bandwidth of the comb) is called the fixed frequency or fixed point for the given parameter, and different parameters will have different fixed points. Note that the comb "breathes" about the fixed point as the given parameter changes, and the frequency of the *n*th comb line can now be indexed (with index *m*) from the $v_{fix}$ as

$$\nu_m = \nu_{fix} + mf_{rep}. \tag{6.5}$$

The change in a comb line frequency from a change in the given parameter is now

$$\delta\nu_m = m\delta f_{rep}. \tag{6.6}$$

The location of the fixed point determines how this parameter should be leveraged for comb control, as illustrated in Figure 6.14. Here two fixed point locations are shown. For the fixed point frequency far below the optical spectrum, small changes in $f_{rep}$ are accompanied by large changes in $v_c$. The parameter with this fixed point is best for controlling $v_c$. For the fixed point near the center of the optical spectrum, $v_c$ changes very

little if at all when the parameter changes; it is mainly $f_{rep}$ that is affected, and the parameter with this fixed point is best for controlling $f_{rep}$.

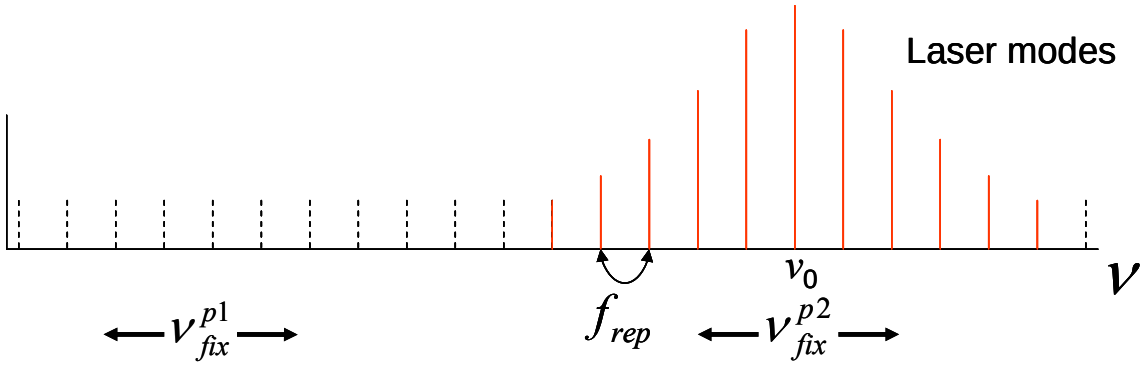


Figure 6.14: Illustration of two fixed point frequencies. When parameter 1 is changed, the comb "breathes" about $\nu_{fix}^{p1}$, when parameter 2 changes, the comb "breathes" about $\nu_{fix}^{p2}$.

### 6.6.2 Measuring the fixed points

Although fixed points have been theoretically derived for passively mode-locked lasers [51], the fixed points for the COEO are determined experimentally. The setup showing the measurement of the fixed point for the phase in the optoelectronic loop is shown in Figure 6.15. The locations of the fixed points can be determined by measuring the ratio of the change in the optical frequency of a laser mode to the change in the pulse repetition rate as one of the laser parameters is modulated. The location of the fixed point $\nu_{fix}$ is then calculated as

$$\nu_{fix} = \nu_n - \left( \frac{\delta \nu_n}{\delta f_{rep}} \right) \cdot f_{rep}. \tag{6.7}$$

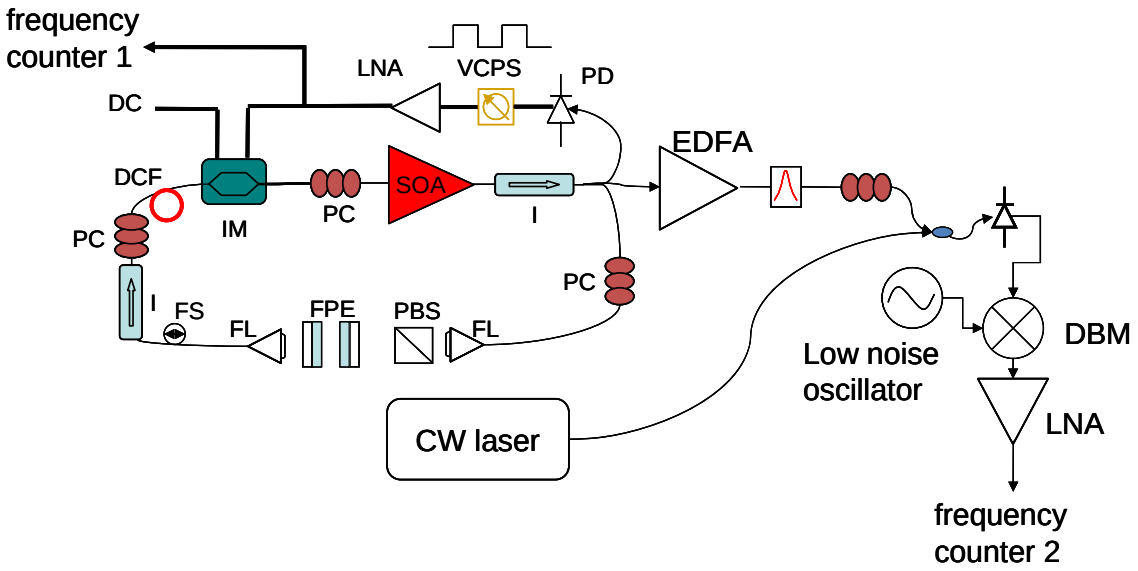


Figure 6.15: Setup for the measurements of the fixed point frequencies of an etalon-based COEO. Parameters of phase of the optoelectronic loop, SOA bias current, modulator DC bias and laser cavity length in fiber and free space were tested. Each parameter was square wave modulated and the changes to the frequency of the *n*th mode and the repetition rate was monitored with frequency counters. A low noise oscillator was used to mix down the optical frequency beat tone to within the bandwidth of the 2nd frequency counter.

By square-wave modulating the COEO parameters at 0.4 Hz, the locations of the fixed points were measured for the COEO of Figure 6.15. Changes to the 10.24 GHz repetition rate were measured with a frequency counter set to 10 Hz resolution. Changes to the

optical frequency were measured by beating a laser mode with a stable, narrow linewidth continuous-wave (CW) laser. The stability of the beat tone was monitored with a second frequency counter with 0.1 second gate time. Ambiguity in the sign of $\delta\nu_n$ was resolved with a high resolution measurement of the optical spectrum of the COEO and the CW laser, shown in Figure 6.16(a). Here it is seen the COEO comb line lies at a lower frequency than the CW laser. Thus an increase in the frequency of the beat tone indicates a decrease in the frequency of the comb line. The full optical spectrum of the COEO is shown in Figure 6.16(b).

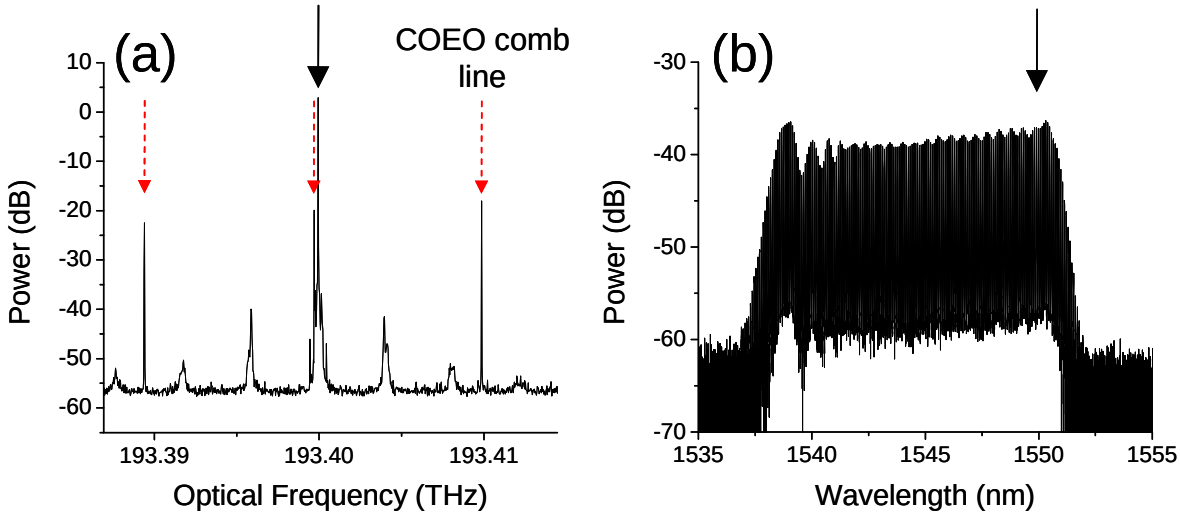


Figure 6.16: Optical spectra. (a) High resolution spectrum. The red dotted arrows indicate COEO comb lines, the black arrow indicates the CW laser line. Other spurs are artifacts of the high resolution spectrum analyzer. (b) Full spectrum of the COEO. The arrow indicates the location of the CW laser.

First, the comb dynamics for changes to the OE loop phase were measured by applying a 2.6 mrad peak-to-peak modulation via a voltage controlled phase shifter. The

optoelectronic loop is a feature not present in passively mode-locked lasers, so it is worth mentioning how changes to the OE loop phase affect the pulse repetition rate and the associated fixed point frequency. The affect of the OE loop phase is best illustrated by reducing the COEO to a simple resonator-with-feedback oscillator. By requiring that the phase accumulated in the OE loop be a multiple of 2π, the change in $f_{rep}$ for a change in OE phase can be shown to be [52]

$$\delta f_{rep} = \delta\varphi \frac{f_{rep}}{2Q_R} \tag{6.8}$$

where $\delta\varphi$ is the change in the optoelectronic loop phase and $Q_R$ is the effective microwave quality factor of the laser resonator. Since changes to the optoelectronic loop phase do not affect the phase of the optical carrier, the fixed point is expected to be close to the center of the COEO optical spectrum. The measured changes to the optical frequency and the repetition rate are shown in Figures 6.17(a) and (b), respectively. The ratio $\delta\nu/\delta f_{rep}$ calculated from Figure 6.17 places the fixed point at 194.7 THz, which is indeed close to the center of the COEO spectrum. Also, note that this measurement allows for the determination of the effective microwave quality factor of the laser cavity through Equation 6.8. The calculated QR is $10^4$, which is inline with the Q value reported in Chapter 3. (Since the laser cavity is much shorter here than in Chapter 3, a smaller Q value is expected.)

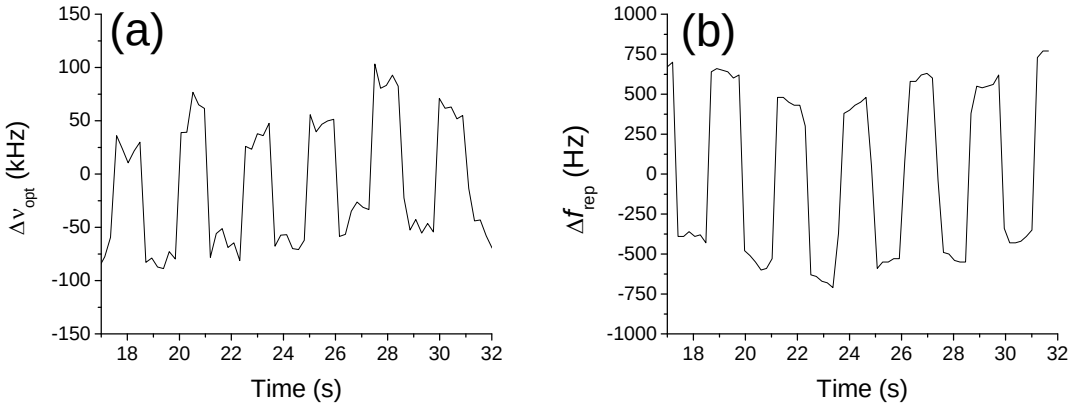


Figure 6.17: Optoelectronic loop phase fixed point measurement. (a) Changes in the optical frequency as the phase is square-wave modulated. Noise is mainly due to instabilities in the CW laser. (b) Changes in the repetition rate as the phase is square-wave modulated.

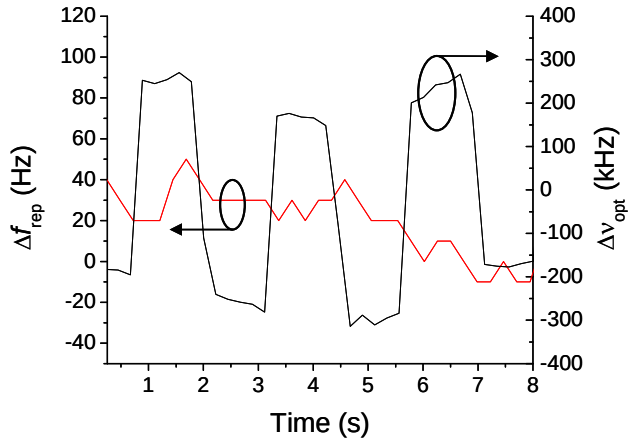


Figure 6.18: Cavity length change in fiber fixed point measurement, showing changes in the repetition rate and changes in the optical frequency as the voltage to a fiber stretcher is square-wave modulated. An upper bound on the repetition rate change of 30 Hz puts an upper bound on the fixed point of 36 THz.

The results of the modulation of the cavity length via a fiber stretcher are shown in Figure 6.18. Instabilities in the measurements of $f_{rep}$ prevent exact calculation of the fixed point, however, a change in $\delta f_{rep}$ of ~30 Hz puts a conservative upper bound on the fixed point frequency of ~36 THz. While this estimated fixed point frequency is higher than expected, it should be noted that with the large value of $\delta\nu/\delta f_{rep}$ , the fixed point frequency is very sensitive to the value of $\delta f_{rep}$. If a 25 Hz rep rate change is assumed, the fixed point drops to 5 THz. The depth of modulation of the cavity length could not be increased to make changes to $f_{rep}$ more apparent, for this pushed the optical modes too far from the etalon resonances and destabilized mode-locking. Also note that in general, the presence of the OE loop will effect the amount the repetition rate changes due to changes in the pulse round trip time in the laser cavity. Again, by requiring the accumulated phase in the OE loop to a multiple of 2π it can be shown that

$$\delta f_{rep} = \frac{\delta f_0}{1+\frac{Q_{OE}}{Q_R}} \tag{6.9}$$

where $f_0$ is the natural resonance of the high quality factor resonator (in this case the inverse of the pulse round trip time in the laser cavity) and $Q_{OE}$ is the microwave quality factor of the OE loop, given by $2\pi f_{rep}\tau$. For most COEOs, including the one reported here, $Q_R >> Q_{OE}$ and the effect of the delay in the OE loop is small.

The fixed points for the SOA current, DC bias on the modulator, and free space cavity length changes were also measured. The results of all the fixed point measurements are summarized in Figure 6.19. The fixed point frequency for the bias voltage to the intensity modulator, varied at 1% of the full depth of modulation applied, was measured to be 196.1 THz. Small changes to the modulator bias are essentially changes to the intracavity

loss, and considering results from passively mode-locked lasers [50], the fixed point is expected to be close to the optical carrier frequency. The location of the fixed point for cavity length changes in free space, otherwise expected to be close to 0 Hz, is shifted to the much higher frequency of 183.8 THz. However, it was noticed that as the free space cavity length changed, the power in the repetition rate signal also changed. This observation led to the conclusion that the free-space-to-fiber coupling changed with the movement of the fiber launcher position, and the changes to the intracavity loss shifted the fixed point frequency. The SOA current, modulated at a 2% modulation depth, was determined to have a fixed point also at 183.8 THz, well within the expected range [50].

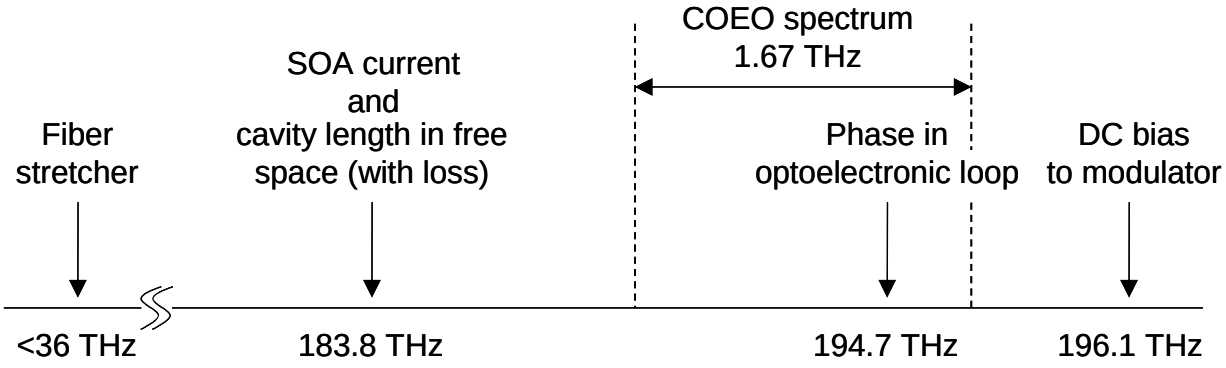


Figure 6.19: Summary of fixed point measurements. The COEO spectrum, centered at 194.1 THz, is included for reference.

With a fixed point frequency far from the optical carrier, changes to the fiber cavity length yield the largest change in the optical frequency for a given change in the repetition rate. This indicates that feedback to an intracavity fiber stretcher is best for control of the optical carrier frequency. Similarly, the OE loop yields the smallest change to the optical frequencies for a given change in the repetition rate, and is therefore ideal

for feedback control of $f_{rep}$. For the system in Figure 6.10, the error signal used for feedback to the cavity length is influenced by changes to the OE loop phase. The method by which this undesirable coupling can be eliminated follows from the measurements of the fixed point frequencies. The OE loop fixed point frequency is by definition insensitive to changes in the OE loop phase. By using this frequency for generating the cavity length control error signal, the laser cavity length can be decoupled from the OE loop phase. However, the maximum sensitivity for measuring changes to the pulse repetition rate is achieved by comparing error signals from comb lines at opposite ends of the COEO spectrum. Implementing this decoupling therefore comes at the cost of either decreased sensitivity to changes in the repetition rate or the added complexity of generating a third PDH error signal.

In summary, the fixed point frequencies for an etalon-based coupled optoelectronic oscillator have been measured. It was found that out of the possible feedback paths for stabilization, the optoelectronic phase, with a fixed point of 194.7 THz, and laser cavity length changes in fiber, with a fixed point below 36 THz, are best for control of the pulse repetition rate and optical carrier frequency, respectively. Moreover, determination of the fixed point frequencies has lead to a feedback architecture for improved comb control of a COEO where feedback to the cavity length is decoupled from changes to the phase in the optoelectronic loop.

# CHAPTER 7
# FUTURE WORK

The optical frequency self stabilized COEO results to date demonstrate the promise of this design to generate not only a low noise, stable 10 GHz signal, but also to generate a highly stable optical frequency comb. Two areas of improvement have been identified, namely the incorporation of a higher finesse, more stable etalon and active phase noise reduction. The implementation of these two areas constitutes the future work on the self-stabilized COEO.

## *7.1 Incorporation of a more stable, higher finesse etalon*

With the intracavity etalon responsible for the multiple tasks of supermode suppression, stabilization of the optical frequencies, and defining and stabilizing the pulse repetition rate, the performance of the COEO depends heavily on the performance of the etalon. Although the etalon used in these experiments has three low expansion coefficient spacers, it is unsealed, leaving the refractive index of the air gap susceptible to air currents, and changes in air temperature and pressure. To demonstrate the sensitivity of the laser to air pressure changes, a pressure differential between our lab and the outside hallway was exploited. (The lab is kept at a slightly higher pressure in an attempt to keep out dust.) With the laser actively mode-locked, a beat tone between the mode-locked laser and the stable CW source was measured as the lab door was opened and closed and the PDH stabilization run in either open or closed loop. The results are shown in Figure 7.1. Figure 7.1(a) shows the frequency of the beat tone with the lab door closed. For short durations, the laser will operate with the PDH in open loop (that is, feedback is not

applied to the cavity length), and Figure 7.1(a) represents the beat signal when the door is closed for either open or closed loop PDH. Figure 7.1(b) is the beat signal when the door is opened with the open loop PDH, and a 1 MHz shift in the beat tone is observed. This is contrasted with the beat tone measurement in Figure 7.1(c) where the door is open and the PDH loop is closed. In this case the laser line tracks the frequency change of the etalon transmission peak, and the shift in the frequency of the beat tone is now 4 MHz. It should be noted that when the PDH loop is closed, the beat frequency shift is stable while the door remains open. A shift of 4 MHz of an etalon transmission peak at 1550 nm corresponds to a fractional index change of the air gap of only $2 \cdot 10^{-8}$, which in turn corresponds to a fractional air pressure change of only $\sim 2 \cdot 10^{-5}$ [53]. Of course, the free spectral range of the etalon is also affected. Assuming the same shift in the transmission peak of 4 MHz, the free spectral range of the etalon will shift ~200 Hz. This is close to the measured stability of the COEO repetition rate in Figure 6.13.

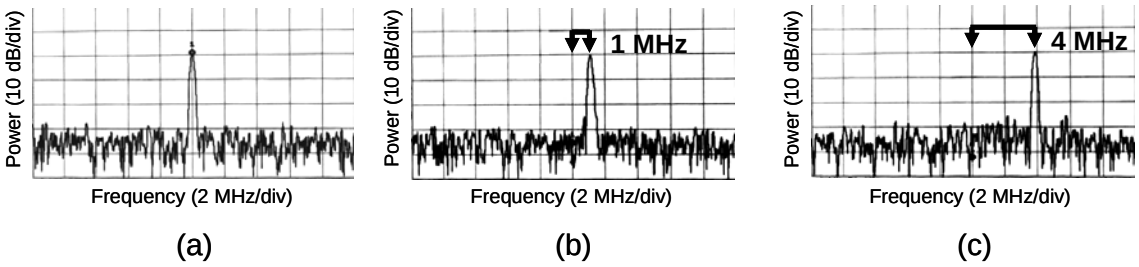


Figure 7.1: Measurement of the etalon stability. (a) Mode-locked laser – CW laser beat frequency when the lab door is closed and the PDH is in either the open loop or closed loop state. (b) Beat frequency when the lab door is open and the PDH is in open loop state. (c) Beat frequency when the lab door is open and the PDH is in the closed loop state.

Since we are at the limit of stability provided by the etalon, further progress in an etalon-based COEO must be made with a more stable etalon. It is believed that incorporating a sealed etalon will improve performance. Moreover, the greater stability provided with a sealed etalon allows for simultaneous increase in the etalon finesse. Increasing the etalon finesse has many potential advantages. First, it will allow for a longer laser cavity length while still only supporting a single optical supermode. This will not only reduce the optical linewidth, but it will improve the effective microwave quality factor as well. Second, it will provide a sharper discriminant for Pound-Drever-Hall stabilization, for the ratio of the error signal voltage to the frequency change is inversely proportional to the width of the etalon transmission peak. Having a sharper discriminant will improve the sensitivity of fluctuations of both the average optical frequency and the pulse repetition rate.

### *7.2 Active suppression of the RF phase noise in a COEO*

The phase noise of the RF signal depends heavily on the resonator bandwidth, or equivalently the resonator quality factor. Figure 7.2 shows how the phase noise of an oscillator decreases as the Q of the resonator increases. In a COEO, a high Q is acquired by creating a long storage time in the laser cavity with a long round trip time. The dependence of the microwave Q on the laser cavity length implies that a long laser cavity can produce very low noise COEOs. Indeed, the lowest (close to the carrier) phase noise COEOs have optical cavity lengths hundreds of meters long [54]. Such long cavity lengths are not practical in an optical frequency stabilized COEO, however. The limited finesse of the intracavity etalon requires the longitudinal modes of the laser cavity to have enough separation so that the etalon can select a single supermode set. The etalon used in

the experiments described above has a finesse of ~100; this limited the laser cavity length to below ~10 meters. Another potential solution to reduce the noise of an optical frequency stabilized COEO is active noise suppression.

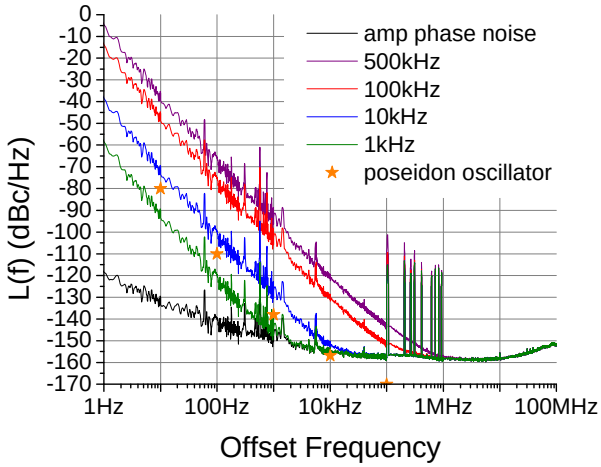


Figure 7.2: The phase noise of an oscillator for different resonator bandwidths when the internal phase noise is dominated by the amplifier phase noise. The Poseidon oscillator phase noise is shown for comparison.

Actively suppressing the phase noise of a COEO requires measurement of the phase fluctuations in the optoelectronic loop and feedback to compensate for those fluctuations. Note that such systems have been demonstrated for purely microwave oscillators [55], [56]. To see how this can be accomplished, recall the phase noise measurement techniques expounded upon in Chapter 2. From Section 2.2.2 the phase noise of relative noise measurement system is given by

$$S_m(\omega) = S^{\phi}(\omega) \cdot \left[1 + |H(\omega)|^2 - 2|H(\omega)|\cos(\theta(\omega))\right]. \tag{7.1}$$

For a system with $|H(\omega)| \approx 1$ and $\theta(\omega) \approx \omega / \omega_1$, in other words the transfer function is governed by a phase response that is proportional to the frequency, the power spectral density of the output of the system reduces to

$$S_m(\omega) = \frac{\omega^2}{\omega_1^2} S^{\phi}(\omega) \tag{7.2}$$

Examples of such systems include the delay line frequency discriminator and a mode-locked laser. Thus such systems give the phase noise of the input multiplied by the square of the offset frequency. It turns out (see Appendix B) that power spectrum of the phase fluctuations of the optoelectronic loop $S^{\psi}(\omega)$ of a COEO has an inverse relationship to the power spectrum of the phase noise of the oscillator output $S^{\phi}(\omega)$, namely,

$$S^{\phi}(\omega) = \left(\frac{\Gamma^2}{\omega^2}\right) S^{\psi}(\omega). \tag{7.3}$$

Putting Equation 7.2 together with Equation 7.3 yields

$$S_m(\omega) = \frac{\Gamma^2}{\omega_1^2} S^{\psi}(\omega) \tag{7.4}$$

and the noise $S^{\psi}(\omega)$is recovered. In other words, the action of the coupled optoelectronic oscillator is to turn phase fluctuations into frequency fluctuations while the frequency discriminator converts frequency fluctuations into phase fluctuations to recover the phase noise $S^{\psi}(\omega)$. This phase information can be used to adjust the phase in the COEO optoelectronic loop. The noise of the oscillator is then limited to the noise floor of the phase noise correction feedback loop.

In order to lower the phase noise of a COEO then, a frequency discriminator can be used. The discriminator does not need to be separate from the oscillator itself [56]. Either by using the mode-locked laser or by incorporating a delay line into the COEO, the oscillator's high Q element can double as the frequency discriminator for phase noise reduction. (Note the similarity with using the same intracavity etalon for supermode suppression and optical frequency stabilization in Chapter 5.) A potential design that utilizes the mode-locked laser is shown in Figure 7.3. The oscillator signals before and after the mode-locked laser (and photodetector) are compared and the phase difference is applied to a phase shifter in the loop. The difficulty with this scheme is that the laser is an active device, and the phase difference before and after the mode-locked laser will contain the laser's residual noise as well as the discriminator signal. The residual noise will set the noise floor of the phase correction feedback loop and thus the oscillator noise as well. For the setup in Figure 7.3, the oscillator noise for different levels of laser residual noise can be calculated, and are plotted in Figure 7.4. Note that a Q value of $6 \cdot 10^4$ is assumed in Figure 7.4. These noise levels are higher than desired. If a higher finesse etalon is used in the laser cavity allowing for a longer laser cavity and therefore higher effective microwave Q, the efficacy of the design of Figure 7.3 should be reassessed, as the higher Q greatly reduces the noise levels.

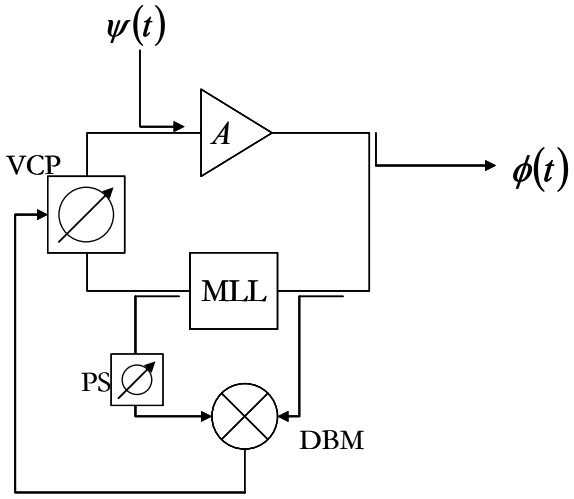


Figure 7.3: Proposed setup for active phase noise reduction by using the discriminator effects of a mode-locked laser. A, RF amplifier; VCP, voltage controlled phase shifter; DBM double balanced mixer; PS phase shifter; MLL, mode-locked laser.

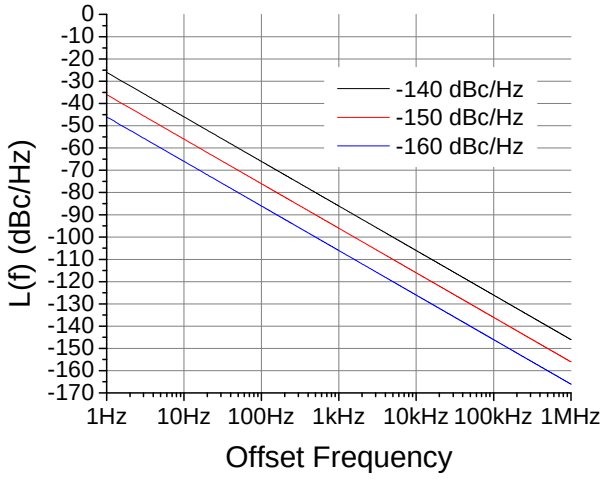


Figure 7.4: Predicted noise of the oscillator of Figure 7.3 for different levels of spontaneous emission noise from the mode-locked laser.

When the residual noise of the laser is too high, a separate, passive high Q element can be incorporated into the laser and used for phase noise reduction. A possibility is a delay line frequency discriminator. Using the formulation used to develop the Leeson model [57] (detailed in Appendix B), one can define a phase noise transfer function of the delay line by which internally generated phase noise fluctuations are transformed into the phase noise power spectrum of at the oscillator output. First, consider an oscillator with a single delay line only (such as in an optoelectronic oscillator). The delay line transfer function $D(\omega)$ is simply $e^{i\omega\tau}$ for a delay of $\tau$. The oscillator transfer function follows as

$$\left|H(\omega)\right|^2 = \frac{1}{2-2\cos(\omega\tau)}. \tag{7.5}$$

The phase noise power spectrum at the oscillator output is obtained by multiplying this transfer function by the phase noise power spectrum of the internally generated phase noise. A plot of Equation 7.5 is shown in Figure 7.5 for two different delays. Note that for longer delays, the noise decreases for low offset frequencies at the expense of increased spur density at multiples of $1/\tau$. The spurious modes at large offsets can be suppressed with a mode selection filter.

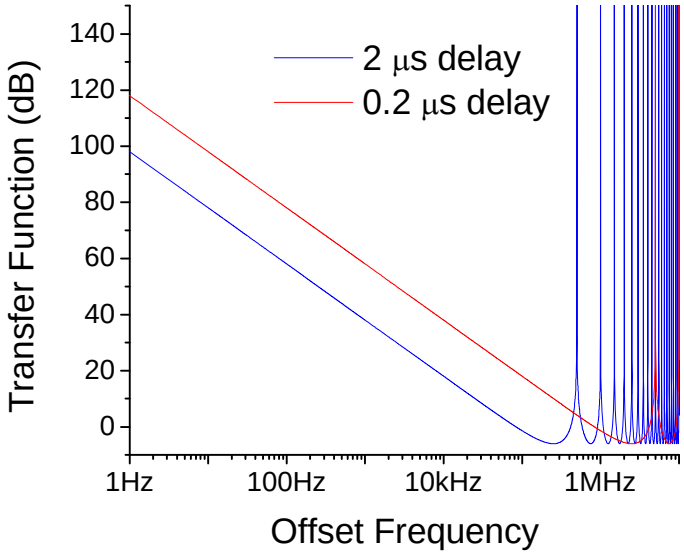


Figure 7.5: Phase noise transfer function of the delay line oscillator for two different values of delay.

To suppress modes closer to the carrier, a multiloop configuration can be implemented [58]. The double loop delay line transfer function is $\frac{1}{2}\left(e^{i\omega\tau_1}+e^{i\omega\tau_2}\right)$ and the oscillator transfer function is

$$\left|H(\omega)\right|^2=\left[1-\cos(\omega\tau_1)-\cos(\omega\tau_2)+\tfrac{1}{2}\left\{1+\cos\left(\omega(\tau_1-\tau_2)\right)\right\}\right]^{-1}. \tag{7.6}$$

Equation 7.6 is plotted in Figure 7.6.

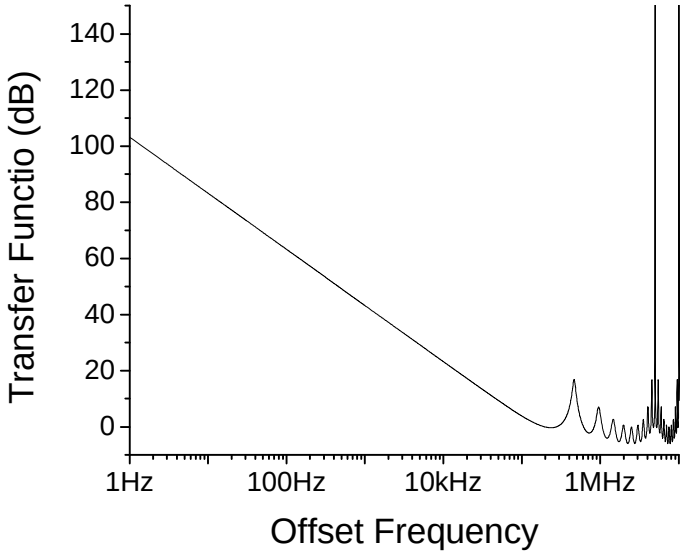


Figure 7.6: Phase noise transfer function of a dual loop delay line oscillator. The delays of the two loops used are 2 μs and 0.2 μs.

In using a delay line frequency discriminator for phase noise suppression, a dual loop configuration is inherent. A design that includes dual loop configuration with phase noise suppression is shown in Figure 7.7. The optical signal from the mode-locked laser is split in two and a long relative delay is introduced between the two arms. Since the noise in the phase noise reduction circuit will ultimately limit the oscillator's phase noise, decreasing the noise floor of the phase noise measurement is critical. The best way to do this is to use the interferometric noise measurement system described in Appendix A. The two signals are photodetected and sent to a 180° hybrid coupler. The sum port is used for the oscillator's electrical feedback. The difference port is used in a carrier suppressed noise measurement system. The output of this system is used to control the phase in the electrical feedback loop to suppress the phase noise. In order to maintain carrier

suppression at the difference port of the 180° hybrid coupler, the two photodetected signals are mixed, the output of which controls the quadrature phase shifter.

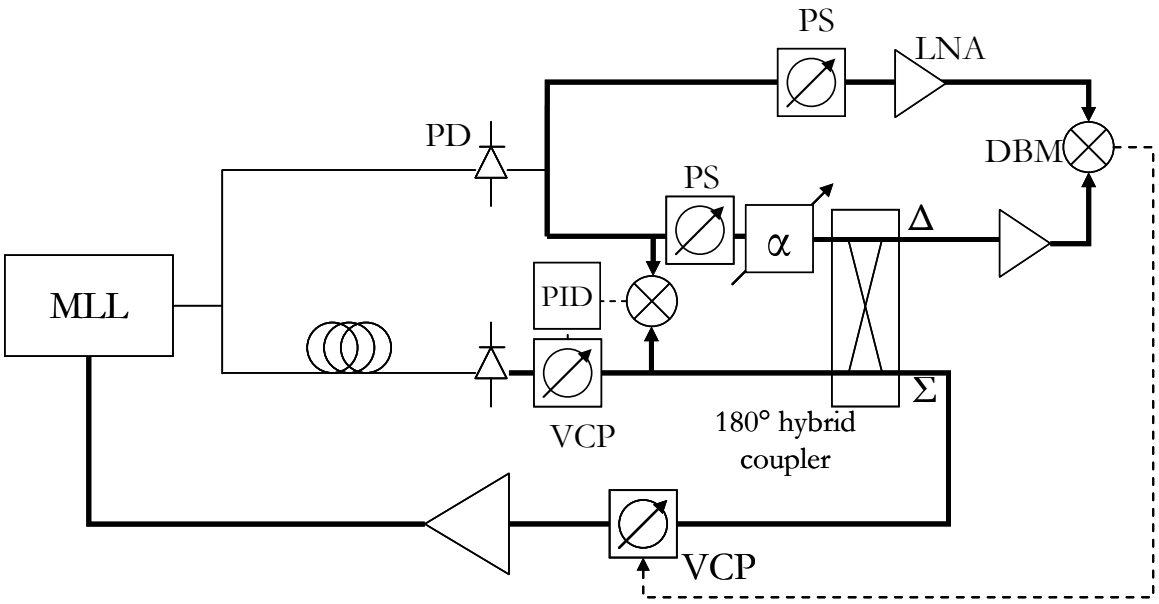


Figure 7.7: Proposed coupled optoelectronic oscillator with active noise suppression. Thick lines are electrical paths, thin lines are optical paths and the dotted lines are noise suppression feedback paths. PD, photodetector; PID, PID controller; α, variable attenuator; DBM, double balanced mixer; VCP, voltage controlled phase shifter, LNA, low noise amplifier; PS, phase shifter; MLL, mode-locked laser cavity.

Thus two separate approaches to improve the performance of a coupled optoelectronic oscillator have been outlined. The first is to simply incorporate an etalon with a higher finesse than is currently in use. This should quickly lead to lower jitter and increased stability of the optical modes. The second is a system applicable to any COEO (optical frequency stabilized or not) that relies on active suppression of the RF phase noise. The

implementation of this system is much more involved, and would require heavy investment to produce improved results over the higher finesse etalon design.

# APPENDIX A
# INTERFEROMETRIC NOISE MEASUREMENTS

The photodetected signals upon which phase and amplitude noise measurements are made are often low power – signal levels ranging from -20 dBm to -10 dBm are common. When measuring the noise of low power signals, an RF amplifier between the photodetector and mixer is necessary to saturate the mixer. As mentioned in Chapter 2, an important contribution to the measurement system noise floor is the flicker noise arising from the amplification of the RF carrier. The flicker contribution to the noise floor is double if both signal inputs to the mixer need amplification, as is often the case in a frequency discriminator. By employing an interferometric noise measurement, the flicker contribution of *both* amplifiers can be heavily mitigated [33]. Moreover, the system is easily changed from measuring phase noise to amplitude noise by tuning a phase shifter. The setup for the interferometric noise measurement is shown in Figure A.1. The two input signals are phase and amplitude balanced, then passed through a 180° hybrid coupler. A 180° hybrid coupler is a four-port (two inputs and two outputs) device. One output port (marked Δ) is the difference of the two input signals, while the other output port (marked Σ) is the sum of the two input signals. For input voltage signals *S(t)* and *R(t)*, the hybrid coupler output may be written as

$$V_{\Delta} = \frac{1}{\sqrt{2}}\left[S(t) - R(t)\right] \tag{A.1}$$

and

$$V_{\Sigma} = \frac{1}{\sqrt{2}}\left[S(t) + R(t)\right] \tag{A.2}$$

where the $1/\sqrt{2}$ is necessary for energy conservation. For two input signals of the same frequency, the carrier is suppressed at the output of the difference (dark) port. The output

of this port is therefore noise sidebands only. Without a carrier, the amplifier following the dark port will not flicker. A carrier does emerge from the sum port, and the amplifier following this port consequently will flicker, but this flicker noise will not be detected by the noise measurement system. To understand how this happens, consider Figure A.2. As in Figure 2.9, only carrier-sideband multiplications contribute to the measured signal. Unlike Figure 2.9, there is no carrier signal into one of the amplifiers and therefore no flicker. The other amplifier flickers, but because there is no carrier in the other port of the mixer, this flicker noise does not contribute to the output of the mixer.

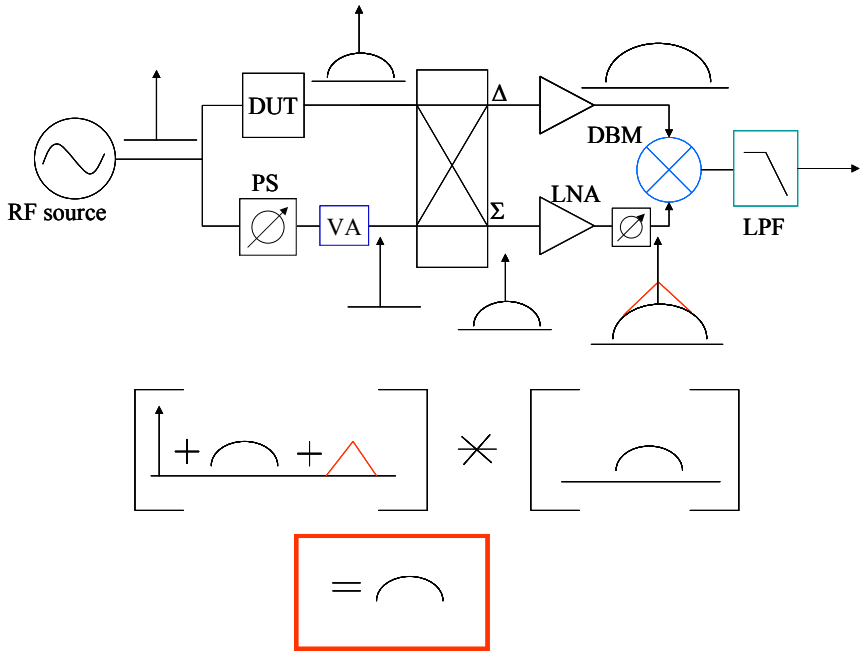


Figure A.1: Interferometric noise measurement setup. Suppressing the RF carrier in one port of the mixer suppresses the flicker noise from the noise floor. "*" denotes convolution.

To evaluate in detail how the interferometric noise measurement system measures amplitude and phase noise, consider input signals *S(t)* and *R(t)* of

$$S(t) = V_0\left[\cos(\omega_0 t) + \alpha_S(t)\cos(\omega_0 t) - \phi_S(t)\sin(\omega_0 t)\right] \tag{A.3}$$

and

$$R(t) = V_0\left[\cos(\omega_0 t) + \varepsilon\cos(\omega_0 t + \theta) + \alpha_R(t)\cos(\omega_0 t) - \phi_R(t)\sin(\omega_0 t)\right]. \tag{A.4}$$

The term $\varepsilon\cos(\omega_0 t + \theta)$ represents the imperfect phase and amplitude balance of the two signals, with $\varepsilon << 1$. Signal *S(t)* has amplitude and phase noise $\alpha_S(t)$ and $\phi_S(t)$, and the phase and amplitude noise of *R(t)* are $\phi_R(t)$ and $\alpha_R(t)$, respectively. The noise floor of the measurement system will be ignored for now. The signals from the Δ and Σ ports of the hybrid coupler follow as

$$V_\Delta = \frac{V_0}{\sqrt{2}}\left[(\alpha_S(t) - \alpha_R(t))\cos(\omega_0 t) - (\phi_S(t) - \phi_R(t))\sin(\omega_0 t) - \varepsilon\cos(\omega_0 t + \theta)\right] \tag{A.5}$$

and

$$V_\Sigma = \frac{V_0}{\sqrt{2}}\left[2\cos(\omega_0 t) + (\alpha_S(t) + \alpha_R(t))\cos(\omega_0 t) - (\phi_S(t) + \phi_R(t))\sin(\omega_0 t) + \varepsilon\cos(\omega_0 t + \theta)\right] \tag{A.6}$$

Accounting for a relative phase shift δ, the output of the mixer and low pass filter is given by

$$V_M = \eta\left[(\alpha_S(t) - \alpha_R(t))\cos(\delta) - (\phi_S(t) - \phi_R(t))\sin(\delta)\right]. \tag{A.7}$$

The detector constant is given by

$$\eta = \frac{V_0^2 a_1 b_1 \kappa}{2} \tag{A.8}$$

where $a_1$ is the gain of amplifier *a*, $b_1$ is the gain of amplifier *b*, and $\kappa$ is the (saturable) conversion efficiency of the mixer, and has the units of $(\text{Volts})^{-1}$. By setting δ to 0° or 90°, either the relative amplitude or phase noise is measured.

To determine the suppression of the amplifier flicker noise, the amplitude and phase noise of $S(t)$ and $R(t)$ are ignored. The signals from the Δ and Σ ports of the hybrid coupler are now expressed as

$$V_{\Delta} = \frac{V_0}{\sqrt{2}}\left[-\varepsilon\cos(\omega_0 t + \theta)\right] \tag{A.9}$$

and

$$V_{\Sigma} = \frac{V_0}{\sqrt{2}}\left[2\cos(\omega_0 t) + \varepsilon\cos(\omega_0 t + \theta)\right]. \tag{A.10}$$

When these signals are amplified, amplitude and phase flicker noise are added:

$$V_a = -\frac{V_0 a_1 \varepsilon}{\sqrt{2}}\left[\cos(\omega_0 t + \theta) + \alpha_a(t)\cos(\omega_0 t + \theta) - \varphi_a \sin(\omega_0 t + \theta)\right] \tag{A.11}$$

$$V_b = -\frac{2V_0 b_1}{\sqrt{2}}\left[\cos(\omega_0 t + \delta) + \alpha_b(t)\cos(\omega_0 t + \delta) - \varphi_b \sin(\omega_0 t + \delta)\right]. \tag{A.12}$$

The subscripts *a* and *b* indicate signals from amplifiers *a* and *b*, respectively. In the derivation of Equation A.12, the relative phase shift δ is accounted for and the small signal $\varepsilon\cos(\omega_0 t + \theta)$ was ignored. The baseband output of the mixer and lowpass filter is given by:

$$V_M = \varepsilon\eta\left[(\alpha_a(t) + \alpha_b(t))\cos(\theta) + (\varphi_a - \varphi_b)\sin(\theta)\right] \text{ for } \delta = 0 \tag{A.13}$$

and

$$V_M = \varepsilon\eta\left[(\alpha_a(t) + \alpha_b(t))\sin(\theta) + (\varphi_a - \varphi_b)\cos(\theta)\right] \text{ for } \delta = 90° \tag{A.14}$$

where only first order terms are retained. Note that the level of the amplifier flicker noise is reduced by the carrier suppression out of the dark port of the 180° hybrid coupler by amount $\varepsilon$.

An intereferometric noise measurement test set was built and characterized. Figure A.2 shows the noise floor of the system. Note the 20 dB improved sensitivity of the interferometric noise measurement system compared to the noise floor of Figure 2.8.

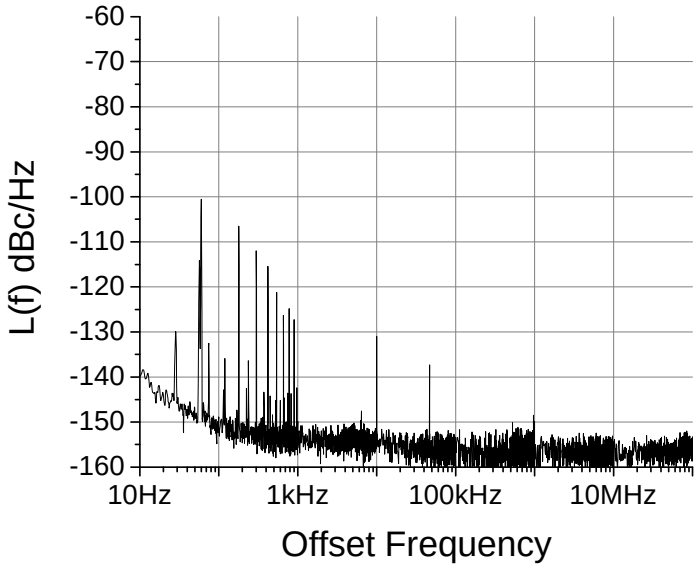


Figure A.2: Noise floor of a interferometric noise measurement system.

# APPENDIX B
# THE LEESON MODEL

A more rigorous analysis of the oscillation conditions and noise analysis of the RF signal generated from a coupled optoelectronic oscillator can be performed by considering a generalization of the COEO as a resonator with feedback oscillator. Shown in Figure B.1 is a simplified diagram of the oscillator, the major components of which are a resonator and an amplifier, to compensate for losses, connected in a feedback loop. (This can be applied to the COEO when considering the RF mode selected by the RF filter or etalon only.) The resonator's influence on the oscillating RF frequency comes not only from its action as a narrow bandpass filter; its dispersion plays a role as well. This can be seen by examining the condition for stable oscillation, the so-called Barkhausen condition [46]:

$$A \cdot R(\omega = \omega_0) = 1 \tag{B.1}$$

where $\omega_0$ is both the resonant frequency of the resonator and the oscillation frequency, $A$ is the action of the amplifier and $R$ is that of the resonator. The Barkhausen condition can be separated into phase and amplitude conditions, that is,

$$|A \cdot R(\omega = \omega_0)| = 1 \tag{B.2}$$

$$\arg[A \cdot R(\omega = \omega_0)] = 0. \tag{B.3}$$

Oscillation can occur if the small signal loop gain overcomes loop losses. The amplitude part of the condition is met by clamping the signal power through saturation of the amplifier gain. The phase response will be mostly determined by the resonator, and any phase response of the amplifier can be absorbed by $R(\omega)$. The phase condition then reduces to $\arg[R(\omega)]$ only.

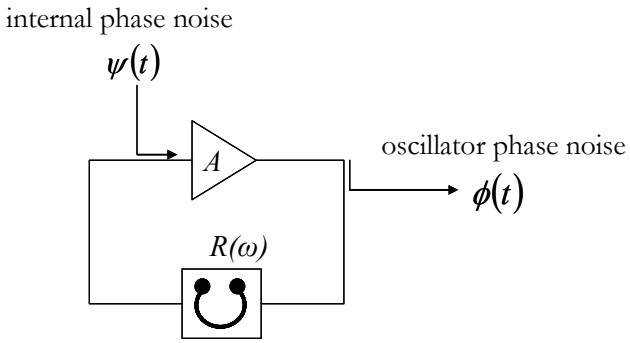


Figure B.1: The resonator with feedback. *A*, amplifier; *R*, resonator. The oscillator phase noise is related to the internal phase noise through the Leeson model.

By introducing a static phase shift $\delta$ into the loop, the Equation B.3 is modified to $\delta + \arg[R(\omega)] = 0$. Small static phase shifts will alter the oscillation frequency by amount $\Delta$, where

$$\Delta = \frac{\delta}{\frac{\partial}{\partial\omega}\arg[R(\omega)]_{\omega=\omega_0}}. \tag{B.4}$$

In other words, small changes in phase in the feedback loop of a COEO will convert to frequency changes of the RF signal (repetition rate) at the output. Also, the frequency of the COEO can be tuned by applying a phase shift in the feedback loop. The amount of tuning of the oscillation frequency is limited to the range where the small signal loop gain is exceeds the loss.

As noise of the RF signal is of chief concern, being able to predict the noise of the output signal as a function of the constituent parts is advantageous. The amplitude noise of such oscillators is largely clamped by saturation of the amplifier, and is typically much lower than the phase noise. Therefore, the phase noise of the oscillator is focused upon.

Predicting the phase noise of an oscillator such as the COEO from the phase noise of the constituent parts is performed through the Leeson model.

By assuming a linear shift invariant (LSI) system, the action of a component on a signal may be specified by its impulse response function. For an impulse response function $h(t)$ and transfer function $H(\omega)=|H(\omega)|e^{i\theta(\omega)}$, the action on the signal $\cos(\omega_0 t+\delta)$ is simply

$$H_0\cos(\omega_0 t+\delta+\theta_0) \tag{B.5}$$

where $H_0=|H(\omega_0)|$ and $\theta_0=\theta(\omega_0)$. If the signal has a small amount of phase noise $\phi(t)$, it can be shown that the signal at the output of the system may be written as

$$\begin{aligned} &H_0\left[1+\tfrac{1}{H_0}\left(h_s(t)*\phi(t)\cos\theta_0+h_c(t)*\phi(t)\sin\theta_0\right)\right]\times \\ &\cos\left\{\omega_0 t+\delta+\theta_0+\tfrac{1}{H_0}\left(h_c(t)*\phi(t)\cos\theta_0-h_s(t)*\phi(t)\sin\theta_0\right)\right\} \end{aligned} \tag{B.6}$$

where $h_c(t)$ and $h_s(t)$ are defined as

$$h_c(t)=\cos(\omega_0 t)h(t) \tag{B.7}$$

and

$$h_s(t)=\sin(\omega_0 t)h(t) \tag{B.8}$$

respectively, and $*$ denotes convolution. Equations B.7 and B.8 define the phase noise impulse response of a signal with low phase noise and negligible amplitude noise through a LSI system. It can be shown that the associated (double sided) phase noise transfer function may be written as

$$H_p(\omega)=\frac{1}{2H_0}\left(H(\omega-\omega_0)e^{-i\theta_0}+H(\omega+\omega_0)e^{i\theta_0}\right). \tag{B.9}$$

This result justifies our use of a phase noise transfer function to describe the action of an

actively mode-locked laser on the RF source phase noise in Section 3.6. Equation B.9 states that the phase noise transfer function is simply the normalized voltage transfer function. This means that knowledge of the voltage transfer function can be used to determine the system's response to phase noise, and vice versa.

Armed with a phase noise transfer function, when determining the phase noise of the oscillator, each component can be considered to act on the phase noise only. Consider Figure B.1. Phase noise $\psi$ is introduced prior to a noiseless amplifier. The amplifier phase noise transfer function is taken as equal to unity. To determine the transfer function of the resonator, either empirical data (such as that of Section 3.6) or knowledge of the voltage transfer function may be used. Both the assumption of a simple Lorentzian filter or the results for a mode-locked laser presented in Section 3.6 yield the same result, namely

$$R(\omega) = \frac{1}{1 + i\frac{\omega}{\Gamma}} \tag{B.10}$$

where Γ is the HWHM of the resonator's intensity response. The phase noise transfer function of the oscillator is defined by

$$\mathsf{H}(\omega) = \frac{\phi}{\psi}. \tag{B.11}$$

By starting at the output and continuing around the loop, the phase noise transfer function of the resonator with feedback oscillator is given by

$$\mathsf{H}(\omega) = \frac{1}{1 - R(\omega)}. \tag{B.12}$$

As described in Section 2.2.2, the power spectra of the input phase noise $S^{\psi}(\omega)$ and

oscillator phase noise $S^{\phi}(\omega)$ are related through the magnitude squared of the transfer function. The phase noise of the oscillator then follows as

$$S^{\phi}(\omega) = |H(\omega)|^2 S^{\psi}(\omega) = \left(1 + \frac{\Gamma^2}{\omega^2}\right) S^{\psi}(\omega). \tag{B.13}$$

This equation that relates the phase noise of an oscillator to the phase noise of introduced by components in the feedback loop was first given by Leeson [57] and is known as the Leeson model.

To understand the significance of Equation B.13, first consider frequencies $\omega >> \Gamma$. In this region of the phase noise spectrum, the oscillator phase noise is equivalent to the input phase noise. When $\omega << \Gamma$, however, there is a significant increase of the oscillator phase noise over that of the input phase noise. By recasting the phase noise in terms of the frequency noise $S_{\delta f}(\omega)$:

$$S_{\delta f}(\omega) = \Gamma^2 S^{\psi}(\omega) \quad \text{for} \qquad \omega << \Gamma \tag{B.14}$$

it can be seen that the frequency fluctuations of the oscillator are proportional to the input phase fluctuations. A plot of the Leeson model applied to the phase noise of an RF amplifier is shown in Figure B.2.

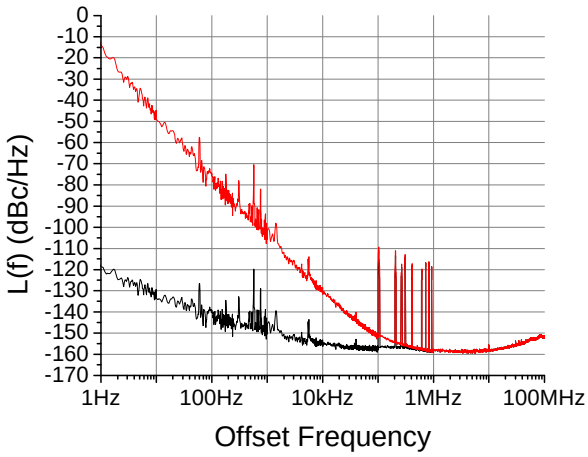


Figure B.2: Leeson model applied to a low noise RF amplifier. The amplifier phase noise is shown in black. The red curve is the application of Equation B.13 with

$$\Gamma/2\pi = 170\,kHz\,.$$

Similar noise models can be developed for the oscillator designs of Chapter 7 using a similar approach to the one presented here.

# REFERENCES


[1] P. J. Delfyett, S. Gee, M. T. Choi, H. Izadpanah, W. Lee, S. Ozharar, F. Quinlan, T. Yimaz, "Optical Frequency Combs From Semiconductor Lasers and Applications in Ultrawideband Signal Processing and Communications," J. Lightwave Technol. **7**, 2701-2719, (2006)

[2] A. Leven, Y. Yang, J. Lin, P. Kondratko, A. Tate, T. C. Hu, N. G. Weimann, Y. K. Chen, "High Speed Integrated InP Photonic Digital-to-Analog Converter," *Int. Conf. on Indium Phosphide and Related Materials Conf. Proc.*, paper MA1.1, 2006

[3] P. Juodawlkis, J. C. Twitchell, G. E. Betts, J. J. Hargreaves, R. D. Younger, J. L. Wasserman, F. J. O'Donnell, K. G. Ray, R. C. Williamson, "Optically Sampled Analog-to-Digital Converters," IEEE Trans. Microwave Theory Tech., **49**, 1840 (2001)

[4] W. Ng, Y. M. So, R. Stephens, D. Persechini, "Characterization of the Jitter in a Mode-Locked Er-Fiber Laser and Its Application in Photonic Sampling for Analog-to-Digital Conversion at 10Gsample/s," J. Lightwave Technol., **22**, 1953-1961, 2004

[5] A. Leven, Y. Yang, R. Kopf, A. Tate, T. C. Hu, J. Frackoviak, R. Reyes, N. G. Weimann, Y.K. Chen, R. DeSalvo, G. Burdge, G. Deibner, F. Quinlan, S.Gee, P. Delfyett, "High Sped Arbitrary Waveform Generation and Processing using a Photonic Digital-to-Analog Converter," LEOS Summer Topicals Meeting 2007, paper TuC2.1

[6] H. Taylor, "An optical analog to digital converter – Design and analysis," J. Quantum Electron.*,* **15**, 210-216, 1979

[7] M. T. Murphy, Th. Udem, R. Holzwarth, A. Sizmann, L. Pasquini, C. Araujo-Hauck, H. Dekker, S. D'Odorico, M. Fischer, T. W. Hänsch, A. Manescau, "High-precision wavelength calibration of astronomical spectrographs with laser frequency combs," Mon. Not. R. Astron. Soc., **380,** 839-847, 2007

[8] B. E. Little, S. T. Chu, P.P. Absil, J. V. Hryniewicz, F. G. Johnson, F. Seiferth, D. Gill, V. Van, O. King, M. Trakalo, "Very High-Order Microring Resonator Filters for WDM Applications," IEEE Photon. Technol. Lett., **16**, 2263-2265, 2004

[9] S. M. Foreman, K. W. Holman, D. D. Hudson, D. J. Jones, J. Ye, "Remote transfer of ultrastable frequency references via fiber networks," Rev. Sci. Instr., **78**, 021101 (2007)

[10] OMS7J. M. Kahn, "Modulation and Detection Techniques for Optical Communication Systems," *in Optical Amplifiers and Their Applications and Coherent Optical Technologies and Applications on CD-ROM* (The Optical Society of America, Washington, DC, 2006), CThC1

[11] F. Quinlan, S. Gee, S. Ozharar, P. J. Delfyett, "Stabilized Optical Frequency Comb Source for Coherent Communication and Signal Processing," OFC 2007, paper

[12] T. Yilmaz, C. M. Depriest, A. Braun, J. Abeles, P. J. Delfyett, "Noise in Fundamental and Harmonic Modelocked Semiconductor Lasers: Experiments and Simulations," J. Quantum Electron., **39**, 838-849, 2003

[13] K. Haneda, M. Yoshida, M. Nakazawa, H. Yokoyama, Y. Ogawa, "Linewidth and relative intensity noise measurements of longitudinal modes of ultrahigh-speed mode-locked laser diodes," Opt. Lett., **30**, 1000-1002, 2005

[14] D. R. Hjelme, A. R. Mickelson, "Theory of timing jitter in actively modelocked lasers," J. Quantum Electron., **28**, 1594-1605, 1992

[15] C. H. Henry, "Phase Noise in Semiconductor Lasers," J. Lightwave Technol. **LT-4**, 298-311, 1986

[16] P. T. Ho, "Phase and Amplitude Fluctuations in an Mode-Locked Laser," J. Quantum Electron., **QE-21**, 1806-1813, 1985

[17] J. Ye, S. T. Cundiff, Eds., *Femtosecond Optical Frequency Comb Technology*, Springer-Verlag, New York, 2005

[18] D. von der Linde, "Characterization of the noise in continuously operating modelocked lasers," Appl. Phys. B, **39**, 201 (1986)

[19] S. Gee, S. Ozharar, F. Quinlan, J. J. Plant, P. W. Juodawlkis, P. J. Delfyett, "Self-Stabilization of an Actively Mode-Locked Semiconductor-Based Fiber-Ring Laser for Ultralow Jitter," IEEE Photon. Technol. Lett., **19**, p. 498-500, 2007

[20] A. Yariv, *Optical Electronics in Modern Communications* 5th Edition, Oxford, New York, 1997

[21] M. Nakazawa, K. Tamura, E. Yoshida, "Supermode noise suppression in a harmonically modelocked fibre laser by selfphase modulation and spectral filtering," Electron. Lett., **32**, p. 461-463, 1996

[22] F. Rana, H. Lee, R. Ram, M. Grein, L. Jiang, E. Ippen, H. A. Haus, "Characterization of the noise and correlations in harmonically mode-locked lasers," J. Opt. Soc. Am. B, **19**, p. 2609-2621, 2002

[23] O. Pottiez, O. Deparis, R. Kiyan, M. Haelterman, P. Emplit, P. Megret, M. Blondel, "Supermode Noise of Harmonically Mode-Locked Erbuim Fiber Lasers With Composite Cavity," IEEE JQE, **38**, p. 252-259, 2002

[24] T. R. Schibli, J. Kim, O. Kuzucu, J. T. Gopinath, S. N. Tandom, G. S. Petrich, L. A. Kolodziejski, J. G. Fujimoto, E. P. Ippen, F. X. Kaertner, "Attosecond active synchronization of passively mode-locked lasers by balanced cross correlation," Opt. Lett., **28**, p. 947-949, 2003

[25] S. Gee, F. Quinlan, S. Ozharar, P. J. Delfyett, "Simultaneous Optical Comb Frequency Stabilization and Super-Mode Noise Suppression of Harmonically Mode-Locked Semiconductor Ring Laser Using an Intracavity Etalon," Photon. Technol. Lett., **17**, 199 (2005)

[26] F. Quinlan, S. Gee, S. Ozharar, P. J. Delfyett, "Ultralow-jitter and –amplitude noise semiconductor-based modelocked laser," Opt. Lett., **31**, 2870-2872, 2006

[27] C. W. Nelson, F. L. Walls, C. K. Boggs, "Extending the range for precision AM noise measurements," *IEEE Freq. Control Symp.*, 854-857, 1996

[28] Specifications of Agilient systems can be obtained at www.agilent.com.

[29] A. L. Lance, W. D. Seal, F. Labaar, "Phase Noise and AM Noise Measurements in the Frequency Domain," Infrared and Millimeter Waves, **11**, 239-289, 1984

[30] F. Quinlan, S. Gee, S. Ozharar, P. J. Delfyett, "The effects of filtering RF source phase noise by a low noise, high quality factor actively modelocked laser on the laser's absolute and relative phase noise," Opt. Express, **14**, 5346 (2006)

[31] D. J. Derickson, A. Mar, J. E. Bowers, "Residual and Absolute Timing Jitter in Actively Mode-locked Semiconductor Lasers," Electron. Lett., **26**, 2026-2028 (1990)

[32] P. J. Winzer, "Shot-noise formula for time-varying photon rates: a general derivation," J. Opt. Soc. Am. B., **14**, p. 2424-2429, 1997

[33] E. Rubiola, E. Salik, N. Yu, L. Maleki, "Phase-Noise and Amplitude-Noise Measurement of Low-Power Signals,"IEEE Freq. Cont. Symp. p. 292-297, 2004

[34] D. W. Rush, G. L. Burdge, P.-T. Ho, "The Linewidth of a Mode-Locked Semiconductor Laser Caused by Spontaneous Emission: Experimental Comparison to Single-Mode Operation," J. Quantum Electron., **QE-22**, 2088 (1986)

[35] N. A. Olsson, "Lightwave Systems with Optical Amplifiers," J. Lightwave Technol., **7**, 1071 (1989)

[36] S. Gee, F. Quinlan, S. Ozharar, P. J. Delfyett, "Correlation of supermode noise of harmonically mode-locked lasers," J. Opt. Soc. Am. B, **24**, pp. 1490-1497, 2007

[37] F. Quinlan, S. Gee, S. Ozharar, P. J. Delfyett, "Greater than 20 dB supermode noise suppression and timing jitter reduction via CW injection of a harmonically mode-locked laser," Photon. Technol. Lett., **19**, pp. 1221-1223, 2007

[38] A. Siegman, *Lasers,* University Science Books, Salsalito, CA, 1986

[39] A. Takada, W. Imajuku, "Linewidth Narrowing and Optical Phase Control of Mode-Locked Semiconductor Ring Laser Employing Optical Injection Locking," *IEEE Photon. Technol. Lett.*, vol. **9**, no. 10, pp. 1328-1330, Oct. 1997

[40] T. Jung, J.-L. Shen, D. Tong, S. Murthy, M. C. Wu, T. Tanburn-Ek, W. Weng, R. Lodenkamper, R. Davis, L. J. Lembo, J. C. Brock, "CW Injection Locking of a Mode-Locked Semiconductor Laser as a Local Oscillator Comb for Channelizing Broad-Band RF Signals," *IEEE Trans. Microwave Theory Tech.*, **47**, no. 7, pp. 1225-1233, July 1999

[41] G. Yabre, H. de Waardt, H. van den Boom, G.-D. Khoe, "Noise Characteristics of Single-Mode Semiconductor Lasers Under External Light Injection," *IEEE J. Quantum. Electron.,* **36**, no. 3, pp. 385-393, Mar. 2000

[42] R. W. Drever, P. J. L. Hall, F. V. Kowalski, J. Hough, G. M. Ford, A. J. Munley, H. Ward, "Laser Phase and Frequency stabilization using an optical resonator," Appl. Phys. B. **31**, 97-105 (1983)

[43] F. Quinlan, S. Gee, S. Ozharar, P. J. Delfyett, "Frequency Stabilized Low Timing Jitter Mode-Locked Laser with an Intracavity Etalon," CLEO 2007, paper CThHH6

[44] F. Quinlan, S. Gee, S. Ozharar, P. J. Delfyett, "Optical frequency self stabilization in a coupled optoelectronic oscillator," 2007 IEEE International Frequency Control Symposium Joint with the European Frequency and Time Forum, May 29-June 1, pp. 1023-1027

[45] S. Gee, S. Ozharar, F. Quinlan, P. J. Delfyett, "High precision measurement of free spectral range of etalon," Electron. Lett., **42**, pp. 715-716, 2006

[46] E. Rubiola, *The Leeson Effect*, 2002, www.rubiola.org

[47] X. Yao, L. Maleki, "Dual microwave and optical oscillator," Opt. Lett., **22**, p. 1867-1869, 1997

[48] R. J. Jones, J.-C. Diels, J. Jasapara, W. Rudolph, "Stabilization of the frequency, phase, and repetition rate of an ultra-short pulse train to a Fabry-Perot cavity," Opt. Comm., **175**, p. 409-418, 2000

[49] H. R. Telle, B. Lipphardt, J. Stenger, "Kerr-lens, mode-locked lasers as transfer oscillators for optical frequency measurements," Appl. Phys. B, **74**, p. 1-6, 2002

[50] N. R. Newbury, W. C. Swann, "Low-noise fiber-laser frequency combs," J. Opt. Soc. Am. B, **24**, p. 1756-1770, 2007

[51] N. R. Newbury, B. R. Washburn, "Theory of the Frequency Comb Output From a Femtosecond Fiber Laser," IEEE J. Quantum. Electron., **41**, pp. 1388-1402, 2005

[52] N. Yu, E. Salik, L. Maleki, "Ultralow-noise mode-locked laser with coupled optoelectronic oscillator configuration," Opt. Lett., **30**, 1231-1233, (2005).

[53] K. P. Birch, M. J. Downs, "Corrections to the Updated Elden Equation for the Refractive Index of Air," Metrologia, **31**, pp. 315-316, 1994

[54] E. Salik, N. Yu, L. Maleki, "An Ultralow Phase Noise Coupled Optoelectronic Oscillator," Photon. Technol. Lett., **19**, p. 444-446, 2007

[55] D. G. Santiago, G. J. Dick, "Microwave frequency discriminator with a cooled sapphire resonator for ultra-low phase noise," in Proc IEEE Freq. Control Symp., Hershey, PA, June 1992, pp. 176–182

[56] E. Ivanov, M. Tobar, "Low Phase-Noise Microwave Oscillators With Interferometric Signal Processing," IEEE-Trans. Microw. Theory and Techniques, **54**, p. 3284-3294, 2006

[57] D. B. Leeson, "A simple model of Feedback Oscillator Noise Spectrum," Proc. IEEE, p. 329-330, 1966

[58] T. Banky, B. Horvath, T. Berceli, "Optimum configuration of multiloop optoelectronic oscillators," J. Opt. Soc. B, **23**, p. 1371-1380, 2006